

Towards the creation of a two-dimensional optical tweezer array using a liquid crystal spatial light modulator

-MASTER THESIS-

by

Johanna Hennebichler, BSc

submitted to the Faculty of Mathematics, Computer
Science and Physics of the University of Innsbruck

in partial fulfillment of the requirements for the degree

Master of science (MSc)

supervised by

Univ.-Prof. Dr. Francesca Ferlaino,

Dr. Manfred Mark,

Institute for Experimental Physics, University of Innsbruck

Innsbruck, November 2023

Abstract

In this thesis, we study the generation of two-dimensional optical tweezer arrays via the phase modulation of a light field by means of a *liquid crystal spatial light modulator* (LC SLM). The final goal of our main experiment is to explore quantum simulation using *Rydberg atoms* of erbium trapped in optical tweezer arrays generated by an LC SLM.

In the first part of the thesis, we explain the main properties of Rydberg atoms and their interactions, followed by a review of erbium in Rydberg physics. Subsequently, we discuss the theoretical basics of *optical tweezer arrays* and how they can be realized experimentally via different optical devices, e.g. an LC SLM. A significant portion of the first part of the thesis is also dedicated to describing how to operate the LC SLM and how to calculate its corresponding phase patterns via so-called *phase retrieval algorithms*.

In the second part, we present the optical setup used in our experiment. We first perform aberration correction measurements with the use of *Zernike polynomials*. We can report a significant improvement of the focal spot quality after the aberration correction procedure. Then, we generate different geometries of optical tweezer arrays, first via the *Gerchberg-Saxton algorithm*. This algorithm yields a non-uniform reconstruction of trap intensities, such that an adaptation in terms of the *weighted Gerchberg-Saxton algorithm* has to be implemented instead. We find that the uniformity of the trap intensity increases considerably, reaching values of up to $\sim 98\%$, dependent on the trap geometry. We present the largest optical tweezer array we have been able to generate successfully so far, which is a rectangular lattice of 10×10 optical tweezers. Lastly, we briefly discuss the emergence of *ghost spots* in the reconstructed image and the dependence of the spot quality on the spot separation.

Contents

Abstract	i
Introduction	1
1 Rydberg atoms	5
1.1 General properties	5
1.2 Interactions between Rydberg atoms	7
1.2.1 Van der Waals interaction	8
1.2.2 Förster resonance	9
1.2.3 Resonant dipole-dipole interaction	11
1.3 Rydberg blockade	11
1.4 Erbium in Rydberg physics	13
1.4.1 Electronic configuration	14
1.4.2 Multielectron Rydberg properties	16
2 Optical tweezer arrays	19
2.1 Basics on optical tweezers	19
2.1.1 Trapping atoms with light	19
2.1.2 AC Stark effect	22
2.1.3 Gaussian beam	23
2.2 Methods to create optical tweezer arrays	25
2.2.1 Acousto-Optic Deflector (AOD)	26
2.2.2 Digital Micromirror Device (DMD)	27
2.2.3 Liquid Crystal Spatial Light Modulator (LC SLM)	28
2.3 Comparing LC SLM and DMD	34
3 Basics of operating LC SLMs	37
3.1 Driving an LC SLM	37

3.2	Flatness correction and blazed grating	39
3.3	Aberration correction	42
3.4	Phase retrieval algorithms	45
3.4.1	Gerchberg-Saxton (GS) algorithm	45
3.4.2	Weighted Gerchberg-Saxton (WGS) algorithm	48
3.5	Calculation of target patterns	49
4	Generating holographic 2D optical tweezer arrays	52
4.1	Optical setup	52
4.2	LC SLM calibration	54
4.3	Choosing the blazed grating	55
4.4	Aberration correction	57
4.5	Rectangular optical tweezer array	60
5	Performance and quality	65
5.1	Performance of WGS algorithm	65
5.2	Gallery of optical tweezer arrays	67
5.3	Scalability of WGS algorithm	70
5.4	Ghost spots	71
5.5	Separation of spots	73
6	Conclusion and Outlook	76
	Appendix	79
	Bibliography	85
	Acknowledgements	97

Introduction

Motivation

In 1924, Satyendranath Bose gave foundation to *Planck's law*, which was derived a few years earlier in 1900. He elegantly developed its first complete theoretical derivation using a statistical approach entirely based on the idea that light is made up of photons (which are bosons) [1]. Albert Einstein later picked up this approach and applied it to a mono-atomic ideal quantum gas. In other words, Einstein was able to generalize the *Bose statistic* to (massive) bosons, leading to the introduction of the *Bose-Einstein statistic* [2]. Following Bose's work, Einstein predicted that, at extremely low temperatures, a gas of bosons undergoes an unprecedented phase transition into a novel matter state, now called *Bose-Einstein condensate* (BEC).

For decades, Einstein's prediction remained a mere theoretical concept. Its experimental realization was mainly limited by the requirement of unimaginably low temperatures on the order of a few billionths of a degree above absolute zero. Thus, it was not until 70 years later that the first experimental observation of Einstein's theoretical prediction took place. This remarkable achievement was made possible by the invention of the laser in the 1960s and the subsequent development of novel laser cooling and trapping techniques in the 1980s [3]. In 1995, research groups were able to successfully realize Bose-Einstein condensates of different atomic species, including Na [4], Rb [5] and Li [6]. To honor this exceptional accomplishment, Eric A. Cornell, Carl E. Wieman and Wolfgang Ketterle were awarded with the Nobel prize in 2001 [7].

The technological approach used for the creation of BECs was then also applied to fermions, yielding a fundamentally different statistical behaviour.

Unlike bosons, identical fermions are not permitted to occupy the same state when cooled to certain temperatures. Instead, they begin to occupy one by one all the energy levels in the system, starting from the lowest one up to a certain *Fermi energy*. The cloud of ultracold fermions is then referred to as *degenerate Fermi gas* (DFG) and was first achieved in 1999 [8].

Within the past two decades, these ultracold atomic gases have revealed themselves to be promising platforms for quantum simulation as their high controllability allows for the simulation of exciting quantum phenomena, which are too complex to simulate using a standard computer [9]. In general, the construction of a useful, general-purpose quantum computer is found to be an exceptionally challenging task, whereas building a quantum simulator is a seemingly more realistic goal. Quantum simulators are well-controlled artificial quantum systems that are used to model a quantum system of interest by displaying the same characteristics. In particular, the combination of ultracold atomic gases either with *optical lattices* [10] or with moving *optical tweezer arrays* [11] has been found to offer vast opportunities for exploring quantum simulation.

An optical lattice is an artificial periodic potential generated by standing waves of light, which, in turn, are created by the interference of two or more counter-propagating laser beams. Thus, an optical lattice exhibits a high degree of flexibility as its configuration can easily be altered by tuning the frequency and/or the intensity of its counter-propagating laser beams. As a result, optical lattice systems are not only capable of storing fermionic and bosonic atoms, but also provide the powerful feature of tailoring the Hamiltonian by harnessing the tunability of the tunneling and interaction energy [10]. A first pioneering experiment reported the observation of the transition from the *superfluid phase* to the *Mott insulator phase* using bosonic atoms in a three-dimensional optical lattice [12].

Besides optical lattices, moving optical tweezer arrays have emerged as another platform for cold atom quantum simulation and are also the platform of choice in our experiment. In optical tweezer arrays, individual neutral atoms are trapped in highly focused laser beams and their locations can be controlled independently. Additionally, the optical tweezer platform is highly scalable and offers great controllability of the interaction between atoms via excitation to the *Rydberg state*. In this regard, a well-controlled quantum

system of Rydberg atoms can be harnessed to achieve *analog quantum simulation* by mimicking the respective Hamiltonian of choice [13]. In particular, both the strong *dipole-dipole* and the *van der Waals interaction* between Rydberg atoms, typically exceeding the MHz scale, are highly regarded and pave unique and novel paths in quantum simulation. To give a few examples, in an experiment studying quantum magnetism, it was possible to probe many-body dynamics using a one-dimensional 51-atom quantum simulator [14]. More recently, Ising-type models were implemented and the corresponding physical platform was scaled up to a regime of hundreds of Rydberg atoms, which becomes infeasible to simulate on a classical computer [15, 16]. In general, there exists a multitude of possible applications of Rydberg atoms in quantum science and a thorough overview thereof is provided in Ref. [17].

Both physical platforms rely on techniques to precisely control the intensity distribution of the light field experienced by the atoms. The use of light to control the external degrees of freedom of a particle was first proposed in the pioneering work of the American physicist Arthur Ashkin in the 1960s and 1970s [18]. He demonstrated that one could trap and manipulate dielectric particles using a focused laser beam, which established the foundation for future optical tweezers. However, it was not until a few years later in 1986, when Ashkin, along with his colleague Steven Chu and others, successfully developed the first optical tweezer capable of trapping single particles [19]. They used a high numerical aperture (NA) objective lens to very tightly focus the laser beam, consequently generating an intense light spot. Counter-intuitively, particles were drawn towards the focus of the beam rather than being pushed away, and they would even follow the laser beam as they were trapped in the focal spot at all times. A recent overview of optical tweezers and their applications is presented in Ref. [11].

There are many different devices for the generation of optical tweezer arrays, including *acousto-optic deflectors* (AODs), *digital micromirror devices* (DMDs) and *liquid crystal spatial light modulators* (LC SLMs). In our experiment, we have decided to use an LC SLM, which is a computer-controlled optical device capable of generating arbitrary intensity patterns. The aim of my master thesis now is to work towards the creation of two-dimensional optical tweezer arrays using an LC SLM. In particular, the long-term goal of the entire experiment is to achieve quantum simulation with erbium Rydberg atoms in an optical tweezer array.

Thesis overview

Chapter 1 first reviews Rydberg atoms, as we ultimately want to trap these in our two-dimensional optical tweezer array. We first discuss their general properties, followed by a section devoted to the interactions between Rydberg atoms. Additionally, we explain the Rydberg blockade and its importance regarding quantum simulation. Lastly, we focus on erbium in Rydberg physics, where we review its most relevant properties.

Chapter 2 introduces the basic concepts of atom-light interaction. We describe fundamental notions necessary to understand optical tweezer experiments and give an overview of different devices to create optical tweezer arrays. The main devices we discuss and compare are acousto-optic deflectors, digital micromirror devices and liquid crystal spatial light modulators.

Chapter 3 focuses on the basics for operating LC SLMs. We discuss how to drive an LC SLM and review different phase retrieval algorithms as means of retrieving phase patterns for the generation of optical tweezer arrays via LC SLMs.

Chapter 4 is devoted to the experimental realization, where we first present our optical setup, followed by a section focusing on the calibration of LC SLMs. We discuss aberration correction via LC SLMs and present our first results of rectangular optical tweezer arrays.

Chapter 5 gives an overview of our experimental results, where we discuss the performance of the phase-retrieval algorithms. We additionally present a gallery of different optical tweezer configurations and review the reconstruction quality and scalability of these algorithms.

Chapter 6 concludes the thesis with an outlook on how the LC SLM setup could be implemented in the main experiment. Finally, we give a brief summary of the thesis.

Chapter 1

Rydberg atoms

In this chapter, we want to give a general overview of Rydberg atoms, including their properties and interactions. Nowadays, Rydberg atoms find wide application in many research areas, as they exhibit exaggerated state-dependent properties [17]. In particular, one can benefit from these properties when controlling ordered assemblies of Rydberg atoms at a single-particle level. This is achieved via arrays of optical tweezers (see Chap. 2). Combined with strong Rydberg interactions, this approach provides a promising and attractive platform for quantum simulation [13]. In Sec. 1.1, we discuss the general properties of Rydberg atoms. Section 1.2 instead reviews the different interactions between Rydberg atoms, while Sec. 1.3 focuses on the Rydberg blockade. Finally, Sec. 1.4 is devoted to erbium in Rydberg physics.

1.1 General properties

In Rydberg atoms, one of the valence electrons is excited into a state with high principal quantum number $n > 10$. A high principle quantum number implies that there is an outer electron with an orbit far from the nucleus. In this case, the remaining core electrons shield this outer electron from the electric field created by the nucleus. In good approximation, the electric potential experienced by the outer electron then appears identical to that experienced by the electron in a hydrogen atom. The properties of Rydberg atoms therefore closely resemble the ones of hydrogen. The energy of an

atom in the state $|n, l, j, m_j\rangle$ is given by

$$E_{nlj} = -\frac{R_y}{(n - \delta_{lj})^2}, \quad (1.1)$$

where l is the orbital angular momentum quantum number, j the total electronic angular momentum quantum number, $R_y \approx 13.6 \text{ eV}$ the Rydberg constant and δ_{lj} the *quantum defect* [17]. The quantum defect refers to energy level corrections arising for multi-electron atomic species. Using the example of an alkali atom, there is only one valence electron accessible, while the atomic orbitals are fully filled with the remaining electrons. These electrons lead to a shielding of the electric field of all except for one proton, which is why the potential experienced by the valence electron resembles a point charge, creating a Coulomb-like potential. However, compared to the single proton in a hydrogen atom, the ionic core is much more complex. For alkali atoms with small orbital angular momentum, there is a finite probability for the valence electron to be inside the core or at least to penetrate the cloud of non-valence electrons shielding the core. If this is the case, the shielding is mitigated and the energy level structure changes. A study of the quantum defects for erbium specifically is provided in Ref. [20].

Atomic properties, like their dipole moment, their polarizability and their lifetime depend strongly on the principal quantum number n and they are enhanced by working with large values of n . Some of these properties are summarised in Table 1.1.

Table 1.1: Scaling of properties of Rydberg atoms with respect to the principal quantum number n .

Property	n -scaling
Binding energy	n^{-2}
Energy between adjacent n states	n^{-3}
Orbital radius	n^2
Dipole moment $\langle nl er n(l+1) \rangle$	n^2
Polarizability	n^7
Radiative lifetime	n^3

For instance, the n^2 -scaling of the orbital radius leads to the atom size massively increasing for large n , reaching values of up to a few microns. Hence, Rydberg atoms are also referred to as "giants" in the atomic world. Another property of Rydberg atoms - making them attractive objects to study - is the long radiative lifetime of the excited state scaling as n^3 . As a consequence of the large dipole moment scaling as n^2 , Rydberg atoms are also very polarizable with the polarizability scaling as n^7 . Thus, they are strongly sensitive to external electric fields, also including the electric field generated by neighbouring Rydberg atoms. Together with the small spacing between Rydberg levels, scaling as n^{-3} , Rydberg atoms are expected to undergo very strong interactions [21]. These strong interactions are governed by two mechanisms – the *dipole-dipole interaction* and the *van der Waals interaction*. The former describes the interaction of two dipolar atoms (or molecules), while the latter accounts for interactions of induced dipoles. More precisely, the van der Waals interaction emerges as the fluctuations of the charge distribution of one Rydberg atom give rise to instantaneous dipole moments, which subsequently induce dipole moments in neighbouring atoms.

1.2 Interactions between Rydberg atoms

The following discussion of the interactions between Rydberg atoms is primarily taken from Ref. [21], to which we refer the reader to for further information.

Let us consider two atoms, atom 1 at position \mathbf{R}_1 and atom 2 at position \mathbf{R}_2 separated by a distance $\mathbf{R} = \mathbf{R}_2 - \mathbf{R}_1$. We additionally assume the absence of any external electric or magnetic fields. As already briefly mentioned in the previous section, these atoms acquire a significant electric dipole moment when being excited to the Rydberg state. For the case of the interatomic separation $R \equiv |\mathbf{R}|$ being much larger than the extension of the electronic wavefunction, the interaction between the atoms is governed by the dipole-dipole interaction. The corresponding dipole-dipole interaction Hamiltonian reads

$$\hat{H}_{\text{dd}} = \frac{1}{4\pi\epsilon_0} \frac{\hat{\mathbf{d}}_1 \cdot \hat{\mathbf{d}}_2 - 3(\hat{\mathbf{d}}_1 \cdot \mathbf{n})(\hat{\mathbf{d}}_2 \cdot \mathbf{n})}{R^3}, \quad (1.2)$$

where $\hat{\mathbf{d}}_1$ and $\hat{\mathbf{d}}_2$ denote the electric dipole operator of atom 1 and atom 2, ϵ_0 the permittivity and $\mathbf{n} = \mathbf{R}/R$ a unit vector pointing from atom 1 towards

atom 2. In the following, the eigenstates of a single atom are labelled $|\alpha\rangle$, $|\beta\rangle$, \dots , where α and β summarize the respective quantum numbers n , l , j and m_j . The corresponding eigenenergies read E_α , E_β , \dots . Without any interaction present between the atoms, the eigenstate of the two-atom system is simply the pair state $|\alpha\beta\rangle = |\alpha\rangle \otimes |\beta\rangle$ with the energy $E_{\alpha\beta} = E_\alpha + E_\beta$.

1.2.1 Van der Waals interaction

We now assume that both atoms are prepared in the same initial state $|\alpha\rangle$, resulting in the pair state $|\alpha\alpha\rangle$. As depicted in Fig. 1.1 (a), this pair state is generally expected to be non-degenerate with respect to any other pair state. In this case, the mixing with other pair states is negligible, such that they can all be ignored. Thus, the effect of the interaction Hamiltonian given in Eq. (1.2) can be treated using non-degenerate perturbation theory.

To first order, the energy shift $\Delta E^{(1)}$ of the given unperturbed pair state $|\alpha\alpha\rangle$ is zero:

$$\Delta E^{(1)} = \langle \alpha\alpha | \hat{H}_{\text{dd}} | \alpha\alpha \rangle \quad (1.3)$$

$$= \frac{1}{4\pi\epsilon_0} \frac{\langle \alpha | \hat{\mathbf{d}}_1 | \alpha \rangle \langle \alpha | \hat{\mathbf{d}}_2 | \alpha \rangle - 3 \langle \alpha | \hat{\mathbf{d}}_1 \cdot \mathbf{n} | \alpha \rangle \langle \alpha | \hat{\mathbf{d}}_2 \cdot \mathbf{n} | \alpha \rangle}{R^3} = 0. \quad (1.4)$$

The average value of the dipole moment vanishes for reasons of parity. While the atomic state $|\alpha\rangle$ is of definite parity, the dipole operators $\hat{\mathbf{d}}_1$ and $\hat{\mathbf{d}}_2$ exhibit odd parity. Thus, the effect of the interaction Hamiltonian on the system is of second order. Continuing the perturbative calculations to second order results in

$$\Delta E^{(2)} = \sum_{\beta, \gamma, \dots} \frac{|\langle \alpha\alpha | \hat{H}_{\text{dd}} | \beta\gamma \rangle|^2}{E_{\alpha\alpha} - E_{\beta\gamma}} = \frac{C_6}{R^6}, \quad (1.5)$$

where the pair state $|\alpha\alpha\rangle$ is coupled to other pair states of different parity via \hat{H}_{dd} . The resulting non-zero shift scales as R^{-6} and the interaction giving rise to this shift is referred to as van der Waals interaction. The C_6 -coefficient takes the form

$$C_6 = \sum_{\beta, \gamma, \dots} \frac{|\langle \alpha | \hat{\mathbf{d}}_1 | \beta \rangle \langle \alpha | \hat{\mathbf{d}}_2 | \gamma \rangle - 3 \langle \alpha | \hat{\mathbf{d}}_1 \cdot \mathbf{n} | \beta \rangle \langle \alpha | \hat{\mathbf{d}}_2 \cdot \mathbf{n} | \gamma \rangle|^2}{(4\pi\epsilon_0)^2 (2E_\alpha - E_\beta - E_\gamma)}, \quad (1.6)$$

where the summation takes into account all feasible pair states $|\beta\gamma\rangle$ different from $|\alpha\alpha\rangle$, i.e. all interaction channels. The numerator of Eq. (1.6) is proportional to a dipole moment to the fourth power, while the denominator corresponds to the energy difference of adjacent pair states. Using Table 1.1, a simple scaling argument shows that C_6 scales as n^{11} . Consequently, the van der Waals interaction between two Rydberg atoms is very strong and for interatomic separations of a few microns, it can reach tens of MHz. The dependence of the van der Waals interaction on the distance of two Rydberg atoms was directly measured in Ref. [22], while a more comprehensive description of the van der Waals interaction in general can be found in Refs. [13, 21].

As stated in Ref. [21], the effects of the van der Waals interaction are in general pairwise additive for systems of $N > 2$ atoms. The corresponding interaction Hamiltonian for a system of N atoms then takes the form

$$H_{\text{vdW}} = \sum_{i < j} \frac{C_6}{R_{ij}^6} n_i n_j, \quad (1.7)$$

where $n_i = |r\rangle\langle r|_i$ denotes the projector on the Rydberg state of interest of atom i . Along with introducing the spin operators $\sigma_{x,y,z}$, mapping the ground state to the spin down state $|\downarrow\rangle = |g\rangle$ and the Rydberg state to the spin up state $|\uparrow\rangle = |r\rangle$ leads to the relation $n_i = (1 + \sigma_z^i)/2$. By adding an additional laser coherently driving the transition $|g\rangle \leftrightarrow |r\rangle$ with a Rabi frequency Ω and a detuning δ , the Hamiltonian reads

$$H_{\text{Ising}} = \frac{\hbar\Omega}{2} \sum_i \sigma_x^i + \sum_i (\hbar\delta + B_i) \sigma_z^i + \sum_{i < j} \frac{C_6}{R_{ij}^6} \sigma_z^i \sigma_z^j, \quad (1.8)$$

where $B_i = \sum_j C_6/R_{ij}^6$ [21]. In terms of quantum simulation, the Ising-like Hamiltonian in Eq. (1.8) can be used to simulate a quantum Ising magnet. Such simulations were conducted in Ref. [21] for a system of three Rydberg atoms.

1.2.2 Förster resonance

Until now, we have assumed that the pair state $|\alpha\alpha\rangle$ is a non-degenerate state. However, for certain values of n , the pair state $|\alpha\alpha\rangle$ turns out to be degenerate or quasi-degenerate with other pair states $|\beta\gamma\rangle$, as shown in Fig. 1.1 (b).

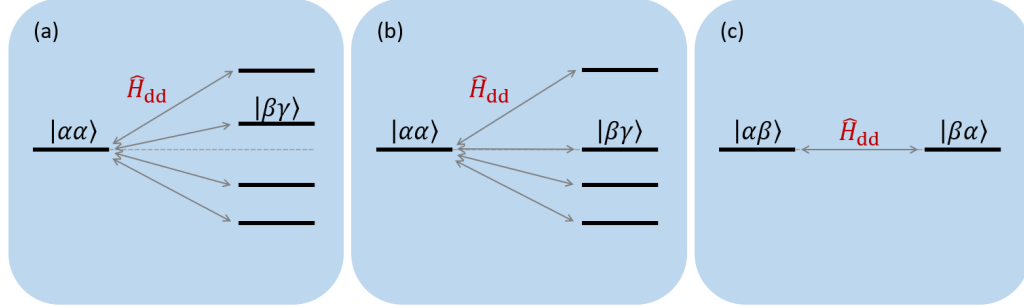


Figure 1.1: Different types of interactions between Rydberg atoms. (a) Van der Waals interaction. (b) Förster resonance. (c) Resonant dipole-dipole interaction.

If this is the case, the remaining non-degenerate states can be neglected and the presence of \hat{H}_{dd} gives rise to the new eigenstates $|\pm\rangle = (|\alpha\alpha\rangle \pm |\beta\gamma\rangle)/\sqrt{2}$, which are coherent superpositions of the two pair states. The dipolar interaction now manifests itself at first order and the corresponding eigenenergies are $E_{\pm} = \pm C_3/R^3$, where $C_3 = R^3 \langle \beta\gamma | \hat{H}_{dd} | \alpha\alpha \rangle$. Hence, the atoms do not interact via the van der Waals interaction scaling as R^{-6} , but instead via the resonantly enhanced long-range *Förster resonance* scaling as R^{-3} [21]. The Förster resonance is particularly useful for the realization of very strong Rydberg blockades [23, 24], as we will see in Sec. 1.3.

Typically, the pair states are only degenerate in good approximation, meaning they are quasi-degenerate. The corresponding difference in energy $\Delta = E_{\alpha\alpha} - E_{\beta\gamma}$ is referred to as *Förster defect* and usually takes on values on the order of a few MHz [21]. However, one can make use of the fact that the states $|\alpha\rangle$, $|\beta\rangle$ and $|\gamma\rangle$ generally exhibit different polarizabilities and hence are affected by an external electric field differently. Thus, the relative position of the pair states $|\alpha\alpha\rangle$ and $|\beta\gamma\rangle$ can be tuned individually via the Stark effect by applying an electric field. If the strength of the electric field is chosen appropriately, it is possible to obtain exact resonance between the pair states, i.e. $\Delta = 0$. Experimentally, this means that one can switch between the non-resonant weak van der Waals interaction and the comparatively strong resonant dipole-dipole interaction by tuning the external electric field accordingly [21].

1.2.3 Resonant dipole-dipole interaction

Instead of preparing the pair state $|\alpha\alpha\rangle$, we now assume the atoms are prepared in the pair state $|\alpha\beta\rangle$, which is degenerate with $|\beta\alpha\rangle$. As a consequence of this degeneracy as presented in Fig. 1.1 (c), a resonant dipole-dipole interaction between the distinct Rydberg atoms emerges. This gives rise to the new eigenstates $|\pm\rangle = \frac{1}{\sqrt{2}}(|\alpha\beta\rangle \pm |\beta\alpha\rangle)$ with the eigenenergies $E_{\pm} = \pm C_3/R^3$. The corresponding dipole-dipole Hamiltonian can hence be expressed in terms of the basis $\{|\alpha\beta\rangle, |\beta\alpha\rangle\}$ and takes the form

$$\hat{H}_{dd} = \frac{C_3}{R^3}(|\alpha\beta\rangle\langle\beta\alpha| + |\beta\alpha\rangle\langle\alpha\beta|). \quad (1.9)$$

Accordingly, an atom initially prepared in the pair state $|\alpha\beta\rangle$ will coherently evolve into $|\beta\alpha\rangle$ and subsequently back to $|\alpha\beta\rangle$. The corresponding "flip-flop" oscillation frequency is proportional to R^{-3} . The C_3 -coefficient is a product of two matrix elements of the dipole operator between the states $|\alpha\rangle$ and $|\beta\rangle$ and therefore scales as n^4 .

With regard to quantum simulation, the resonant dipole-dipole interaction can be harnessed for the direct implementation of spin interaction, which is explained in more detail in Ref. [21]. To do this, the pseudo-spin states $|\uparrow\rangle$ and $|\downarrow\rangle$ are encoded in $|\alpha\rangle$ and $|\beta\rangle$, respectively, giving rise to the XY spin Hamiltonian

$$H_{XY} = \sum_{i < j} \frac{C_3}{R_{ij}^3} (\sigma_+^i \sigma_-^j + \sigma_-^i \sigma_+^j), \quad (1.10)$$

where $\sigma_{\pm} = \sigma_x \pm i\sigma_y$. Such spin Hamiltonians have been an interesting subject of experimental research using ultracold polar molecules in optical lattices [25] or dipolar BECs [26].

1.3 Rydberg blockade

The Rydberg blockade is based on the interactions between Rydberg atoms as explained above, and was proposed in Ref. [27] as a means of implementing quantum gates with neutral atoms. For the sake of argument, we again look at a system consisting of two atoms, both in their ground state $|gg\rangle$ as shown in Fig. 1.2 (a). We furthermore consider a laser coherently coupling the ground state $|g\rangle$ to the Rydberg state $|r\rangle$ with a Rabi frequency Ω . Using

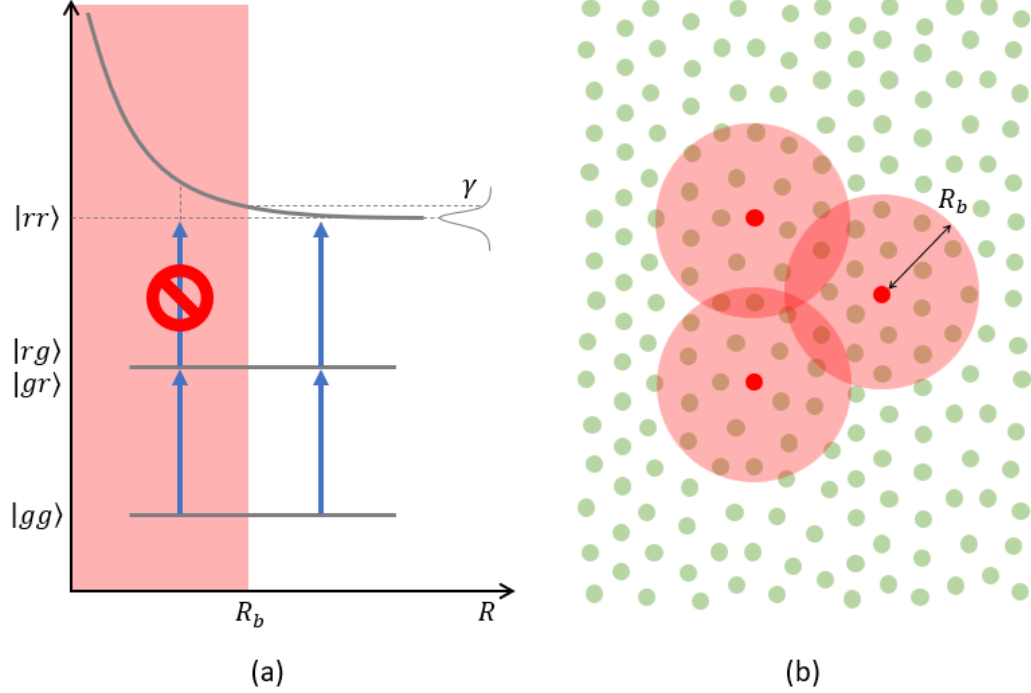


Figure 1.2: Rydberg blockade mechanism. (a) At short interatomic distances ($R < R_b$), the van der Waals interaction shifts the doubly-excited state $|rr\rangle$ out of resonance. The state is considered to be off-resonant when its corresponding energy shift is larger than its linewidth γ . (b) The Rydberg blockade also applies to an N -atom system, where the red dots represent Rydberg atoms and the red-shaded circles indicate the respective blockade volumes with a radius R_b .

this laser, one can now successfully drive the transition from the ground state to the Rydberg state of one of both atoms, resulting either in state $|gr\rangle$ or in state $|rg\rangle$. The state $|rr\rangle$ is shifted by the van der Waals interaction by an amount $\propto C_6/R^6$, where the strength of the energy shift depends on the interatomic distance R . For large interatomic distances, the presence of one Rydberg atom does not suppress the excitation of a new Rydberg atom as the energy shift is negligibly small and the laser is still on resonance with the excitation of the second atom.

However, for smaller interatomic distances, i.e. when the atoms are close enough, the van der Waals interaction shifts the energy levels of the neighbouring atom significantly. As soon as this energy shift becomes larger than the linewidth γ of the corresponding Rydberg state, as displayed in Fig. 1.2 (a), the excitation of this atom to the Rydberg state is severely suppressed. Consequently, one can define a volume surrounding the existing Rydberg atom with the so-called blockade radius

$$R_b = \left(\frac{C_6}{\gamma/2} \right)^{1/6}, \quad (1.11)$$

within which any Rydberg excitation to the doubly-excited state $|rr\rangle$ is not possible. Instead, the initial state $|gg\rangle$ evolves to the entangled state

$$|\psi_+\rangle = \frac{1}{\sqrt{2}}(|gr\rangle + |rg\rangle). \quad (1.12)$$

In this Rydberg blockade regime, both atoms are now coupled and will undergo Rabi oscillations between the collective states $|gg\rangle$ and $|\psi_+\rangle$ at a frequency of $\sqrt{2}\Omega$. Figure 1.2 (b) illustrates that this concept can also be extended to an ensemble of N atoms. Here, the presence of a single Rydberg atom strongly suppresses the Rydberg excitation of not only one, but a large number of atoms within its surrounding volume. Similarly, the N -atom system then oscillates between the collective states $|ggg\dots g\rangle$ and

$$|\psi_N\rangle = \frac{1}{\sqrt{N}} \sum_{j=1}^N |ggg\dots r_j\dots g\rangle \quad (1.13)$$

at a frequency of $\sqrt{N}\Omega$, where Ω is the single-atom Rabi frequency.

1.4 Erbium in Rydberg physics

In recent years, enormous progress has been made in studying the properties and applications of Rydberg atoms in quantum simulation, both in theoretical work as well as experimentally [28]. However, the majority of these studies has specifically put focus on investigating single- or two-electron systems like alkali [14, 29, 30], alkaline-earth [31, 32, 33] or alkaline-earth-like [34] atomic species. Instead, we aim at extending this Rydberg toolbox to

the more complex multi-valence-electron atomic species *erbium*.

Erbium (Er) belongs to the lanthanide series of the periodic table. It has an atomic number of $Z = 68$ and an atomic mass of $167.259(3)$ amu [35]. Solid erbium has a silvery-white metallic luster and is naturally only found in chemical combinations with other elements, hence it needs to be artificially isolated. Erbium in the form of Er^{+3} is an essential constituent in many technological applications and is most commonly used as a dopant in silica-glass fibers for laser light amplifiers [36].

Similar to many other lanthanides, erbium has a high melting point at 1529°C , and boiling point at around 2900°C . Erbium furthermore has six stable isotopes, five of which are bosonic isotopes (^{162}Er , ^{164}Er , ^{166}Er , ^{168}Er , ^{170}Er), and one fermionic (^{167}Er). Table 1.2 gives an overview of the relative abundance of each isotope and its corresponding type of quantum mechanical statistic.

Table 1.2: Isotopes of erbium. Six stable isotopes are reported and the relative abundances and statistics are listed according to Ref. [37].

Atomic mass number	Natural abundance	Quantum statistics
162	0.14%	Boson
164	1.6%	Boson
166	33.5	Boson
167	22.9%	Fermion
168	27%	Boson
170	14.9%	Boson

1.4.1 Electronic configuration

Erbium atoms are composed of a total of 68 electrons, 14 of which are valence electrons. The electrons are distributed among the electron shells as

$$(1s^2 2s^2 2p^6 3s^2 3p^6 3d^{10} 4s^2 4p^6 4d^{10} 5s^2 5p^6) 4f^{12} 6s^2 = [\text{Xe}] 4f^{12} 6s^2, \quad (1.14)$$

where the electronic configuration up to the $4f^{12}$ and $6s^2$ shells correspond to the electronic configuration of xenon (Xe). In accordance with the *Madelung*

rule, the $6s$ shell is filled up before the $4f$ shell with an increasing number of electrons. Because of this, all shells except for the $4f$ shell are completely filled. The only partially filled inner f shell is surrounded by the outer s shell and this type of configuration is therefore referred to as *submerged-shell configuration*.

Figure 1.3 illustrates the two missing electrons in the partially filled $4f$ shell, having an angular momentum projection quantum number of $m_l = +2$ and $+3$. Due to its large orbital angular momentum quantum number of $l = 3$, the $4f$ shell is additionally highly anisotropic, whereas the $6s$ shell exhibits spherical symmetry with $l = 0$. Figure 1.3 also displays this highly anisotropic angular dependence of the $4f$ shell, while the spherically symmetric $6s$ shell is depicted for comparison.

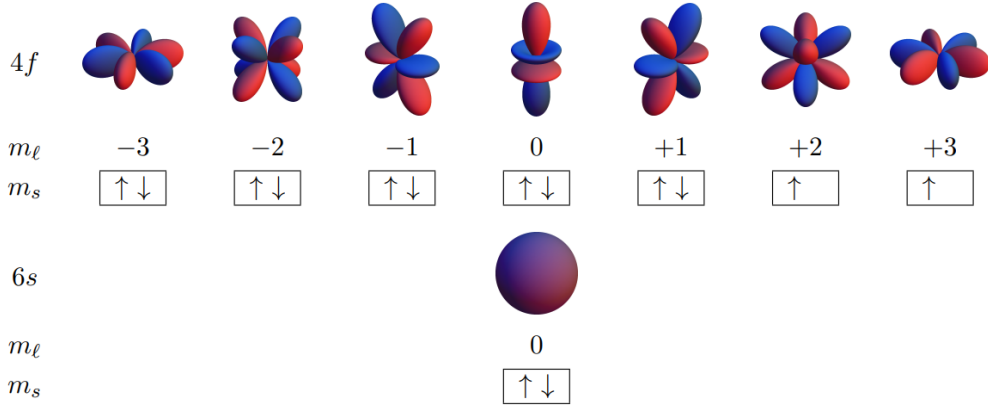


Figure 1.3: Illustration of the angular dependence of the $4f$ wavefunction for different m_l states. The individual images depict the anisotropy and isotropy in the probability density of the $4f$ and the $6s$ valence electrons of erbium, respectively. The arrows indicate the arrangement of these 14 valence electrons. Taken from Ref. [38].

The electrons occupy the $4f$ shell according to *Hund's rule*, satisfying the following set of criteria:

1. The multiplicity, defined as $2\mathbf{S} + 1$, needs to be maximized. Here, \mathbf{S} is the total spin angular momentum for all electrons.

2. For a given multiplicity, i.e. a fixed \mathbf{S} , the orbital angular momentum \mathbf{L} has to be maximized.
3. For atoms where the outermost shell is more than half-filled, the level with the lowest value of the electronic angular momentum \mathbf{J} lies lowest in energy, i.e. \mathbf{J} needs to be maximized.

Taking these criteria into consideration, the ground state of erbium has the properties

$$\mathbf{L} = 5, \quad \mathbf{S} = 1, \quad \mathbf{J} = 6.$$

The bosonic isotopes of erbium have an even number of protons and neutrons, thus resulting in a nuclear spin of $\mathbf{I} = 0$. Due to the nuclear spin being zero, the bosonic isotopes only exhibit fine structure splitting. Its fermionic isotope on the other hand has an even number of protons, but an odd number of neutrons, leading to a nuclear spin of $\mathbf{I} = 7/2$ instead. The electronic angular momentum \mathbf{J} couples with this non-zero nuclear spin, resulting in the total angular momentum $\mathbf{F} = 19/2$, which gives rise to a large hyperfine manifold. Here, it is interesting to point out that odd-even or even-odd nuclei will always have half-integer spin, whereas even-even and odd-odd nuclei have zero nuclear spin and integer nuclear spin, respectively [39].

1.4.2 Multielectron Rydberg properties

As already mentioned before, alkali atoms have been a common choice to study in the field of Rydberg physics for a long time. Alkali atoms belong to the first group of the periodic table and therefore hold one valence electron. Their relatively sparse atomic structure renders them easy to describe and additionally enables the implementation of robust cooling and trapping schemes. However, their simplicity comes at the expense of a limited degree of freedom for studying and controlling their Rydberg atoms. Alkaline-earth atoms on the other hand feature two valence electrons and therefore offer less restricted opportunities in this regard. Here, the key paradigm shift is that, after exciting one of the available valence electrons to the Rydberg state, the core remains optically active. This means that there still remains the second valence electron to work with, as we will discuss in a moment. The goal now is to push these boundaries even further by exploring the Rydberg physics of atoms with more than two valence electrons, e.g. lanthanides.

In general, multi-valence-electron atomic species such as erbium hold an extremely rich energy level structure and their unusual electronic configuration enables new forms of controlling these lanthanides [40]. In particular, the optically active core exhibits large remaining ionic-core polarizability, which is expected to allow for:

1. **Direct trapping:** One can leverage the polarizability for trapping the Rydberg atoms in conventional red-detuned optical tweezers (see Sec. 2.1.1) despite the repulsive ponderomotive action of the Rydberg electron [41].
2. **New excitation schemes:** The multiple valence electrons present in lanthanides give access to a rich plethora of possibilities for laser cooling, optical manipulation and also Rydberg excitation, ranging from ultra-narrow near-infrared (few Hz) optical transitions to broad near-ultraviolet (tens of MHz) ones [40].
3. **Large hyperfine manifold:** Thanks to the large angular momentum of lanthanides, the fermionic isotope's hyperfine structure can be used to encode large Hilbert spaces when doing quantum simulation [40].

In recent work, the excitation of erbium atoms to Rydberg states has been demonstrated. In Ref. [20], the Rydberg spectrum of ^{166}Er was studied, where a two-photon excitation scheme based on electromagnetically induced transparency (EIT) on a hot atomic beam was used. Figure 1.4 displays a scheme of the electronic levels of erbium, where electronic levels of odd and even parity are represented in black and red, respectively. The arrows indicate the corresponding dipole-allowed transitions of the valence electrons. The two-photon excitation scheme employed in Ref. [20] involves a 401-411 nm transition. Here, an atom initially in the $4f^{12}6s^2$ state was excited to the intermediate $4f^{12}6s6p$ state. Subsequently, the 411 nm transition was used to excite the atom to the final $4f^{12}6sns/nd$ state, i.e. to either the ns or the nd Rydberg series. As a result, approximately 550 different states of the ns and nd Rydberg series with n ranging from 14 up to 140 were identified successfully.

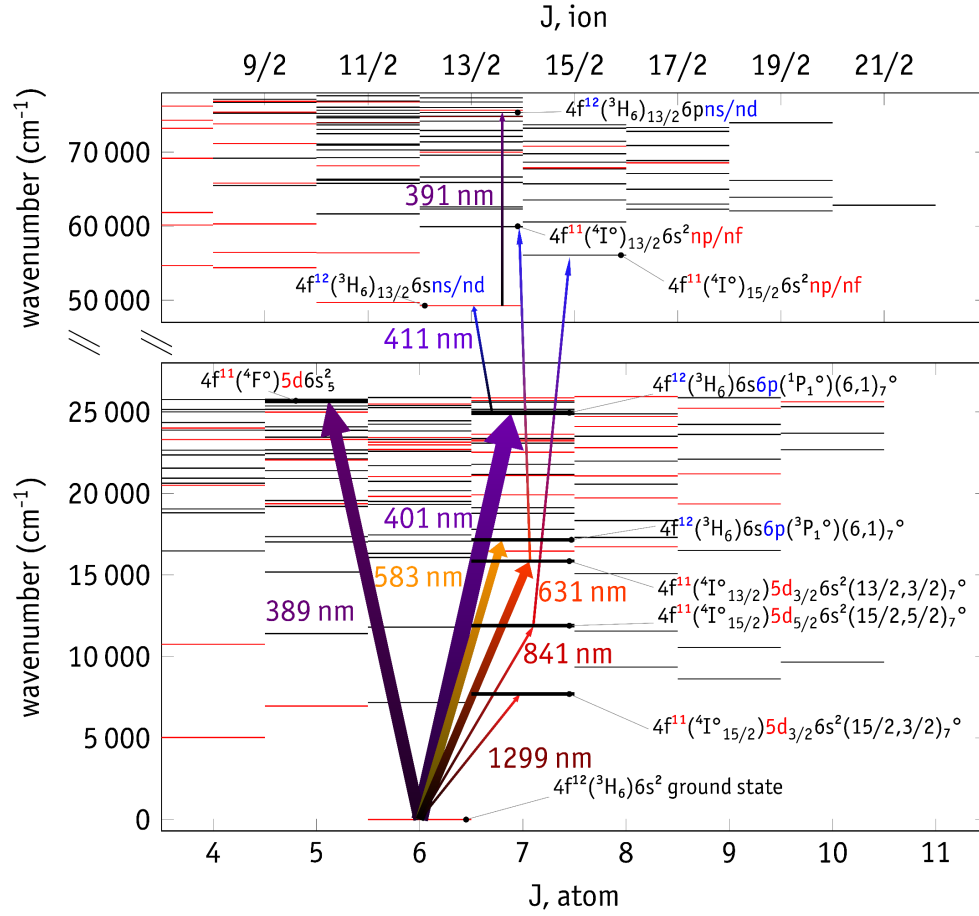


Figure 1.4: Scheme of electronic levels of erbium. The black electronic levels have odd parity, while the red ones have even parity. The arrows indicate dipole-allowed transitions, which can be used for Rydberg excitation via a two-photon excitation scheme. For instance, the 401-411 nm transitions can be used for Rydberg excitation of a 6s valence electron. Code provided by Ref. [42] and data taken from Refs. [43, 44].

Chapter 2

Optical tweezer arrays

While Chap. 1 provides an introduction to Rydberg atoms, this chapter focuses on optical tweezer arrays as a powerful tool in cold atom experiments. In Sec. 2.1, we first present an overview of the basic mechanism at the foundation of atom-light interaction based on Ref. [45], while a more comprehensive discussion can be found in Ref. [46]. Afterwards, we discuss different approaches for the generation of optical tweezer arrays in Sec. 2.2, involving acousto-optical deflectors (AODs), digital micromirror devices (DMDs) and liquid crystal spatial light modulators (LC SLMs). Finally, Sec. 2.3 provides a comparison between LC SLMs and DMDs.

2.1 Basics on optical tweezers

2.1.1 Trapping atoms with light

We can obtain a first intuitive picture of how trapping with light works by considering the case of a classical oscillator. When a neutral atom is subjected to laser light, i.e. an oscillating electric field $\vec{E}(\vec{r})$, the laser light induces an electric dipole moment $\vec{p}(\vec{r})$ in the atom. As a result, the induced electric dipole moment oscillates at the laser driving frequency ω and is given by

$$\vec{p}(\vec{r}) = \alpha(\omega)\vec{E}(\vec{r}), \quad (2.1)$$

where α denotes the complex polarizability and is dependent on the driving frequency ω , the atomic species and the polarization of the electric field. The interaction between the electric field and the dipole moment gives rise to the

atom-light interaction potential

$$U_{\text{dip}}(\vec{r}) = -\frac{1}{2} \langle \vec{p}(\vec{r}) \cdot \vec{E}(\vec{r}) \rangle = -\frac{1}{2\epsilon_0 c} \text{Re}(\alpha) I(\vec{r}). \quad (2.2)$$

Here, $I(\vec{r}) = 2\epsilon_0 c |\vec{E}(\vec{r})|^2$ describes the intensity of the electric field, while ϵ_0 denotes the dielectric constant, c the speed of light in vacuum and $\langle \cdot \rangle$ the time average. The real part of the polarizability $\text{Re}(\alpha)$ accounts for in-phase oscillations of the atom. Consequently, a spatial variation of the intensity (e.g. a focused laser beam) generates a trapping potential, governed by the so-called *dipole force*

$$\vec{F}_{\text{dip}}(\vec{r}) = -\nabla U_{\text{dip}}(\vec{r}) = \frac{1}{2\epsilon_0 c} \text{Re}(\alpha) \nabla I(\vec{r}). \quad (2.3)$$

We can see that, for the dipole force to be non-zero, an intensity gradient is strictly required. Such a gradient is typically obtained when using a tightly-focused Gaussian laser beam, which we discuss further in Sec. 2.1.3. The strength of the dipole force is then determined by the intensity gradient and its corresponding direction is determined by the real part of the polarizability. For the case of $\text{Re}(\alpha) > 0$, a net force towards the intensity maximum emerges.

In addition to being trapped in the generated potential, the oscillating atom also absorbs the power P_{abs} from the driving light field, which is subsequently emitted as dipolar radiation. This absorption can now be described using the imaginary part of the polarizability accounting for out-of-phase oscillations, leading to

$$P_{\text{abs}} = \langle \dot{\vec{p}}(\vec{r}) \cdot \vec{E}(\vec{r}) \rangle = \frac{\omega}{\epsilon_0 c} \text{Im}(\alpha) I(\vec{r}). \quad (2.4)$$

The amount of photons scattered by the atoms in the light field can be expressed by the scattering rate

$$\Gamma_{\text{sc}}(\vec{r}) = \frac{P_{\text{abs}}}{\hbar\omega} = \frac{1}{\hbar\epsilon_0 c} \text{Im}(\alpha) I(\vec{r}), \quad (2.5)$$

where \hbar is the Planck constant divided by 2π , while the quantity $\hbar\omega$ gives the energy of a single photon. These photons carry a momentum of $\vec{p} = \hbar\vec{k}$, and the atom therefore experiences a kick along the wavevector \vec{k} of the incoming photons. The resulting scattering force takes the form

$$\vec{F}_{\text{sc}}(\vec{r}) = \hbar\vec{k}\Gamma_{\text{sc}}(\vec{r}). \quad (2.6)$$

To find an expression for the polarizability α , one typically refers to one of two distinct theoretical models. Firstly, one can use the Lorentz-oscillator model, where an electron is elastically bound to the nucleus at an eigenfrequency equivalent to the frequency of the optical transition ω_0 . By integrating the corresponding equation of motion $\ddot{x} + \Gamma\dot{x} + \omega_0^2 x = -eE(t)/m_e$, the polarizability reads

$$\alpha(\omega) = 6\pi\epsilon_0 c^3 \frac{\Gamma/\omega_0^2}{\omega_0^2 - \omega^2 - i(\omega^3/\omega_0^2)\Gamma}. \quad (2.7)$$

Here, Γ denotes the damping rate associated with the radiative energy loss and m_e the electron's mass. Alternatively, one can use a semiclassical approach by considering a two-level system with a spontaneous decay rate Γ . Both methods yield the same result and are nicely discussed in Ref. [45]. In the case of large detuning, the following explicit expressions for both the dipole potential and the scattering rate can be derived:

$$U_{\text{dip}}(\vec{r}) = -\frac{3\pi c^2}{2\omega_0^3} \left(\frac{\Gamma}{\omega_0 - \omega} + \frac{\Gamma}{\omega_0 + \omega} \right) I(\vec{r}), \quad (2.8)$$

$$\Gamma_{\text{sc}}(\vec{r}) = \frac{3\pi c^2}{2\hbar\omega_0^3} \left(\frac{\omega}{\omega_0} \right)^3 \left(\frac{\Gamma}{\omega_0 - \omega} + \frac{\Gamma}{\omega_0 + \omega} \right) I(\vec{r}), \quad (2.9)$$

where Γ denotes the damping rate and ω_0 the atomic resonance. These expressions describe the most important relations for understand the physics behind optical tweezers experiments. If the detuning from the resonance $\Delta \equiv \omega - \omega_0$ is not too large by satisfying the condition $|\Delta| \ll \omega_0$, one can assume $\omega/\omega_0 \approx 1$, i.e. apply the *rotating-wave approximation*. As a result, the expressions for both the dipole potential and the scattering rate simplify to

$$U_{\text{dip}}(\vec{r}) = \frac{3\pi c^2}{2\omega_0^3} \frac{\Gamma}{\Delta} I(\vec{r}), \quad (2.10)$$

$$\Gamma_{\text{sc}}(\vec{r}) = \frac{3\pi c^2}{2\hbar\omega^3} \left(\frac{\Gamma}{\Delta} \right)^2 I(\vec{r}). \quad (2.11)$$

These equations provide important information regarding the features of optical trapping. More specifically, Eq. (2.10) indicates that the sign of the dipole potential is dependent on the detuning Δ of the laser light. If the detuning is negative (*red detuned*, $\Delta < 0$), implying a laser light frequency

smaller than the atomic transition, the dipole potential becomes negative and atoms are drawn towards high intensity regions. For a positive detuning (*blue detuned*, $\Delta > 0$) on the other hand, atoms are repelled by high intensity regions. When looking at the simple relation

$$\hbar\Gamma_{\text{sc}}(\vec{r}) = \frac{\Gamma}{\Delta} U_{\text{dip}}(\vec{r}) \quad (2.12)$$

we obtain when comparing Eq. (2.10) and Eq. (2.11), it becomes clear why usually far-detuned laser light is used for optical tweezers. As the dipole potential scales as $U_{\text{dip}} \propto I/\Delta$, while the scattering rate scales as $\Gamma_{\text{sc}} \propto I/\Delta^2$, it is shown that by increasing both the intensity of the light and the detuning, one can achieve the same trap depth with a lower scattering rate. This clearly shows the advantage of using optical dipole traps at high power as well as large detunings, as one can effectively suppress the scattering rate and subsequently reduce heating while maintaining the trap depth.

2.1.2 AC Stark effect

Instead of considering the atom as a classical oscillator, its motion in a far-detuned light field can alternatively be treated quantum mechanically. Mathematically, the influence of the oscillating light field on the atomic energy levels can be treated via perturbation theory as a second-order time-independent perturbation for non-degenerated states. The corresponding interaction Hamiltonian operator is given by $\hat{H} = -\hat{\mu}\vec{E}$, where $\hat{\mu} = -e\vec{r}$ defines the electric dipole operator. Considering a two-level system coupling to a far-detuned light field, the resulting energy shift of the ground state reads

$$\Delta E = \pm \frac{|\langle e|\mu|g\rangle|^2}{\Delta} |E|^2 = \pm \frac{3\pi c^2}{2\omega_0^2} \frac{\Gamma}{\Delta} I(\vec{r}), \quad (2.13)$$

with $|\langle e|\mu|g\rangle|$ being the dipole matrix element between the ground state $|g\rangle$ and the excited state $|e\rangle$. The \pm sign corresponds to the shift of the ground state and the excited state, respectively. Figure 2.1 (a) illustrates the AC Stark shift by showing how the ground state shifts down and the excited state up when applying red-detuned light ($\Delta < 0$). In particular, Fig. 2.1 (b) displays how a spatially inhomogeneous field, e.g. a Gaussian laser beam, gives rise to a ground-state potential well, in which an atom can be trapped. Comparing Eq. (2.13) to Eq. (2.10), we find that both treatments give the same result.

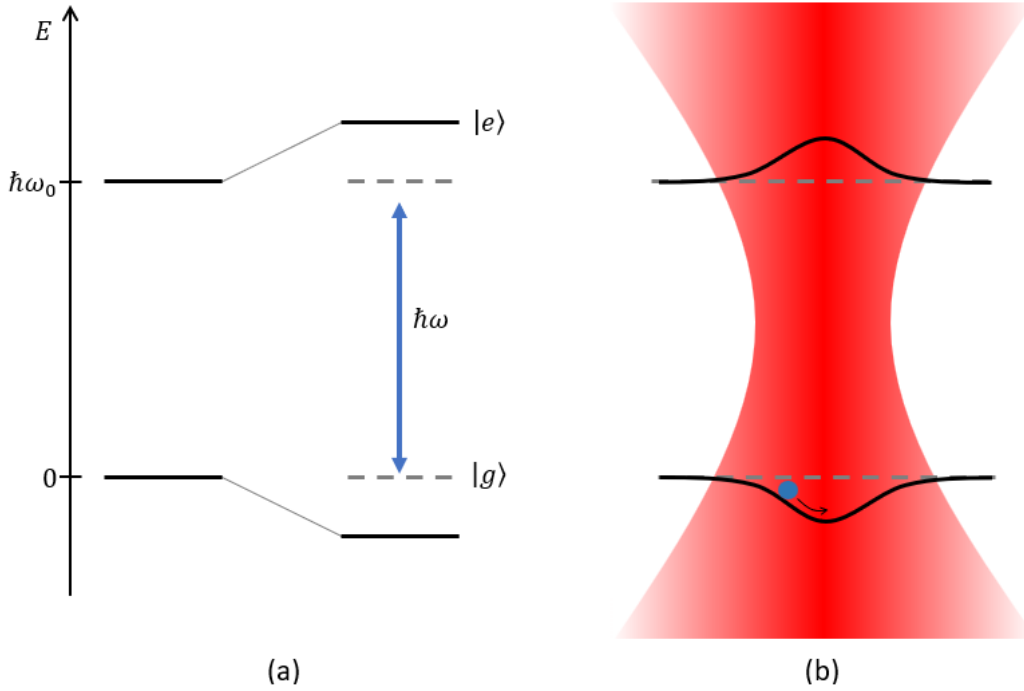


Figure 2.1: Schematic of the AC Stark shift for a two-level atom. (a) Red-detuned light ($\Delta < 0$) shifts the ground state down and the excited state up. (b) When using a Gaussian laser beam with spatially inhomogenous intensity, the light shift gives rise to a trapping potential drawing the atom towards the high-intensity region in the center.

2.1.3 Gaussian beam

As the dipole force in Eq. (2.3) relies on an intensity gradient of the light field and only traps atoms successfully for negative detunings, the simplest realization of an optical tweezer is a focused red-detuned Gaussian beam. The Gaussian beam provides three-dimensional confinement and its spatial intensity distribution propagating along the z -axis is given by

$$I(r, z) = \frac{2P}{\pi w^2(z)} \exp\left(-2\frac{r^2}{w^2(z)}\right), \quad (2.14)$$

where P is the total power, r the radial coordinate and $w(z)$ the $1/e^2$ radius. This radius can be expressed as

$$w(z) = w_0 \sqrt{1 + \left(\frac{z}{z_R}\right)^2}, \quad (2.15)$$

where w_0 denotes the minimum beam waist, z the axial coordinate and $z_R = \pi w_0^2/\lambda$ the Rayleigh range. Knowing the intensity distribution in Eq. (2.14), one can derive the optical potential $U(r, z) \propto I(r, z)$ using Eq. (2.10). As the maximum intensity of a Gaussian beam is located directly in the center of its focal point, the resulting trap depth then is $\hat{U} = |U(r=0, z=0)|$ [45].

We now consider an atomic sample with the thermal energy $k_B T$, where k_B denotes the Boltzman constant and T the temperature. If the thermal energy is considerably smaller than the potential depth \hat{U} , the atoms tend to only populate the center of the trap. Thus, the spatial extension of the sample turns out to be radially small compared to the beam waist and axially small compared to the Rayleigh range. In good approximation, the optical potential experienced by the atomic sample can then be described by a simple cylindrically symmetric harmonic oscillator reading

$$U(r, z) \simeq -\hat{U} \left[1 - 2 \left(\frac{r}{w_0}\right)^2 - \left(\frac{z}{z_R}\right)^2 \right]. \quad (2.16)$$

The corresponding trapping frequencies in the radial and axial direction are then given by

$$\omega_r = \sqrt{\frac{4\hat{U}}{mw_0^2}}, \quad \omega_z = \sqrt{\frac{2\hat{U}}{mz_R^2}}. \quad (2.17)$$

Because the Rayleigh length z_R is larger than the beam waist w_0 by a factor of $\pi w_0/\lambda$, the axial confinement is much weaker than the radial confinement. Knowing that $\hat{U} \propto P/w_0^2$ and $z_R \propto w_0^2$, the trap frequencies can alternatively be expressed as

$$\omega_r \propto \frac{\sqrt{P}}{w_0^2}, \quad \omega_z = \omega_r \frac{\lambda}{\sqrt{2}\pi w_0}. \quad (2.18)$$

Once you measure the radial and axial trap frequencies, e.g. via parametric heating, Eq. (2.18) provides a way of inferring the beam waist w_0 [47]. By doing this, one is able to quantify the quality of an optical tweezer, e.g. by

obtaining information about how Gaussian it is. More precisely, one can determine how Gaussian the beam is by checking that the ratio of the experimental values of the trap frequencies corresponds to the fraction in the second equation of Eq. (2.18).

2.2 Methods to create optical tweezer arrays

As we have briefly discussed in the beginning of this chapter, a single optical tweezer can be generated by focusing a red-detuned Gaussian beam. To focus the laser beam to the atoms, people usually use high NA objectives (0.5 or above is typical) [11]. The production of multiple optical tweezers though requires the application of so-called *spatial light modulation techniques*. These techniques enable the control over the phase and intensity distribution of the light field incident on the high NA objective. The basic idea of spatial light modulation is presented in Fig. 2.2, where the main ingredients for the generation of multiple optical tweezers are depicted schematically.

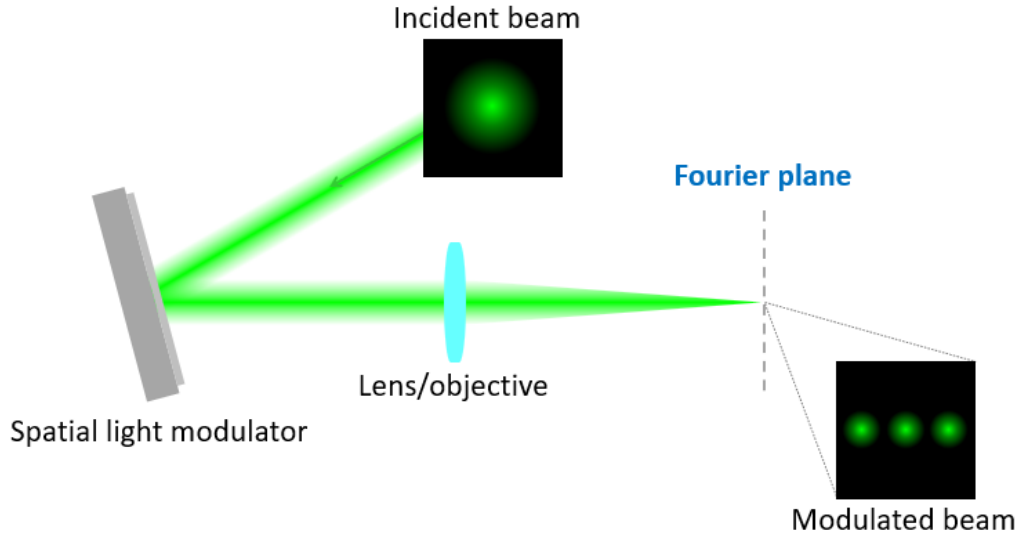


Figure 2.2: Illustration of a simple optical setup for spatial light modulation. The main ingredients are a laser beam, a spatial light modulator, and a lens or objective to be able to observe the modulated beam in a specific plane.

Spatial light modulators have a broad range of applications covering different areas of science. For instance, in astronomy spatial light modulators aid the correction of wavefront aberrations [48]. In biology, established application spaces include imaging in turbid media [49], optogenetics [50] and volumetric imaging [51]. In physics, spatial light modulators can for example be used for femtosecond pulse shaping [52]. However, the thesis focuses on its application in ultracold atom experiments, where many outstanding results have been reported within the last few years. These results include the creation of impurities by individually manipulating atomic spins [53], the realization of strongly correlated quantum walks in optical lattices [54] and, just recently, dynamic high-resolution optical trapping of ultracold atoms [55].

There are different approaches to achieve spatial light modulation. The main ones are acousto-optic deflectors, digital micromirror devices and liquid crystal spatial light modulators. In the following, we discuss these techniques in more detail.

2.2.1 Acousto-Optic Deflector (AOD)

An AOD is a device utilizing the interaction between acoustic waves and light waves to deflect a laser beam. Such devices consist of a crystal with a piezoelectric transducer attached to one of its edges. The piezoelectric transducer generates acoustic radio-frequency (RF) waves acting as a phase grating, travelling through the crystal at an acoustic velocity determined by the material. Here, the acoustic wavelength is dependent on the frequency of the RF tone and any laser incident on the AOD will be diffracted by this grating accordingly. When applying multiple RF tones, one is able to generate phase gratings of different wavelengths and each RF tone consequently causes the formation of a diffracted beam with a different diffraction angle, each of which can then be used for a distinct optical tweezer.

Even though they are intrinsically the same, AODs should not be confused with acousto-optic modulators (AOMs). As for AODs, we have already briefly explained that one alters the frequency of the RF tone to change the diffraction angle of the diffracted light. Here, the intensity of the corresponding output light remains unaffected. In the case of AOMs though, one instead alters the power of the RF driver, while maintaining the same RF tone. As a result, the intensity of the diffracted light experiences modulation,

while the respective diffraction angle does not change.

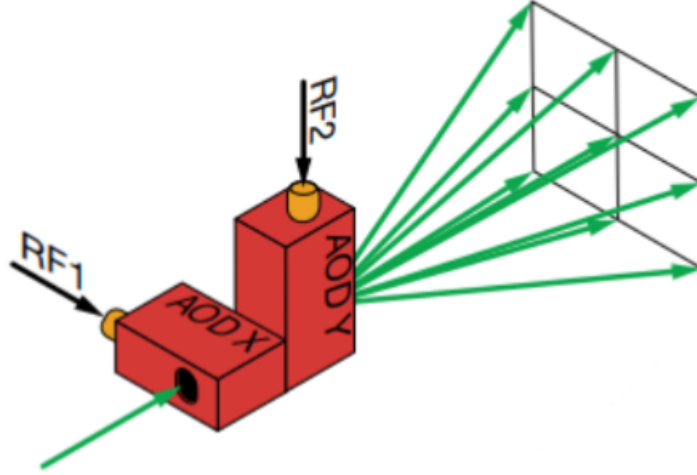


Figure 2.3: Creation of a two-dimensional optical tweezer array using two perpendicular AODs. Here, the spacing of the array in the x - and y -direction is determined by the driving radio-frequency signals RF1 and RF2, respectively. Taken from Ref. [56].

A single AOD can only produce a one-dimensional array of optical tweezers [14, 57]. However, by positioning two AODs consecutively perpendicular to each other as displayed in Fig. 2.3, a two-dimensional array of optical tweezers can be produced [58, 56]. Its geometry though is limited to rectangular/square arrays, which makes AODs unsuitable for the production of arrays of arbitrary geometry. Furthermore, there are not enough degrees of freedom to independently control the position of each trap. However, the fast and real-time control of the tweezer position when using AODs allows dynamic sorting of the atoms for assembling defect-free arrays [57, 29].

2.2.2 Digital Micromirror Device (DMD)

A digital micromirror device consists of a grid of several hundred thousand miniaturized mirrors, each of which corresponds to a pixel of the image to be displayed. By steering these microscopic mirrors individually, one can

modulate the light reflected off the mirror array. For this to be possible, each mirror is mounted on a yoke attached to a torsion hinge as shown in Fig. 2.4. This allows for the mirrors to be tilted in two angles, either -12° or $+12^\circ$, corresponding to an OFF or ON state, respectively. Depending on which position the mirror is set to, the incident beam is deflected into one of two distinct beam paths. This operational position is determined by two electrodes, where one electrode is positioned on each side of the hinge across the diagonal of the mirror. For a more detailed description of the working principle, we refer the reader to Ref. [59]. In general, the two-dimensional mirror array as employed by DMDs offers a greater variety of feasible geometries than two perpendicular AODs.

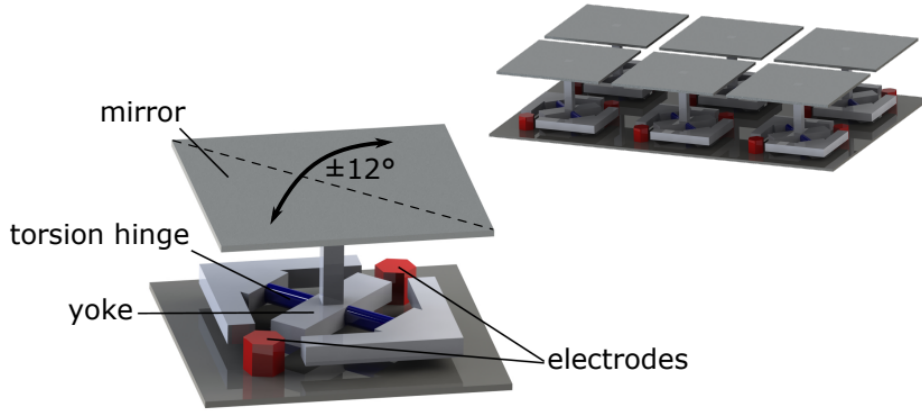


Figure 2.4: Schematic sketch of a DMD. A mirror is mounted on a yoke attached to a torsion hinge and has two operational positions, corresponding to a tilt of either -12° or $+12^\circ$. This position is determined by electrodes positioned underneath the diagonal of the mirror. Taken from Ref. [60].

2.2.3 Liquid Crystal Spatial Light Modulator (LC SLM)

In 1888 Friedrich Reinitzer investigated *cholesteryl benzoate* when he unexpectedly observed two *melting points*, with the substance exhibiting a mesophase between these melting points. The first melting point was reached at a temperature of 145°C , where the substance melted and became milky and viscous. Upon reaching the second melting point at 179°C , the substance would become perfectly transparent. He reported his findings to Otto

Lehmann, who further studied the material, and after discovering that it shared both liquid and crystal properties, he eventually coined the term *liquid crystal* [61].

Liquid crystals

Materials that exhibit a liquid crystal phase are typically composed of molecules that can be visualized as uniaxial ellipsoids with a single long axis about which they possess circular symmetry in any transverse plane. Typically, molecules forming liquid crystals tend to have polar or at least polarizable groups, which give rise to strong dipole-dipole or dipole-induced dipole interactions, and/or hydrogen bonds. In the solid phase, these rod-shaped molecules hold both *orientational* and *positional order*, meaning they sit at a distinct place and display a certain orientation. Conversely, the molecules neither possess orientational nor positional order in the liquid phase, both are random instead. In between, there exists this mesophase where the molecules still have residual orientational order, while having lost their positional order. As shown in the center of Fig. 2.5, this means that the molecules have arbitrary relative position, but still prefer to orient themselves along each other.

There are three major classes of liquid crystals, each different in its respective molecular order:

- **Nematic:** The nematic phase is presented in the center of Fig. 2.5. Here, the molecules tend to self-align themselves and exhibit long-range orientational order as their long axes are roughly parallel to each other. On average, the molecules are therefore aligned along a certain direction, called *director*, while still being able to move randomly.
- **Smectic:** In the smectic phase, the molecules organize themselves in well-defined layers along their long axes. The layers display a periodic structure along the direction perpendicular to the layers. Thus, a positional order in one dimension is present, while there is no positional order of the molecules within the layers.
- **Twisted nematic phase:** Unlike in the previous phases, molecules do not align parallel to each other in the twisted nematic phase, also called *cholesteric phase*. Instead, they form a helical structure, where a twisting of the molecules perpendicular to the director occurs.

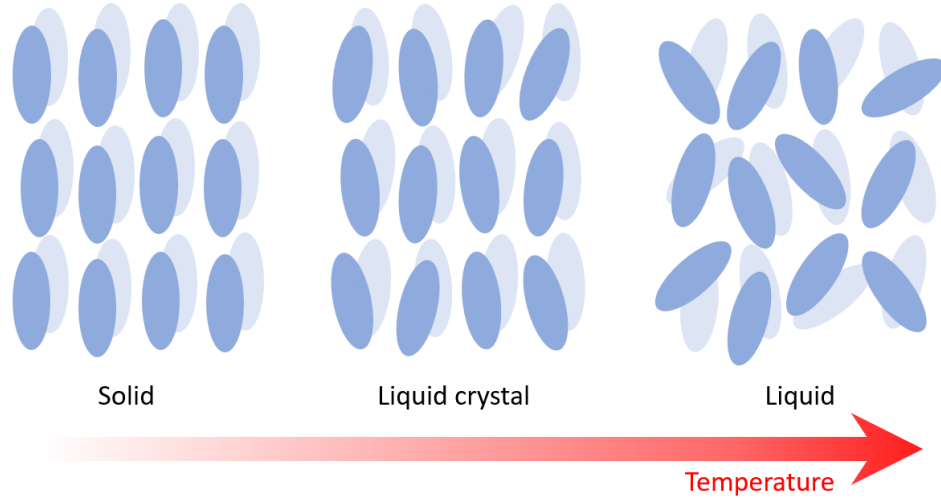


Figure 2.5: Phases of a liquid crystal material. At low temperatures, the material exhibits crystalline properties as it has both positional and orientational order. At high temperatures though, the material behaves like a liquid and displays neither positional nor orientational order. In between, it has a liquid crystalline mesophase with no positional, but orientational order.

For a more thorough description of these liquid crystal phases, we refer the reader to Ref. [62].

Light modulation with liquid crystals

LC SLMs can operate either in transmission or in reflection, but we will only explain the latter, as we also employ a reflective LC SLM in the experiment.

Figure 2.6 shows a schematic of a liquid crystal cell and serves to illustrate the working principle of an LC SLM. To achieve spatial light modulation, the liquid crystal layer is embedded between a glass plate and a reflective silicon substrate layer. On top of the silicon substrate, a layer of aluminium electrodes is arranged. Each of these electrodes makes up a pixel of the LC SLM display and its electric potential can be controlled independently. Additional alignment layers on each side of the liquid crystal layer set the natural orientation of the molecules. Typically, the liquid crystal molecules are ini-

tially set to align in parallel. The electric field across the liquid crystal layer can be controlled independently pixel by pixel, which causes the elongated liquid crystal molecules to tilt accordingly, dependent on the strength of the electric field.

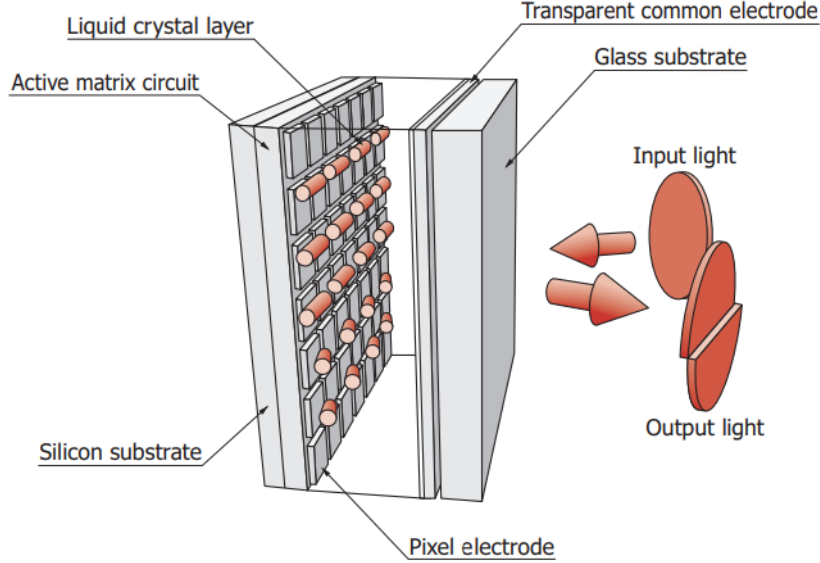


Figure 2.6: Schematic of the SLM chip structure. The liquid crystal layer is embedded between a glass plate and a reflective silicon substrate layer, where the latter contains pixels in the form of aluminium electrodes for controlling the orientation of the molecules. Taken from Ref. [63]

The refractive index experienced by the input light depends on the tilt of these liquid crystal molecules, as we will explain in more detail shortly. The phase modulation imprinted on the input light is therefore determined by the respective electric field applied to each pixel. Here, the linearly polarized light can only be modulated if its direction of polarization, i.e. the direction in which its electric field modulates, is aligned parallel to the initial alignment direction of the liquid crystal molecules. Proper phase modulation is infeasible if the incident light is either not linearly polarized, or its direction of polarization is not aligned with the liquid crystal molecules.

We have mentioned above that the refractive index experienced by the incident light beam is dictated by the orientation of the liquid crystal molecules.

More precisely, this is a result of the uniaxial anisotropy exhibited by molecules due to their elongated rod-like shape. Here, uniaxial anisotropy means there is one symmetry axis in the long direction of the molecules, while all remaining axes perpendicular to that axis are equivalent. The corresponding dielectric constant can be described by the tensor

$$\vec{\varepsilon} = \begin{bmatrix} \varepsilon_{\perp} & 0 & 0 \\ 0 & \varepsilon_{\perp} & 0 \\ 0 & 0 & \varepsilon_{\parallel} \end{bmatrix}, \quad (2.19)$$

where ε_{\parallel} denotes the dielectric constant in the axis of symmetry along the z -direction, and ε_{\perp} along the x - and y -direction, respectively. In general, $\Delta\varepsilon = \varepsilon_{\parallel} - \varepsilon_{\perp} > 0$ holds. When an electric field \vec{E} is now applied, the liquid crystal molecules rotate and their orientation changes with respect to their natural direction set by the alignment layers. Their director \vec{n} , i.e. the average orientation of the liquid crystal molecules, realigns along \vec{E} due to $\Delta\varepsilon > 0$.

The dielectric constant and the index of refraction are now closely linked by the relations $\varepsilon_{\perp} = n_o^2$ and $\varepsilon_{\parallel} = n_e^2$, where n_o and n_e stand for the ordinary and extraordinary index of refraction, respectively. If light now travels through the liquid crystal layer of an LC SLM, its different components of polarization will experience different indices of refraction, dependent on the angle between its direction of propagation and the orientation of the molecules. In this regard, the so-called *index ellipsoid* shown in Fig. 2.7(a) provides a concise representation of the refractive indices and associated polarizations as a function of the direction of propagation of the light beam.

In Fig. 2.7(b), the laser beam is given by its wavevector \vec{k} and is drawn as a line starting from the origin, enclosing an angle α with the extraordinary axis. Its associated polarization is defined in a plane passing through the origin perpendicular to \vec{k} , and can be decomposed into the components \vec{E}_o and \vec{E}_e . The resulting intersection of this plane with the index ellipsoid is an ellipse, as displayed in Fig. 2.7(c). As one can see, \vec{E}_o and \vec{E}_e lie along the minor and major axis of this ellipse and the associated indices of refraction are given by the length of the semi-minor and semi-major axis, respectively.

The index of refraction for the ordinary axis is found to be independent of

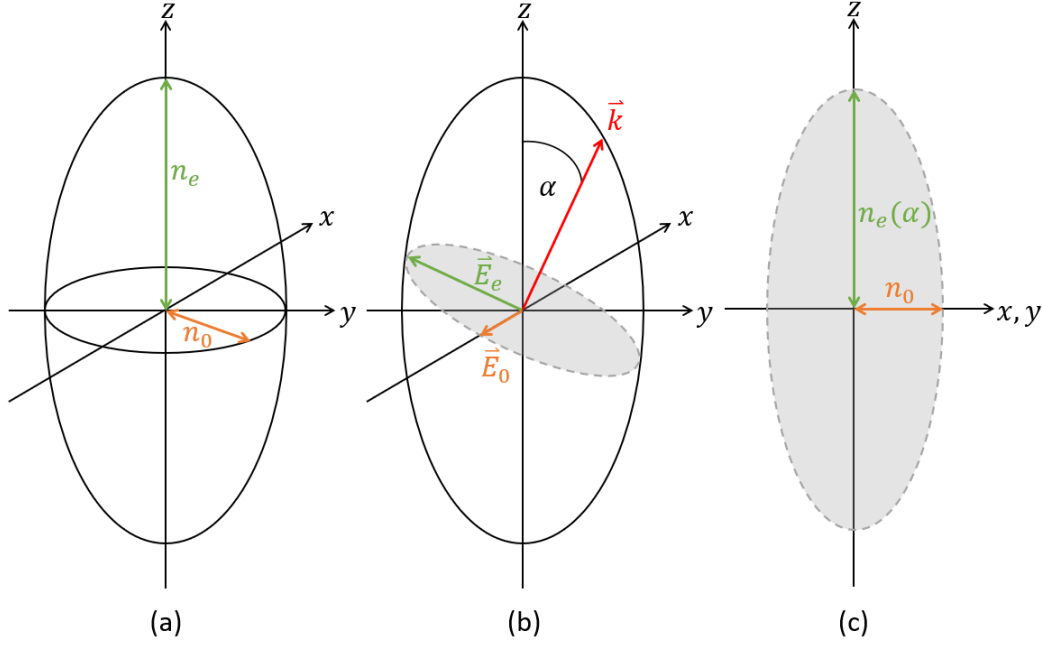


Figure 2.7: Index ellipsoid. (a) The long axis of the elongated liquid crystal molecule is oriented in the z -direction. The z -axis, or extraordinary axis, has an index of refraction denoted n_e , while the remaining x - and y -axis are the ordinary axes with an index of refraction given by n_o (b) The laser beam indicated by its wave vector \vec{k} is propagating through the liquid crystal molecule at an angle α with the extraordinary axis. Its polarization components \vec{E}_o and \vec{E}_e span a plane perpendicular to the direction of propagation (c) The intersection of the plane with the index ellipsoid results in an ellipse, which is used to determine the indices of refraction experienced by the respective polarization components.

the angle α , while the extraordinary index of refraction follows

$$\frac{1}{n_e^2(\alpha)} = \frac{\cos^2(\alpha)}{n_o^2} + \frac{\sin^2(\alpha)}{n_e^2}. \quad (2.20)$$

Consequently, to be able to modulate the light by changing the index of refraction it experiences, one has to change the angle α . There are two approaches for doing so, one of which involves changing the wave vector \vec{k} and thus changing the direction of propagation of the light beam, which is rather

impractical from an experimental point of view. The second approach, as also applied in LC SLMs and explained above, entails changing the orientation of the molecules instead. The optical property of a material having an index of refraction dependent on the direction of propagation and polarization of the light is referred to as *birefringence*.

For light polarized in a plane perpendicular to the optical axis, the liquid crystal molecules appear isotropic and the light only experiences the refractive index n_o , regardless of its specific polarization within the plane. Instead, if the light is only polarized in the z -direction, it does not exhibit any component with a polarization along the ordinary axis of the molecule and the resulting index of refraction is $n_e(\alpha)$, where α is a function of the applied voltage U . The phase shift of a reflected light beam is then given by

$$\phi(U) = n_e(U) \frac{2\pi D}{\lambda}, \quad (2.21)$$

where D is the thickness of the liquid crystal layer in the LC SLM and λ the wavelength [64].

2.3 Comparing LC SLM and DMD

LC SLMs certainly outplay DMDs when it comes to the degrees of freedom per pixel. While LC SLMs typically exhibit 256 voltage levels per pixel, DMDs operate using only binary pixels. The overall number of independently controllable pixels then dictates the extent of modulation complexity that can be achieved.

Alongside the degrees of freedom, there are several other factors determining the achievable performance of LC SLMs and DMDs. Especially in applications where high speed is required, the refresh rate of the device needs to be taken into consideration. Here, DMDs have a large advantage due to their extremely high refresh rate, reaching a maximum of up to 32 kHz [65]. These refresh rates are significantly faster than the typical trap frequencies, which enables the transport and rearrangement of atoms [66]. As opposed to DMDs, the main limitation of LC SLMs is their comparatively low refresh rate of typically less than 120 Hz, which is mainly limited by the LC responsiveness. Thus, LC SLMs are unable to operate on timescales required for

dynamic atom sorting.

Additionally, when exposed to a constant electric field, the liquid crystals of LC SLMs undergo chemical reactions that can eventually destroy them. Thus, LC SLMs are typically operated by alternating the polarity of the electric field across the liquid crystal layer. Dependent on the device, this cycling rate lies between a few Hz and kHz. This continuous switching of the polarity simultaneously alters the phase of every pixel periodically each time and therefore gives rise to temporal fluctuations in the phase, i.e. *phase flicker*. This phase flicker can affect the optical performance of the system by resulting in intensity fluctuations in the reconstructed light field. A comprehensive review of phase flicker associated with LC SLMs can be found in Ref. [67].

A significant advantage of LC SLMs is their *light utilization efficiency*, which is defined as the ratio of the first order diffraction light intensity to the input light intensity. The power that can typically be diffracted into the first order is limited mainly by diffraction loss due to the pixelated display. Here, the pixelated structure of the LC SLM gives rise to higher-order diffraction terms, which, in turn, are modulated by an envelope function arising from the finite pixel size [68, 69]. The presence of these useless higher-order images, also referred to as *ghost spots*, takes the light away from the useful first diffraction order and therefore slightly decreases the light utilization efficiency. These ghost spots will be discussed further in Sec. 5.4, while a comprehensive mathematical derivation of these higher-order diffraction terms as well as approaches regarding their suppression can be found in Ref. [70]. Additionally, the diffraction loss is dependent on the design of the LC SLM, i.e. the anti-reflection coating and the fill factor. Here, an imperfect anti-reflection coating of the front electrode yields an unmodulated beam because a fraction of the incident light is not able to pass through the liquid crystal layer and therefore does not experience modulation. Furthermore, the LC SLM exhibits a non-functional area due to a fill factor less than 100%, which additionally contributes to an unmodulated so-called *zero order spot*. A more detailed discussion about the importance of the fill factor is presented in Sec. 3.2. Regardless of these seeming disadvantages, in Ref. [71] it was found that 42% of the incident light can be redirected into the first order when applying a diagonal blazed grating with a periodicity of 4 pixels per period to the LC SLM. Subsequently, a binary amplitude grating of the same

periodicity was applied to a DMD, yielding a light utilization efficiency of just 8%. The reason why DMDs suffer from poor light utilization efficiency is the fact that all the beam power incident on mirrors in the OFF state is simply dumped. More precisely, the DMD creates a certain intensity pattern by removing light in specific locations, while the LC SLM uses constructive interference to redirect the optical power to the specific regions, where it is needed to reconstruct the image correctly.

Last but not least, spatial light modulation via LC SLMs has the unique feature of being very robust against local defects in the plane of the LC SLM, e.g. dead pixels. Each point of the reconstructed image is modelled by the entire LC SLM surface, which is why dead pixels do not significantly degrade the quality of the reconstructed image in the Fourier plane [68].

Taking everything into consideration, we have eventually decided to use an LC SLM. In the experiment, we generally want to work with dynamic optical tweezer arrays. However, the idea is to use the LC SLM to create only a static pattern, which will then be overlapped with the output of two perpendicular AODs to move the atoms around and therefore make the arrays dynamic. Thus, we accept the comparatively low refresh rate of the LC SLM, with the advantage of having significantly more degrees of freedom and a much better light utilization efficiency.

Chapter 3

Basics of operating LC SLMs

While Chap. 2 provides a general introduction to the different methods to spatially shape light and create arrays of identical tweezers, this chapter focuses on the particular realization we chose in our experiment. In Sec. 3.1 we briefly explain how to drive and address an LC SLM. In particular, we discuss the properties and different constituents of the input signal the device requires. In Secs. 3.2, 3.3 and 3.4, we review these constituents in greater detail one by one. Lastly, Sec. 3.5 is devoted to the calculation of target patterns, which are in turn used for the calculation of the input signal for the LC SLM.

3.1 Driving an LC SLM

In the experiment, we use the Hamamatsu X15213-16L LCOS-SLM. As shown in Fig. 3.1, the device consists of a head connected to its controller. The head is driven by the controller, which is connected to a PC via a standard digital video interface (DVI). In general, the controller is identified as a second PC screen and receives digital images from the PC, which are then converted into analog signals to send to the LC SLM head. The digital images we send to the controller are typically 8-bit grayscale image. The analog signal the controller sends to the head then corresponds to a two-dimensional array filled with values from 0 to 255, where a phase modulation value from 0 to 2π radians can be achieved. From now on, we refer to the grayscale images as *phase patterns*, while the values from 0 to 255 are denoted *gray levels*.

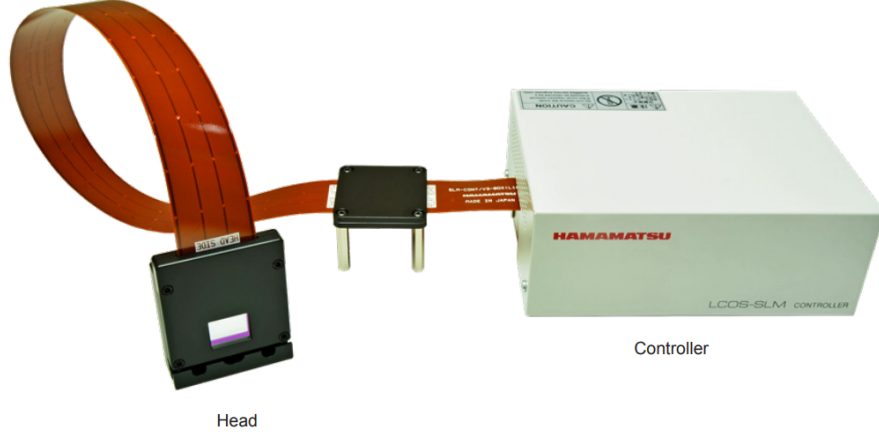


Figure 3.1: Hamamatsu LCOS-SLM X15213 series. Taken from Ref. [72].

Typically, the phase pattern ϕ_{total} we use to drive the LC SLM has several contributions, which are added as follows:

$$\phi_{\text{total}} = (\phi_{\text{factory}} + \phi_{\text{blaze}} + \phi_{\text{aberration}} + \phi_{\text{target}}) \cdot \text{mod}(255) \cdot \frac{g}{255}. \quad (3.1)$$

In this equation,

- (a) ϕ_{factory} is a compensation pattern provided by the manufacturer to correct for the optical non-flatness of the LC SLM backplane;
- (b) ϕ_{blaze} denotes a blazed grating, which is used in order to block the zero order spot of the LC SLM, which emerges due to its imperfect diffraction efficiency;
- (c) $\phi_{\text{aberration}}$ corrects for aberrations introduced by the optical system; and
- (d) ϕ_{target} accounts for the phase pattern giving rise to the intensity distribution of the desired final image.

Each of these patterns has values in between 0 and 255, such that after adding them, one has to calculate the modulus of the result with respect to 255 as the LC SLM demands an 8-bit input image. Here, the parameter g is for rescaling the gray level values dependent on the input wavelength.

In the following, we will review the different constituents as introduced above

in more detail one by one. Section 3.2 focuses on both the compensation pattern ϕ_{factory} and the blazed grating ϕ_{blaze} . In Sec. 3.3, we instead present the algorithm we use for aberration correction to obtain $\phi_{\text{aberration}}$. Finally, Sec. 3.4 introduces so-called *phase retrieval algorithms*, which we utilize to calculate the phase pattern ϕ_{target} .

3.2 Flatness correction and blazed grating

Due to fabrication limitations, the silicon substrate as depicted in Fig. 2.6 may not always be perfectly flat nor parallel. Since the phase shift given in Eq. (2.21) is proportional to the optical thickness, this inherent non-flatness consequently gives rise to an unwanted spatially varying phase delay over the entire LC SLM surface.

One can compensate for this fabrication imperfection by displaying a compensation pattern. Previous studies suggest three different techniques to obtain this compensation pattern, including interferometry, linear polarizers and diffraction based measurements [73]. In our case, this compensation pattern is already provided by the manufacturer and we therefore do not have to conduct additional correction measurements.

Figure 3.2 shows the compensation pattern as provided by the manufacturer, which was obtained using interferometry [63]. Here, it is important to note that due to the wavelength-dependence of the phase shift in Eq. (2.21), the flatness correction is consequently also wavelength-dependent and therefore needs to be chosen accordingly. The manufacturer though only provides compensation patterns in steps of 10 nm, and we therefore use the next closest one for a wavelength of 490 nm instead of the desired 486 nm. We assume that the deviation of 4 nm does not make a significant difference. This compensation pattern always has to be applied because it corrects a permanent deformation of the device.

Additionally, a common concern that unfortunately needs to be dealt with when using LC SLMs for holographic beam shaping is the occurrence of a strong zero order spot. For technical reasons, the LC SLM exhibits gaps at the junctions between adjacent pixels, where no phase modulation is feasible as the corresponding liquid crystal molecules cannot be addressed. In

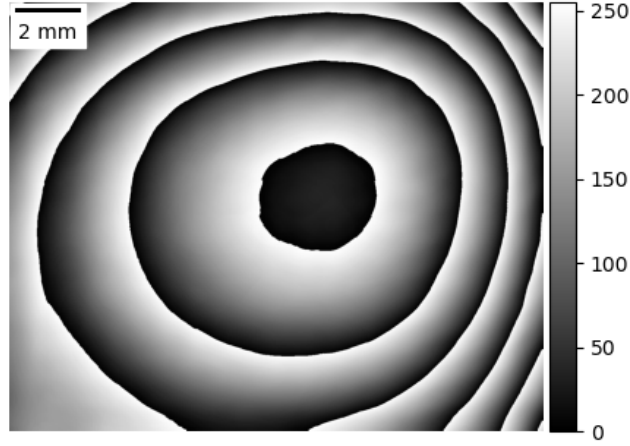


Figure 3.2: Compensation pattern for the non-flatness of the LC SLM backplane. This phase pattern is provided by the manufacturer and is specific to a wavelength of 490 nm. The manufacturer only provides compensation patterns in steps of 10 nm, which is the reason why no compensation pattern specifically for 486 nm is available. However, we consider the effect resulting from a difference of 4 nm to be negligible.

Fig. 3.3, the phase modulating pixels contributing to the active surface of the LC SLM are represented by the light gray squares, while the dark gray area corresponds to these non-addressable inter-pixel gaps. This feature translates to a fill factor $F < 100\%$, where the fill factor is given by the ratio between the active surface of the LC SLM and its entire surface. For a fill factor of $F = 100\%$, the pixel pitch and the pixel size would have to be equal. As the light hitting the gaps does not experience any type of phase modulation by the LC SLM, it consequently contributes to the zero order beam along the optical axis [74]. This unwanted effect not only uses up light, but as a result also creates a high intensity region of unmodulated light, which can interfere with the target pattern and compromise its reconstruction quality.

There are multiple approaches to bypass this effect, one of which is simply utilizing a region far away from the zero order spot by shifting the target pattern away from the optical axis. However, this technique would be very inefficient as it limits the size of the functional area and also reduces diffraction

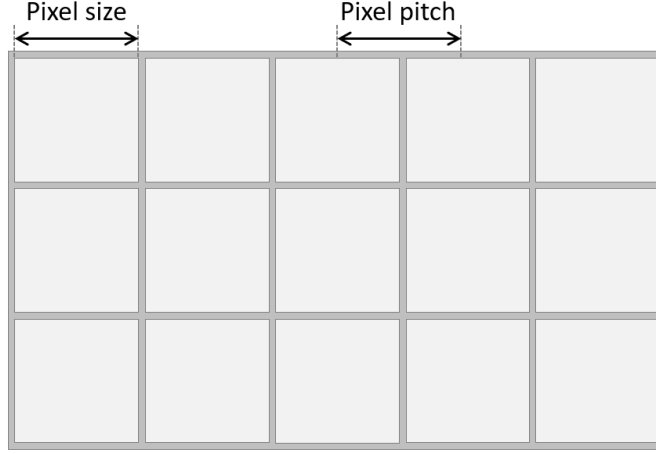


Figure 3.3: LC SLM pixel array. The gray squares illustrate individual pixels, while the dark gray area resembles a non-functional area between the pixels. Light incident on these gaps is not modulated and instead gives rise to a bright zero order spot that can negatively affect the quality of the final image.

efficiency. As described in Refs. [75, 76], one could also create a cancellation beam with the same profile as the zero order beam combined with the target pattern. By forcing a π -phase shift between the cancellation beam and the zero order beam, one can successfully suppress the zero order beam as the beams would destructively interfere. However, this process turns out to be rather slow when trying to apply it to more complex target patterns. The reason is that the calculation of the phase pattern for the cancellation beam is based on the iterative Gerchberg-Saxton algorithm (see Sec. 3.4.1) and is therefore time consuming, especially for more complex target patterns. Another approach involves applying a blazed grating to selectively deflect the higher orders and subsequently using a physical beam block, e.g. an iris, to fully remove the zero order beam in a conjugate plane. This technique though limits the accessible region in the final reconstruction, since any part of the target pattern close to the zero order beam could also be affected. In spite of limiting the accessible region, we have decided to use the latter approach as it is easy to realize experimentally and does not have any significant drawbacks when compared to the other techniques.

3.3 Aberration correction

Aberrations are errors in the phase of the wavefront and are commonly expressed as an expansion in so-called *Zernike polynomials* [77], which were first derived by the Dutch physicist Frits Zernike in 1934. The wavefront can be decomposed into a superposition of orthogonal Zernike polynomials, where each polynomial accounts for a specific aberration.

In general, any arbitrary wavefront can be expanded in terms of a sequence of Zernike polynomials using the polar coordinates (ρ, ϕ) , resulting in

$$W(\rho, \phi) = \sum_{m,n} C_n^m Z_n^m(\rho, \phi). \quad (3.2)$$

Here, Z denotes the Zernike polynomials and C the corresponding Zernike coefficient, while m and n are non-negative integers obeying the relation $n \geq m \geq 0$. One now distinguishes between *even* and *odd* Zernike polynomials. Even Zernike polynomials are defined as

$$Z_n^m(\rho, \phi) = R_n^m(\rho) \cos(m\phi), \quad (3.3)$$

meaning that they are even with respect to the azimuthal angle ϕ . Odd Zernike polynomials are consequently odd with respect to ϕ and therefore take the form

$$Z_n^{-m}(\rho, \phi) = R_n^m(\rho) \sin(m\phi). \quad (3.4)$$

The radial distance ρ is restricted to the unit circle ($0 \leq \rho \leq 1$), and the azimuthal angle ϕ is measured clockwise from the y -axis. The radial polynomials R_n^m are defined as

$$R_n^m(\rho) = \sum_{k=0}^{\frac{n-m}{2}} \frac{(-1)^k (n-k)!}{k! (\frac{n+m}{2} - k)! (\frac{n-m}{2} - k)!} \rho^{n-2k} \quad (3.5)$$

for $n - m$ being even, while $R_n^m(\rho) = 0$ for an odd number of $n - m$. Figure 3.4 displays the first 10 orders of Zernike polynomials, ordered horizontally by the azimuthal degree and vertically by the radial degree.

To correct for optical aberrations, we can make use of the orthogonality of the Zernike polynomials. For every Zernike polynomial, we can adjust its

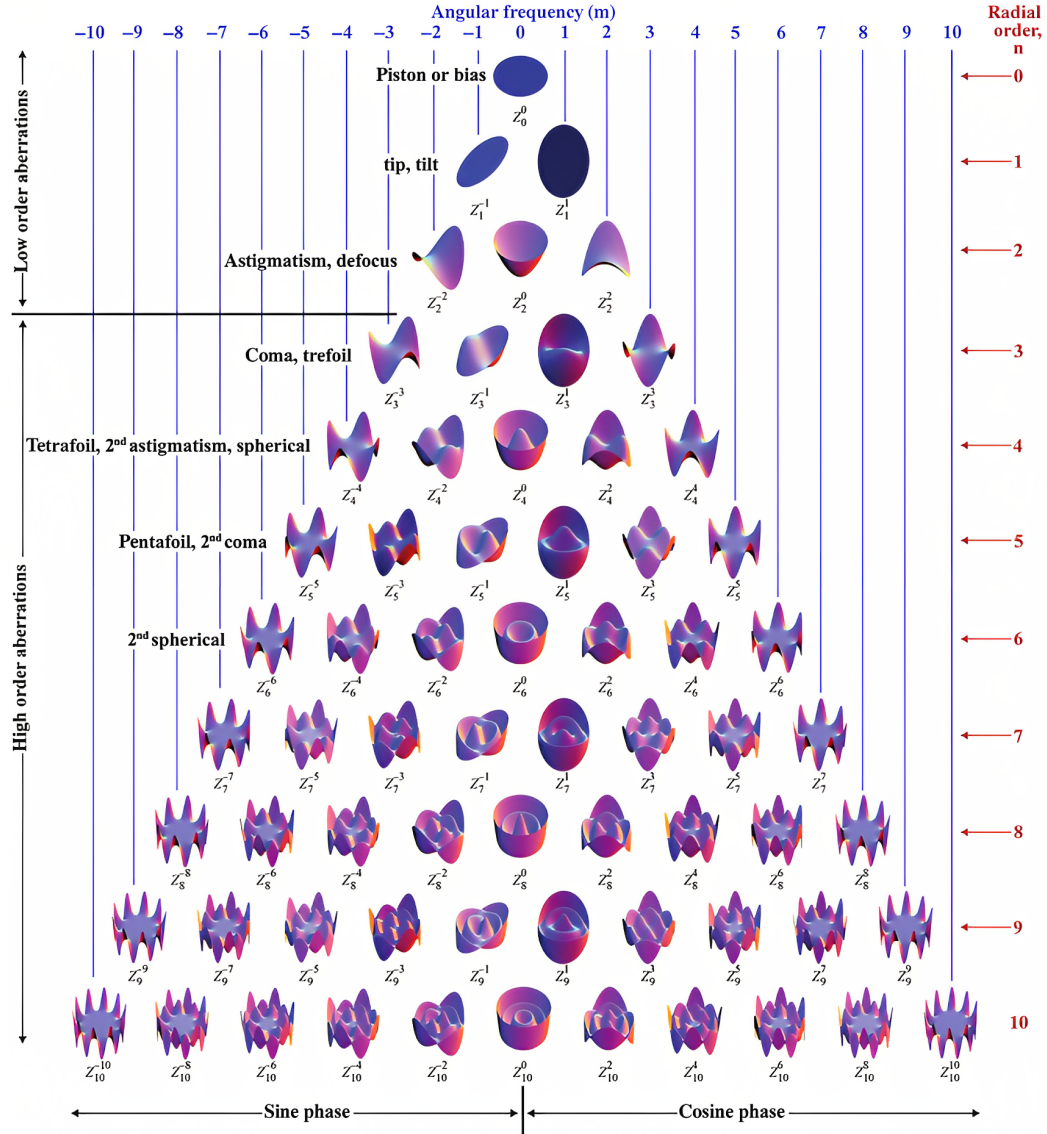


Figure 3.4: Surface plot of the first 10 orders of Zernike polynomials. The name of the associated optical aberrations is provided. Taken from Ref. [77].

coefficient (both negative and positive) in predefined steps. After every step, we apply the slightly changed hologram to the SLM and the camera records an image of the intensity distribution of the first order diffraction beam in the Fourier plane. The image providing maximum intensity, i.e. an optimized Strehl ratio, is then determined and its corresponding coefficient is regarded as the optimal value. Once this value is set, we repeat the same procedure for the next Zernike polynomial. The aberration correction algorithm as explained above is summarized in the flow chart in Fig. 3.5.

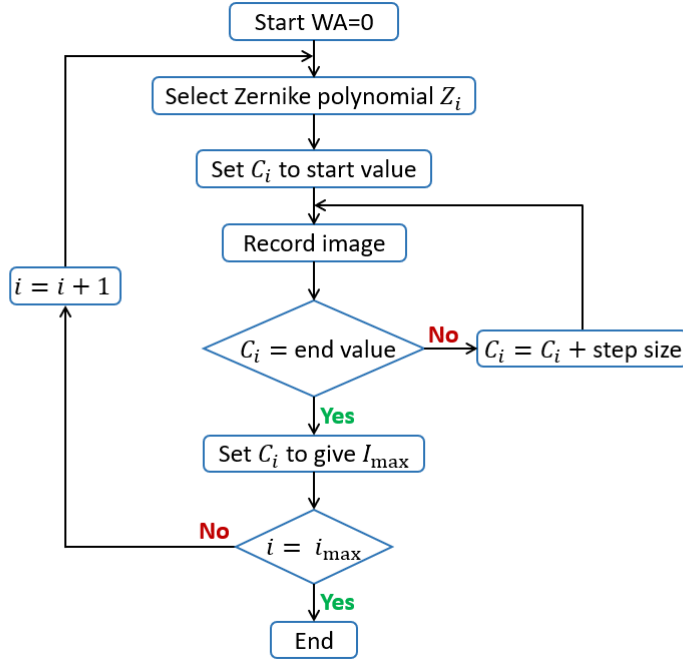


Figure 3.5: Flow chart of the algorithm used for aberration correction. We initially set the coefficients of all Zernike polynomials to zero, meaning we do not assume any wavefront aberration (WA). We then select a Zernike polynomial Z_i and vary its corresponding coefficient C_i by a certain step size in every iteration, where i accounts for both n and m . After each step, we measure the intensity of the first order beam and eventually, the coefficient resulting in the intensity maximum I_{\max} is set as the ideal value. This procedure is then repeated for the next Zernike polynomial Z_{i+1} and can be terminated as desired.

3.4 Phase retrieval algorithms

The creation of arbitrary light patterns using phase-only LC SLMs turns out to be quite challenging and the reason for this is as follows: assuming one knows both the phase and the amplitude of the input light field (e.g. a Gaussian laser beam), what is the hologram one needs to apply to the LC SLM to obtain the correct phase modulation producing the desired intensity pattern in the far field? Here, the Fourier transform is employed to model this far-field diffraction and it can be experimentally realized either by focusing the modulated beam with a lens, or by observing the diffracted light at large distances. The task of recovering a signal from its Fourier transform magnitude is now referred to as *phase retrieval* and can mathematically be achieved by solving the equation

$$\mathcal{F}\{A_0(x, y)e^{i(\theta(x, y) + \phi(x, y))}\} = A_T(u, v)e^{i\varphi(u, v)}, \quad (3.6)$$

where \mathcal{F} denotes the Fourier transform. The expression $A_0(x, y)e^{i\theta(x, y)}$ describes the input beam, $A_T(u, v)e^{i\varphi(u, v)}$ the target field and $\phi(x, y)$ the corresponding phase modulation.

Naively, one would approach this problem by simply taking the inverse Fourier transform of the target field to calculate the required phase modulation at the LC SLM. However, this approach is not feasible as it would eventually require a modulation of both the phase *and* the amplitude of the input light, whereas only phase modulation is possible. Instead, one usually attempts to numerically calculate a phase modulation that results in an optimized intensity pattern in the Fourier plane. Here, the most conventional phase retrieval methods used are *iterative Fourier transform algorithms* (IFTAs).

3.4.1 Gerchberg-Saxton (GS) algorithm

The GS algorithm is very powerful and arguably the most common IFTA. It is a numerical method and its implementation relies on linking the SLM plane and the Fourier plane by simulating the light propagation back and forth via the Fourier transform. When using a lens of focal length f to create the Fourier transform, the lens is placed a distance f away from the SLM plane and the corresponding Fourier plane is defined as the plane a

distance $2f$ away from the LC SLM. After every propagation between these two planes, one imposes the appropriate amplitude constraint in the corresponding plane, while leaving the phase to converge. As a result of the phase freedom in both planes, the phase eventually evolves towards an acceptable solution after a sufficient number of iterations.

A diagram of the GS algorithm is shown in Fig. 3.6 and for reasons of brevity, we omit the use of spatial coordinates and additionally assume $\theta(x, y) = 0$, i.e. the incident light field is modelled to have a uniform phase. The starting point of the calculation is now formed by the input light field

$$E_{\text{in}}^{(1)} = A_0 e^{i\phi_0}, \quad (3.7)$$

where A_0 denotes the incident amplitude and ϕ_0 an initial guess of the phase modulation to be calculated. Here, the algorithm is typically initialized using a random phase pattern for ϕ_0 , where the value of every pixel is randomly distributed in the range from 0 to 2π . The second step consists of going from the SLM plane to the Fourier plane by realizing the far-field diffraction of the LC SLM. This step is achieved by applying the Fast Fourier Transform (FFT) to the input light field and results in

$$E_{\text{out}}^{(1)} = \text{FFT} \left(E_{\text{in}}^{(1)} \right) = A_{\text{out}}^{(1)} e^{i\varphi^{(1)}}, \quad (3.8)$$

where $A_{\text{out}}^{(1)}$ is the amplitude of the output light field and $\varphi^{(1)}$ its corresponding phase. The first amplitude constraint is then imposed by replacing $A_{\text{out}}^{(1)}$ with the target amplitude $A_T = \sqrt{I}$, while the phase is left unchanged, taking the form

$$G_{\text{out}}^{(1)} = A_T e^{i\varphi^{(1)}}. \quad (3.9)$$

The next step now is propagating back to the SLM plane via the Inverse Fast Fourier Transform (IFFT), leading to

$$G_{\text{in}}^{(1)} = \text{IFFT} \left(G_{\text{out}}^{(1)} \right) = A_{\text{in}}^{(1)} e^{i\phi^{(1)}}, \quad (3.10)$$

where $A_{\text{in}}^{(1)}$ is the resulting amplitude and $\phi^{(1)}$ the phase. Subsequently, the second amplitude constraint is imposed by replacing the resulting amplitude with the amplitude A_0 of the incident light field, which gives

$$E_{\text{in}}^{(2)} = A_0 e^{i\phi^{(1)}}. \quad (3.11)$$

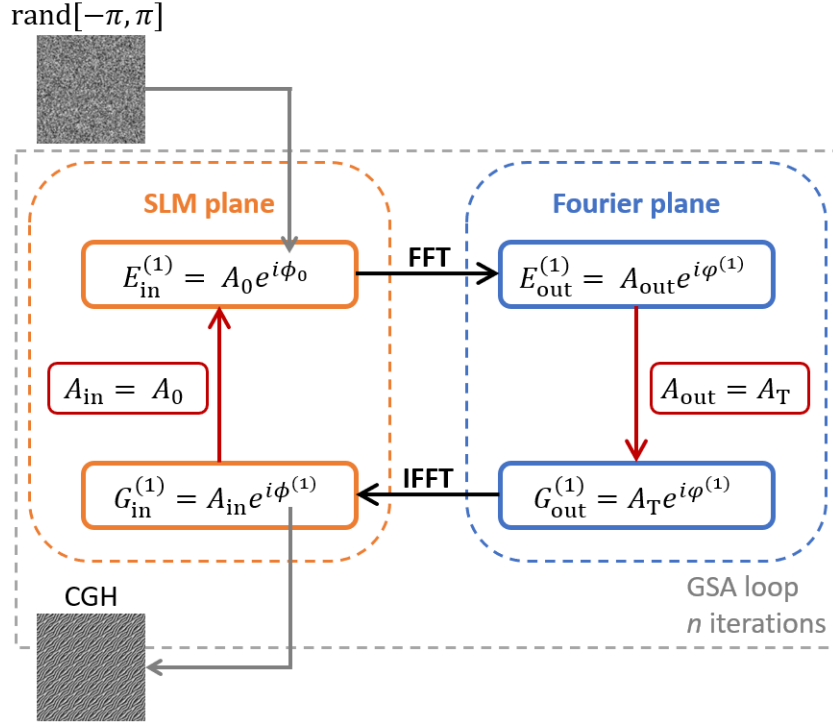


Figure 3.6: Diagram of the GS algorithm. The Fourier transform links the SLM plane to the Fourier plane. After each propagation, one imposes the amplitude constraints $A_{\text{in}} = A_0$ and $A_{\text{out}} = A_T$, while leaving the phase ϕ to converge. Numerous iterations typically need to be conducted to be able to reconstruct the target image satisfactorily.

The procedure as described above forms the first iteration of the GS algorithm. Typically, further iterations are required in order to obtain a satisfactory result for the phase modulation. Termination of the calculation process occurs either after a specified limit in terms of its number of iterations, or after the deviation between the output amplitude A_{out} and the target amplitude A_T falls below a certain threshold.

Note that both the phase pattern, as well as the target image, which are used as an input for the GS algorithm, need to have identical height and width. If this is not the case, the reconstructed optical image stretches or shrinks accordingly, dependent on the ratio between its height and width. Therefore, we choose the size of these input images to be 1024×1024 LC

SLM pixels. However, as the final phase pattern needs to cover the entire area of the LC SLM, which are 1024×1272 pixels, the calculated phase pattern is concatenated and subsequently cut to the appropriate size.

A significant drawback of the GS algorithm is that the recreated intensity distributions typically suffer from imperfections in the form of intensity non-uniformities, which can pose a major problem when trying to generate an array of identical optical tweezers. In order to improve the uniformity of the target image, several modifications of the GS algorithm have been proposed so far. The so-called *weighted Gerchberg-Saxton* algorithm has proven to be an efficient approach and is based on the additional incorporation of the reconstructed image as feedback.

3.4.2 Weighted Gerchberg-Saxton (WGS) algorithm

As a means of increasing the uniformity of the reconstructed image, the WGS algorithm was recently proposed [78, 79]. It is an approach where the deviation between the intensity of the target image and the intensity of the reconstructed image is calculated. This deviation is then used as feedback to restrict the intensity of the image plane by weighting each spot accordingly. The way we define the weight w reads

$$w = e^{G(I_T - I_{\text{out}})}, \quad (3.12)$$

where I_T and I_{out} denote the intensity of the target image and the reconstructed image, respectively. The parameter G is in the following referred to as *gain* and it can increase the speed of convergence when chosen appropriately. Here, our definition of the weight w used for feedback is based on the comprehensive discussion presented in Ref. [80]

The only difference between the GS algorithm and the WGS algorithm lies in the amplitude restriction in the Fourier plane. As shown previously, in the GS algorithm in Fig. 3.6, the first amplitude constraint in the Fourier plane is imposed by simply replacing A_{out} with the target amplitude $A_T = \sqrt{I_T}$. In the WGS algorithm on the other hand, the target amplitude is additionally weighted accordingly using the weight w , resulting in the amplitude constraint $A_{\text{out}} = w \cdot A_T$ instead. This procedure is done for every iteration, and the weights need to be calculated again after every iteration as they keep

changing. Again, the algorithm can either be stopped by setting a limit to the number of iterations, or after the reconstructed amplitude A_{out} resembles the target amplitude A_{T} well within a certain error.

3.5 Calculation of target patterns

In the previous section, we have discussed how to calculate the phase patterns via phase retrieval algorithms. In our case, these algorithms require input in the form of an 8-bit grayscale image in the size of 1024×1024 pixels. This image reflects the intensity distribution we would like to create, e.g. a rectangular lattice of 6×6 traps with a separation of 10 pixels, where each trap corresponds to exactly one pixel. However, we have not yet discussed how the spot separation in terms of pixels in the SLM plane actually transfers to a separation in terms of microns in the focal plane. We now discuss the mathematical relation between these two planes, as it provides a convenient way of choosing the separation in the SLM plane according to experimental needs in the focal plane.

As illustrated in Fig. 3.7, the LC SLM we are using is comprised of discrete pixels in a grid of $N_\xi \times N_\eta = 1024 \times 1272$, with a pixel size of $\Delta\xi \times \Delta\eta = 12.5 \mu\text{m} \times 12.5 \mu\text{m}$. Following the treatment of Ref. [81], $\Delta\xi \times \Delta\eta$ defines a unit cell in the SLM plane. Similarly, the maximum physical size of the incident light in the SLM plane is determined by the active area of the LC SLM and reads $L_\xi \times L_\eta = N_\xi \Delta\xi \times N_\eta \Delta\eta = 15.9 \text{ mm} \times 12.8 \text{ mm}$. We now are interested in how these parameters transform when being viewed in the focal plane of the lens (f_3 in Fig. 4.1) focussing down on the camera. In this focal plane, as depicted in Fig. 3.7, the physical dimension of a unit cell reads

$$\Delta x \times \Delta y = \frac{\lambda f_{\text{eff}}}{N_x \Delta\xi} \times \frac{\lambda f_{\text{eff}}}{N_y \Delta\eta} = \frac{\lambda f_{\text{eff}}}{L_\xi} \times \frac{\lambda f_{\text{eff}}}{L_\eta}, \quad (3.13)$$

where f_{eff} denotes the effective focal length, λ the wavelength of the incident light and $N_x \times N_y$ the number of "pixels" or unit cells in the focal plane. The effective focal length accounts for all lenses after the LC SLM as included in the optical setup (see Fig. 4.1) and therefore takes the form

$$f_{\text{eff}} = \frac{f_1}{f_2} \cdot f_3. \quad (3.14)$$

For computational reasons, one chooses $N_x \times N_y = N_\xi \times N_\eta$, where we refer the reader to Ref. [81] for further explanation. Similar to the SLM plane, there exist $N_x \times N_y$ such unit cells in the focal plane, giving rise to a "signal window" of the size $L_x \times L_y = N_x \Delta x \times N_y \Delta y$. The size of the signal window defines the area in the focal plane within which we can ultimately create the desired intensity distribution.

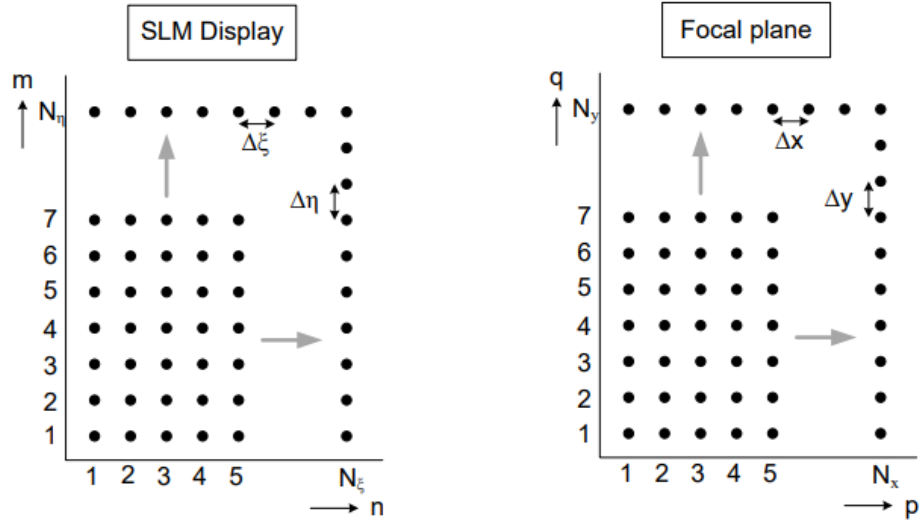


Figure 3.7: The display of the LC SLM is comprised of $N_\xi \times N_\eta$ pixels of the size $\Delta\xi \times \Delta\eta$. In comparison, the field in the focal plane has an equal amount of unit cells, but with the size $\Delta x \times \Delta y$. Taken from Ref. [81]

As we can see, the discretized grid of pixels in the SLM plane yields a discretized grid of unit cells in the focal plane. Consequently, the unit cell $\Delta x \times \Delta y$ corresponds to the smallest possible shift. Assuming that the entire LC SLM is illuminated, the unit cell in the focal length amounts to $\Delta x \times \Delta y = 14.3 \mu\text{m} \times 11.51 \mu\text{m}$. However, we need to keep in mind that, in our experiment, the diameter of the beam incident on the LC SLM measures approximately 13 mm and therefore does not cover the active area of the LC SLM horizontally. For our calculations, we consequently decide to use $L_\xi \times L_\eta = 12.8 \text{ mm} \times 12.8 \text{ mm}$ as an approximation. The unit cell in the focal plane then takes the values $\Delta x \times \Delta y = 14.3 \mu\text{m} \times 14.3 \mu\text{m}$, setting the smallest scale with which we can ultimately control the optical tweezer array.

Note that the size of the unit cell in the focal plane as we report above is a result we obtain while testing the LC SLM, and is much too big for our actual experimental needs. However, according to Eq. (3.13), one can easily adjust the size of the unit cell, either by modifying f_{eff} by using different lenses, or by altering the diameter of the incident beam correspondingly.

Chapter 4

Generating holographic 2D optical tweezer arrays

After reviewing how to operate the LC SLM and providing an overview of the requirements of its input image in Chap. 3, this chapter presents the experimental implementation of the LC SLM and some first results. In Sec. 4.1, we discuss our optical setup. While Sec. 4.2 focuses on the calibration of an LC SLM, we briefly discuss our choice of blazed grating in Sec. 4.3. In Sec. 4.4, we present the results we obtain when conducting our aberration correction procedure. Finally, Sec. 4.5 demonstrates our first optical tweezer arrays, where we generate a rectangular array of 6×6 traps and compare the results we obtain via the GS algorithm with the ones of the WGS algorithm.

4.1 Optical setup

We first begin by presenting the optical setup shown in Fig. 4.1. We use a 486 nm laser, which we couple into a polarization-maintaining fiber. The light emitted by the fiber is then directed to the LC SLM. When building the setup, one has to pay attention to a few aspects: Firstly, the incidence angle of the laser beam on the LC SLM head should be less than or equal to 5° to maintain good phase modulation [82]. Secondly, the laser beam should be incident with horizontal polarization, i.e. perfectly parallel to the plane containing the incident and reflected beam. The required direction of polarization is set by the polarizing beam splitter (PBS) cube. An additional half-wave plate ($\lambda/2$) is implemented to be able to control the intensity, which

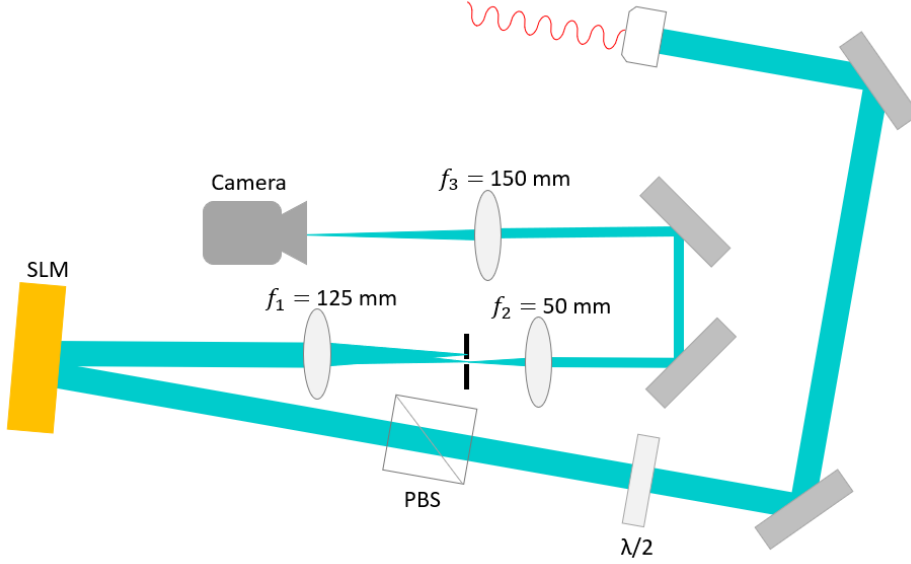


Figure 4.1: Optical setup. The light comes from a polarization-maintaining fiber and its polarization is cleaned by a polarizing beam splitter (PBS) cube. The PBS cube in combination with the half-wave plate ($\lambda/2$) allows for controlling the polarization and intensity of the light incident on the LC SLM. An additional set of lenses is employed after the LC SLM to change the beam size and block the unmodulated zero order spot before hitting the CCD camera.

is either reflected or transmitted by the PBS cube, dependent on the light's polarization. The phase-modulated light reflected off the LC SLM is then focused using an achromatic lens with the focal length $f_1 = 125$ mm. This lens is a distance f_1 away from the LC SLM and performs a Fourier transform of the beam (corresponding to the Fourier transform in the GS algorithm in Sec. 3.4.1). The intensity distribution associated with the phase modulation is obtained in the Fourier plane a distance f_1 away from the lens ($2f_1$ away from the LC SLM). We then use an iris in the Fourier plane to block the zero order spot without significantly affecting the desired image. Subsequently, a $4f$ system with a magnification of 3 ($f_2 = 50$ mm and $f_3 = 150$ mm) is used to both recollimate the beam and change the size of its focal spot. The final measurements of the intensity distribution are taken by placing a CCD camera in the Fourier plane of the last lens.

4.2 LC SLM calibration

Note that the LC SLM we are using is designed to achieve a phase modulation of up to 2.28π at the maximum design wavelength. Independent of the specific wavelength, this design therefore always ensures a phase modulation of at least 2π . As we have discussed in the previous chapter, the phase modulation of the LC SLM varies dependent on the wavelength of the input light, which essentially means that applying the same gray level to two different wavelengths yields different phase modulation depths. We can correct for this by introducing the parameter g in Eq. (3.1), which corresponds to the gray level value yielding a phase shift of 2π at the wavelength of interest. In our case, this parameter is already provided by the manufacturer, i.e. we do not have to carry out the calibration procedure ourselves. The manufacturer suggests $g = 194$ for a wavelength of 486 nm. In case the value is not provided and for completeness, we briefly want to present how these calibration measurements could be conducted.

In general, the goal of calibrating the LC SLM is to obtain a relation between the input gray level values and the corresponding phase pattern of the LC SLM. A variety of different calibration procedures has been proposed in literature, which can be sorted in two distinct categories: the diffractive phase calibration and the interferometric phase calibration. Both methods are widely applied and a comprehensive explanation can be found in Ref. [83].

In Ref. [84], an interferometric phase calibration method is proposed, which entirely relies on the LC SLM itself and, unlike other methods, does not require additional optical components. It is therefore commonly used and is worth discussing. In brief, the LC SLM is configured to simultaneously display a different phase pattern on each half. As depicted in Fig. 4.2 (a) (left panel) and Fig. 4.2 (b) (left panel), one half is addressed with a uniform gray level value, while the other half displays a vertically-oriented binary diffraction grating. While the uniform gray level value of the first half is varied during the calibration procedure, the diffraction grating remains static. When illuminating these specific phase patterns with a collimated beam, the binary grating diffracts a considerable amount of the incident beam into the ± 1 diffraction orders under certain angles (dependent on the grating period), whereas the uniform half results in a non-deflected beam with a certain phase

shift (dependent on the gray level value). Both beams then overlap and yield an interferometric pattern in the form of interference fringes, as shown in Fig. 4.2 (a) (right panel) and Fig. 4.2 (b) (right panel). Here, the entire phase shift information is carried by the non-deflected beam. Figure 4.2 shows that, upon changing the gray level value of the uniform half, the position of the fringes changes accordingly. By determining the fringe position, the desired relation between the displayed gray level value and the corresponding phase shift can be obtained [84].

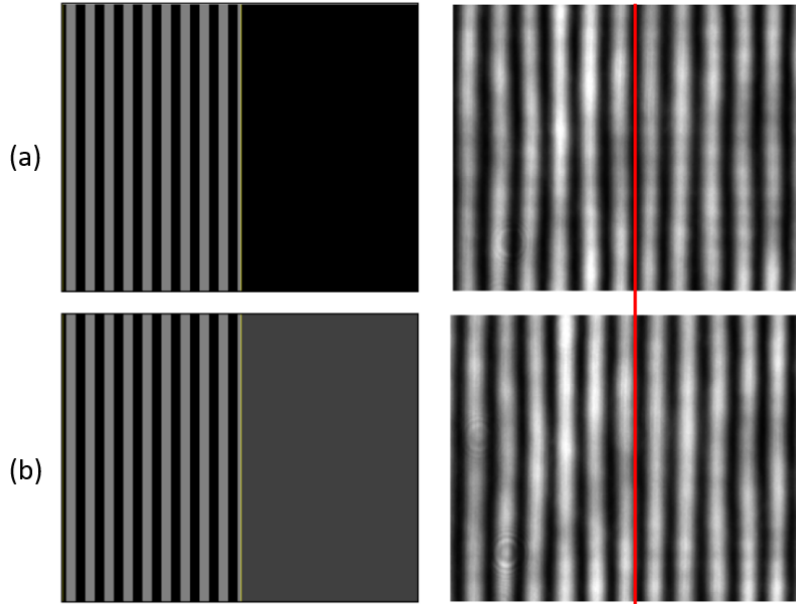


Figure 4.2: Examples of phase patterns and corresponding interference fringes for different gray levels of the right half of the LC SLM. (a) 0. (b) 63. The red line is added to confirm the displacement of the fringe position. Adapted from Ref. [84].

4.3 Choosing the blazed grating

In Sec. 3.2, we have already discussed the reason for additionally having to add a blazed grating to the phase pattern of the LC SLM. Figure 4.3 shows the blazed grating we apply to the LC SLM, which has a period of 10 LC SLM pixels or 10 gray levels, respectively.

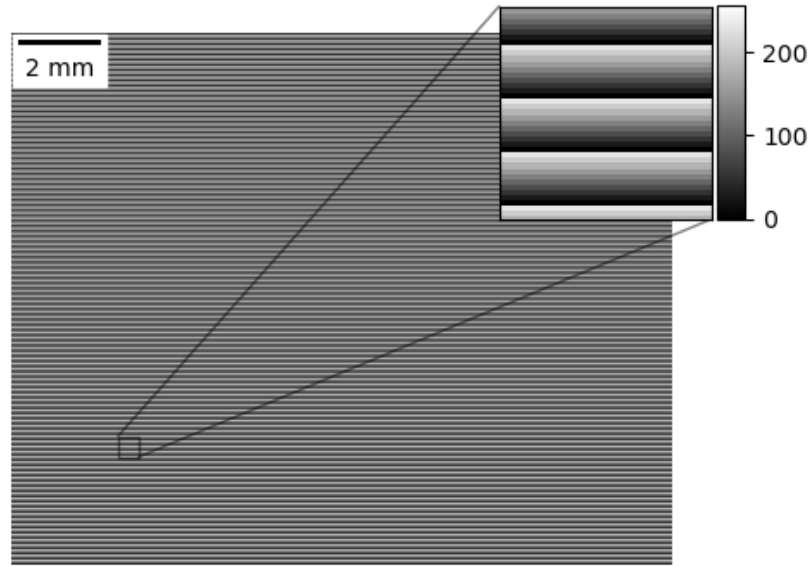


Figure 4.3: Blazed grating with a period of 10 pixels. The image is a grayscale image and therefore has values in the range of 0 to 255. A period of 10 pixels corresponds to 10 different gray levels per period.

When choosing the period of the grating, there is a trade-off between the diffraction efficiency and the diffraction angle. On the one hand, we want to have a large diffraction efficiency so we do not "waste" light. On the other hand, we also desire to obtain a large enough separation between the zero and first order to be able to block the zero order successfully. To determine the diffraction efficiency, we display blazed gratings with a different number of pixels per period, each pixel corresponding to a gray level between 0 and 255, i.e. an 8-bit signal. For each grating, the first order diffraction intensity is measured and the resulting diffraction efficiency is presented in Fig. 4.4.

Note that we did not specifically determine the separation between the individual diffraction orders as a function of the spatial frequency of the blazed grating. Instead, we tried different values for the grating period and eventually decided to use a period of 10 pixels, as it led to a satisfactory separation between the spots on the camera. For the future though, we strongly suggest to measure the correspondence between the spot separation on the camera and the grating period. Furthermore, note that, dependent on the size of the

intensity pattern one wants to display, a different grating period might have to be chosen such that the zero order beam and the modulated first order beam do not overlap.

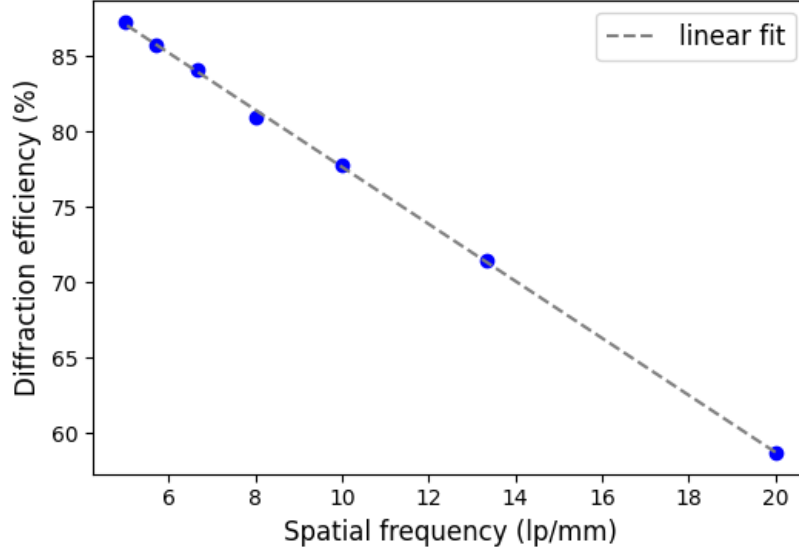


Figure 4.4: Measured diffraction efficiency as a function of the spatial frequency expressed in line pairs per millimeter (lp/mm). The dashed line shows a linear fit of the form $f(x) = kx + d$ with the fit parameters $k = -1.89(2) \frac{\%}{\text{lp/mm}}$ and $d = 96.6(2) \%$.

4.4 Aberration correction

We correct for aberrations in our system as presented by the flow chart in Fig. 3.5. Figure 4.5 (a) displays the resulting Zernike coefficients. Here, we conduct the aberration correction measurements starting with the radial order $n = 2$, corresponding to the third row in Fig. 3.4. We skip the first two rows with $n = 0$ and $n = 1$ in the aberration correction procedure as these are not "true" optical aberrations. More accurately, they do not model the actual curvature of the wavefront, but rather characterize its surface positioning. Here, the constant $n = 0$ order (=piston aberration) only corresponds to an offset in height, while the $n = 1$ order (=tilt aberration) accounts for misalignment or tilts.

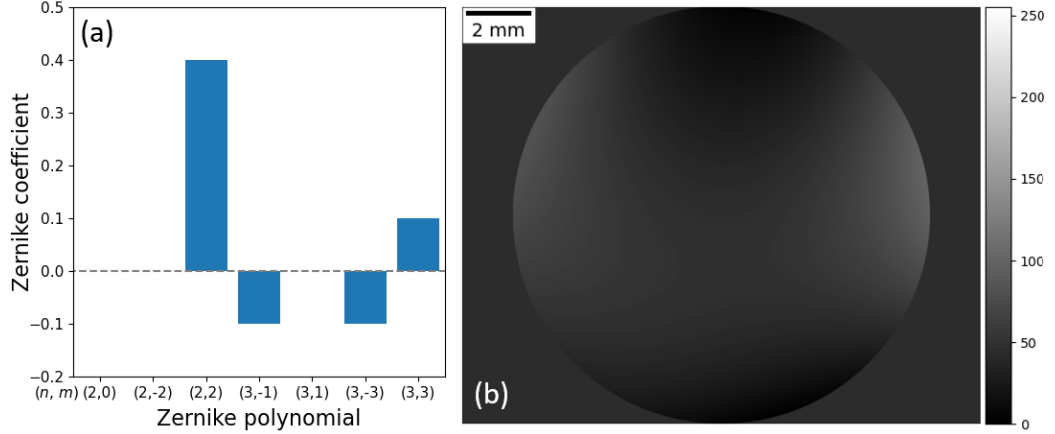


Figure 4.5: Aberration correction via Zernike polynomials. (a) The measured Zernike coefficients are shown, where we do not take into account the first two orders of Zernike polynomials ($n = 0$ and $n = 1$) as they are not "true" aberrations. We determine aberrations in the form of vertical primary astigmatism ($C_2^2 = 0.4$), vertical coma ($C_3^{-1} = -0.1$), vertical trefoil ($C_3^{-3} = -0.1$) and horizontal trefoil ($C_3^3 = 0.1$). (b) The phase pattern corresponding to the measured Zernike coefficients is an 8-bit grayscale image with a resolution of 1024×1272 .

The Zernike polynomial with the orders $n = 2$ and $m = 0$, where its corresponding Zernike coefficient is denoted C_2^0 in Fig. 3.4, accounts for defocus as a wavefront aberration. As shown in Fig. 4.5 (a), we determine $C_2^0 = 0$, which means that our optical system does not exhibit any defocus. Similarly, we find that $C_2^{-2} = 0$ and $C_2^2 = 0.4$, with these Zernike coefficients accounting for oblique primary and vertical primary astigmatism, respectively. While there appears to be no optical aberration in the form of oblique primary astigmatism, vertical primary astigmatism in the optical system can be identified. The presence of this type of astigmatism typically indicates misalignment of the optical components. Additionally, large angles of incidence on the LC SLM could also introduce astigmatism, where the effective pixel structure ends up being slightly denser in one direction [68]. Moving on to third order aberrations, we have the Zernike polynomials describing vertical coma with the Zernike coefficient $C_3^{-1} = -0.1$, horizontal coma with $C_3^1 = 0$, vertical trefoil with $C_3^{-3} = -0.1$, and horizontal trefoil with $C_3^3 = 0.1$. We can de-

termine that both the vertical coma and the vertical trefoil exhibit non-zero Zernike coefficients and are therefore present in the optical system. Pressure on mounting elements in particular can give rise to some form of trefoil, which can also be thought of as a three-winged form of astigmatism, as nicely illustrated in Fig. 3.4.

Figure 4.5 (b) displays the phase pattern corresponding to these Zernike coefficients. This phase pattern needs to be superimposed with both the compensation pattern (Fig. 3.2) and the blazed grating (Fig. 4.3) when applied to the LC SLM. Figure 4.6 (a) displays the first order diffracted beam without aberration correction. Note that the spot has an elliptical shape as a result of the aberrations as listed above. We analyze the quality of the spot by fitting a two-dimensional Gaussian function in the form of

$$G(x, y) = z_0 + A \exp \left(- \left(\frac{(x - x_0)^2}{2\sigma_x^2} + \frac{(y - y_0)^2}{2\sigma_y^2} \right) \right) \quad (4.1)$$

to the data. Here, the coefficient z_0 denotes the offset, A the maximum intensity, x_0 and y_0 the center, and σ_x and σ_y the standard deviations in the x - and y -direction, respectively. The relation with the full width at half maximum (FWHM), which is denoted as W in the following, is given by

$$W_i = \sqrt{2 \ln(2)} \sigma_i, \quad (4.2)$$

with $i = x, y$. Accordingly, we determine FWHMs of $W_x = 14.36(4) \mu\text{m}$ and $W_y = 18.90(6) \mu\text{m}$ for the spot in Fig. 4.6 (a), where no aberration correction is applied. Figure 4.6 (b) on the other hand shows the spot when additional aberration correction is applied. We see a significant improvement of the beam quality as we obtain $W_x = 15.12(2) \mu\text{m}$ and $W_y = 15.26(2) \mu\text{m}$ instead. As mentioned before, the aberration correction scheme is based on finding the Zernike coefficients resulting in the maximum intensity of the first diffraction order. This condition of maximizing the intensity is also nicely reflected by the maximum intensity A as a fit parameter. Normalizing to the maximum intensity I_{max} after the aberration correction, we find that the intensity before the aberration correction is $I_{\text{before}} = 0.817(5) I_{\text{max}}$, while we obtain $I_{\text{after}} = 1.000(3) I_{\text{max}}$ afterwards.

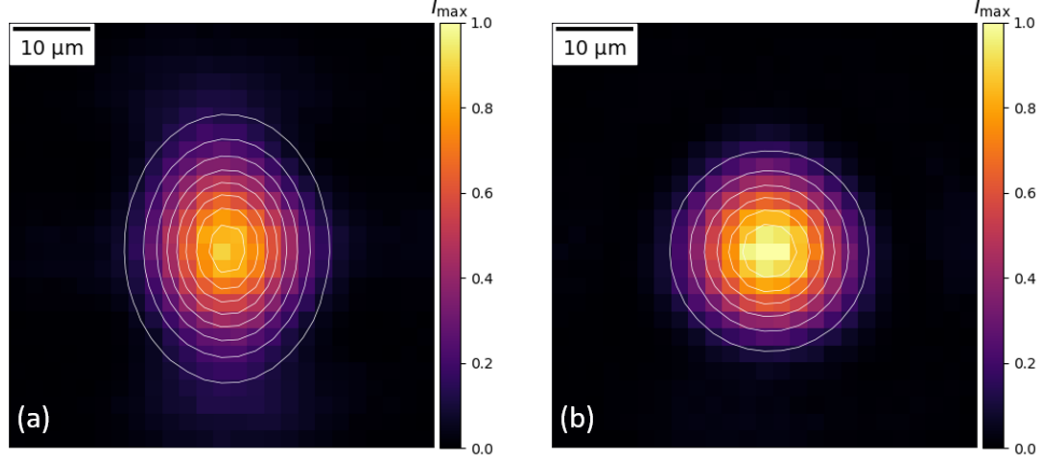


Figure 4.6: First order diffraction spot before and after aberration correction. (a) The first order diffraction spot before correcting for aberrations exhibits an elliptical shape, where the quality is determined by fitting a two-dimensional Gaussian function as indicated by the white lines. (b) The quality of the spot improves significantly when correcting for aberrations. Again, the two-dimensional Gaussian fit is indicated by the white lines.

4.5 Rectangular optical tweezer array

GS algorithm

We first test the functioning of the GS algorithm as introduced in Sec. 3.4.1. Here, the target pattern is a rectangular lattice of 6×6 traps with a separation of 10 pixels, where each trap corresponds to one pixel. Figure 4.7 shows what the phase pattern (ϕ_{target} in Eq. (3.1)) looks like after 50 iterations of the GS algorithm. For its computation, we additionally assume $A_0 = 1$, which means the input beam has spatially uniform intensity. The assumption of uniform illumination of the LC SLM is not completely true, as the incident beam is actually Gaussian. However, initially assuming Gaussian illumination would add three additional free parameters, i.e. the width in the x - and y -direction, as well as the position of the beam on the LC SLM. Alternatively, if the Gaussian beam impinging on the LC SLM is significantly bigger than the active area of the LC SLM, one can assume uniform illumination. In our case, the diameter of the incident beam measures approximately 13 mm,

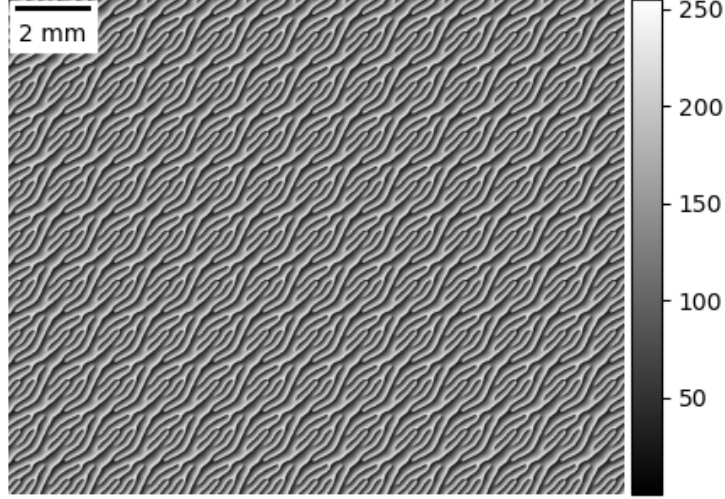


Figure 4.7: Phase pattern after 50 iterations of the GS algorithm for a target pattern of 6×6 traps with a separation of 10 pixels.

which is about the same size as the shorter side of the rectangular active area ($15.9 \text{ mm} \times 12.8 \text{ mm}$) and is therefore not "significantly" bigger. Nevertheless, after testing either option, we are not able to determine a considerable difference. Thus, we implement uniform illumination for reasons of simplicity.

Figure 4.8(a) displays the image one would expect to see in the Fourier plane when applying Fig. 4.7 to the LC SLM, which is $|E_{\text{out}}|^2$ after the last iteration (see Fig. 3.6). In comparison, Fig. 4.8(b) shows the actual image as recorded by the camera when applying the phase pattern given in Fig. 4.7 to the LC SLM (in addition with the flatness correction, the blazed grating and the aberration correction).

In Fig. 4.8(b), we can clearly see an undesired non-uniformity in the intensity of the generated optical tweezer array. We attempt to minimize this issue by using the WGS algorithm instead.

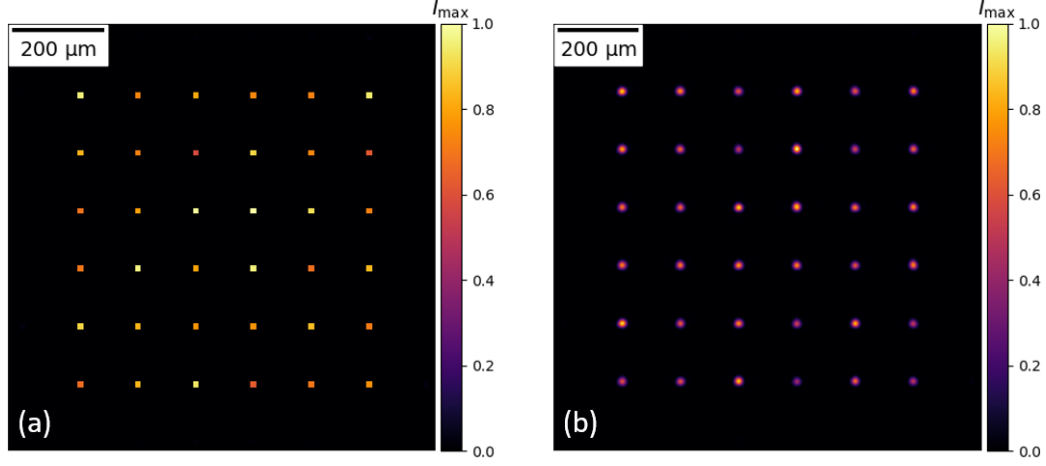


Figure 4.8: Expected and actual image on the camera using the GS algorithm for phase retrieval. (a) Using the final $|E_{\text{out}}|^2$ after the last iteration, one can check what the expected image on the camera when applying the corresponding phase pattern should look like. (b) The intensity distribution of the actual image on the camera looks similar to the theoretical prediction on the left. However, both the reconstructed image and the expected image have a non-uniformity in intensity, which can be dealt with by implementing the WGS algorithm instead.

WGS algorithm

We conduct the WGS algorithm for exactly the same random phase guess and the same target image as for the GS algorithm previously. To better demonstrate the difference in results of both algorithms, Fig. 4.9 (a) again shows the reconstructed image when using the GS algorithm, while Fig. 4.9 (c) depicts the final image on the camera for the WGS algorithm. By eye, we can already observe a significant improvement of the uniformity of the traps, which we quantify by introducing the uniformity

$$u = 1 - \frac{I_{\text{max}} - I_{\text{min}}}{I_{\text{max}} + I_{\text{min}}}, \quad (4.3)$$

where I_{max} and I_{min} denote the maximum and minimum intensity of the spots, respectively. More precisely, we select an area of a certain size including each spot (e.g. the spot position ± 20 camera pixels in the x - and

y -direction), where the summation of the signal within the area is regarded the intensity of the respective spot. By additionally conducting the fitting procedure using a two-dimensional Gaussian function as given in Eq. (4.1), we can analyze the quality of the spots in terms of their spot size. Here, we also want to determine the homogeneity of the spot size. As a measure of the homogeneity of a set of data x , we therefore introduce the standard deviation, which is given by

$$S(x) = \sqrt{\frac{1}{n-1} \sum_{i=1}^n (x_i - \bar{x})^2}, \quad (4.4)$$

where n is the number of spots and x_i the set of data, e.g. the parameter W .

For the spots we obtain via the GS algorithm as shown in Fig. 4.9 (a), we determine a mean spot size of $\overline{W}_x = 15.6(4) \mu\text{m}$ and $\overline{W}_y = 15.6(4) \mu\text{m}$ in the x - and y -direction, respectively. The corresponding uniformity takes a value of around $u = 72.54\%$. As for the spots created via the WGS algorithm displayed in Fig. 4.9 (c), we find a mean spot size of $\overline{W}_x = 15.5(4) \mu\text{m}$ and $\overline{W}_y = 15.5(5) \mu\text{m}$. Here, the uniformity reads approximately $u = 98.15\%$. These results demonstrate that we indeed are able to achieve much better trap uniformity.

Figure 4.9 (b) and Fig. 4.9 (d) display the individual trap intensities for the GS algorithm and the WGS algorithm, respectively. Here, the standard deviations are plotted as shaded areas, while the mean spot intensity is indicated by the dashed lines. It can clearly be seen that the trap intensities vary much less for the WGS algorithm, which confirms the improvement in uniformity as mentioned above.

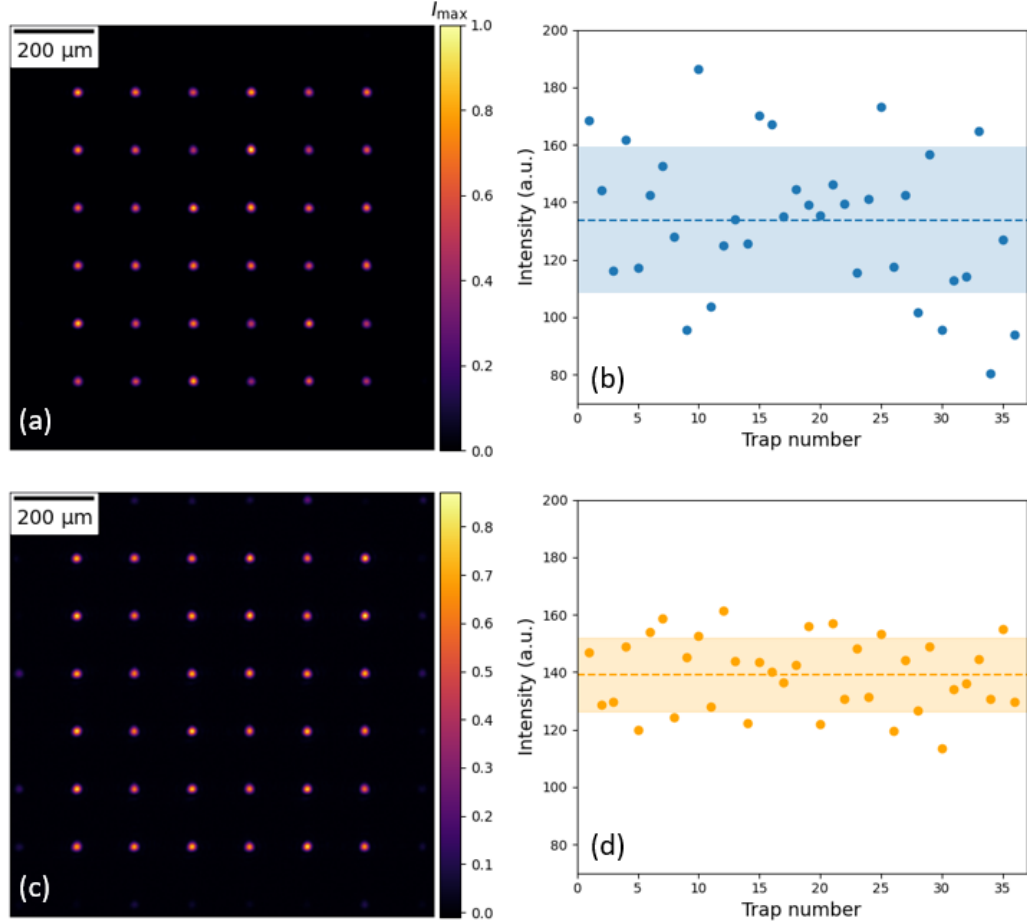


Figure 4.9: Rectangular lattice of 6×6 traps with a separation of 10 pixels. (a) The image is reconstructed via 50 iterations of the GS algorithm and shows considerable non-uniformity in the intensity of the spots. (b) The intensities of the individual traps for the GS algorithm exhibit significant non-uniformity as they vary dramatically. (c,d) We can correct the non-uniformity by utilizing the WGS algorithm. Here, 46 iterations of the WGS algorithm result in an improved uniformity.

Chapter 5

Performance and quality

In this chapter, we want to further analyze the performance of the WGS algorithm and the quality of the reconstructed spots. In Sec. 5.1, we discuss the performance of the weighted Gerchberg-Saxton algorithm (WGS) algorithm using the example of the rectangular 6×6 lattice from the previous chapter. Section 5.2 instead demonstrates the functioning of the WGS algorithm by showing various complex geometries of optical tweezer arrays we are able to generate. Here, we use the same analytical procedure as for the rectangular lattice in the previous chapter to quantify the performance of the WGS algorithm and the quality of the spots. In Sec. 5.3, we very briefly review the scalability of the WGS algorithm, i.e. how many traps we can create with reasonable quality. In the end, Secs. 5.4 and 5.5 focus on the emergence of ghost spots, and the dependence of the spot quality on spot separation, respectively.

5.1 Performance of WGS algorithm

Equation (4.3) quantifies the uniformity of the spot intensities. In Fig. 5.1 (a), we show how the uniformity increases as a function of the number of iterations for the case of the 6×6 rectangular array. Here, the algorithm is set to stop when the deviation between the weakest and brightest spot is less than or equal to 3% of the latter. An alternative method is based on the root mean squared error (RMSE) for all n spots as a condition of termination. The

normalized RMSE is defined as

$$\text{RMSE} = \sqrt{\sum_{i=1}^n \left(\frac{I_{T,i} - I_{\text{out},i}}{I_{T,i}} \right)^2}, \quad (5.1)$$

and is a measure of the deviation between the reconstructed intensity I_{out} and the desired target intensity I_T . Referring to the 6×6 rectangular array, the WGS algorithm conducts 46 iterations until it reaches its terminating condition. Figure 5.1 (a) shows that the corresponding uniformity converges towards 100% with an increasing number of iterations, where we obtain a final uniformity of approximately 98.15%. In addition to the convergence of the uniformity, the convergence of both the weight and the RMSE also indicate that the reconstructed intensity I_{out} approaches the target intensity I_T . We compute the weight as given in Eq. (3.12) and the RMSE as defined in Eq. (5.1). Both results are shown in Fig. 5.1 (b), where the RMSE and the maximum value of the weight w are represented by the blue and green data set, respectively.

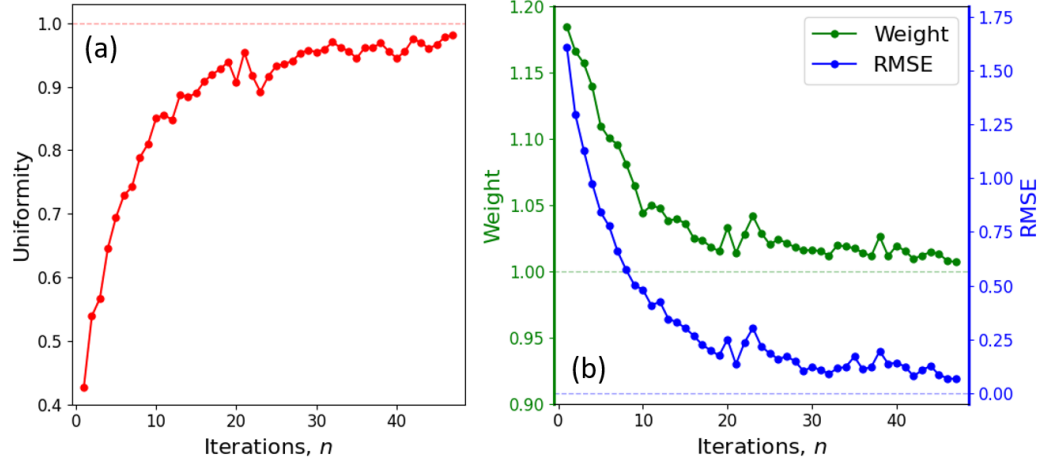


Figure 5.1: Results of the WGS algorithm. (a) The uniformity converges to a value of one, i.e. 100% as the number of iterations increases. Upon reaching the terminating condition after 46 iterations, the uniformity amounts to around 98.15%. (b) As the number of iterations increases, the maximum value of the weight converges to a stable value of one, while the corresponding RMSE approaches zero.

Note that the RMSE gradually converges to a value of zero, which is reasonable, considering that the reconstructed intensity I_{out} is set to approach the target intensity I_{T} . Furthermore, as the number of iteration increases, the weight converges to a stable value of one, as $e^{G(I_{\text{T}}-I_{\text{out}})} \approx 1$ when I_{out} approaches I_{T} . For the above results, we use a gain of $G = 10$. Generally, the choice of the gain depends considerably on how many spots the target image consists of. Empirically, the gain should be increased for an increasing number of spots. If the gain is too low or too high, it might occur that the WGS algorithm does not converge and either undershoots or overshoots instead.

5.2 Gallery of optical tweezer arrays

Besides the creation of rectangular optical tweezer arrays as already discussed, we can create a wide variety of different trap geometries. For instance, Fig. 5.2 displays *circular*, *kagome* and *Lieb* trap geometries. These geometries are particularly relevant for quantum simulation applications. For example, quantum phases have recently been theoretically investigated by arranging Rydberg atoms on a kagome lattice [85]. Another example involves quantum simulation of a topological Mott insulator by utilizing Rydberg atoms in a Lieb lattice [86].

The left column of Fig. 5.2 shows the reconstructed image using the GS algorithm, while the right one displays the results of the WGS algorithm. In all three considered geometries, we observe that the latter provide better performances, as we quantify comparatively in Table 5.1 and 5.2. The analysis of the spot quality and the performance of the WGS algorithm for all three trap configurations is exactly the same as explained previously.

For the GS algorithm, we always set the number of iterations to 50, while for the WGS algorithm this number is set by the 3% tolerance explained above. The number of iterations varies for the different trap geometries. The trap uniformity has significantly increased for the WGS algorithm with respect to the GS algorithm.

Table 5.1: Mean spot size (\overline{W}_x , \overline{W}_y), uniformity u and root mean square error (RMSE) for different trap geometries using the GS algorithm.

Configuration	Iterations	\overline{W}_x (μm)	\overline{W}_y (μm)	u (%)	RMSE (%)
Rectangular	50	15.6(4)	15.6(4)	72.54	16.12
Circular	50	15.5(5)	15.3(5)	78.22	18.54
Lieb	50	15.2(4)	15.3(4)	65.04	31.92
Kagome	50	15.0(3)	15.1(3)	66.01	13.98

Table 5.2: Mean spot size (\overline{W}_x , \overline{W}_y), uniformity u and root mean square error (RMSE) for different trap geometries using the WGS algorithm.

Configuration	Iterations	\overline{W}_x (μm)	\overline{W}_y (μm)	u (%)	RMSE (%)
Rectangular	46	15.5(4)	15.5(5)	98.15	6.55
Circular	23	15.6(4)	15.6(4)	98.56	3.02
Lieb	35	15.5(4)	15.4(4)	98.18	6.59
Kagome	30	15.3(3)	15.1(3)	98.64	3.84

We want to point out that, especially in Fig. 5.2 (d) and Fig. 5.2 (f), one can observe the emergence of so-called *ghost spots*. These are weaker replicas of the desired spots, which are located in between them and are further discussed in Sec. 5.4. Additional discussions and figures on the different geometry and convergence can be found in App. A.

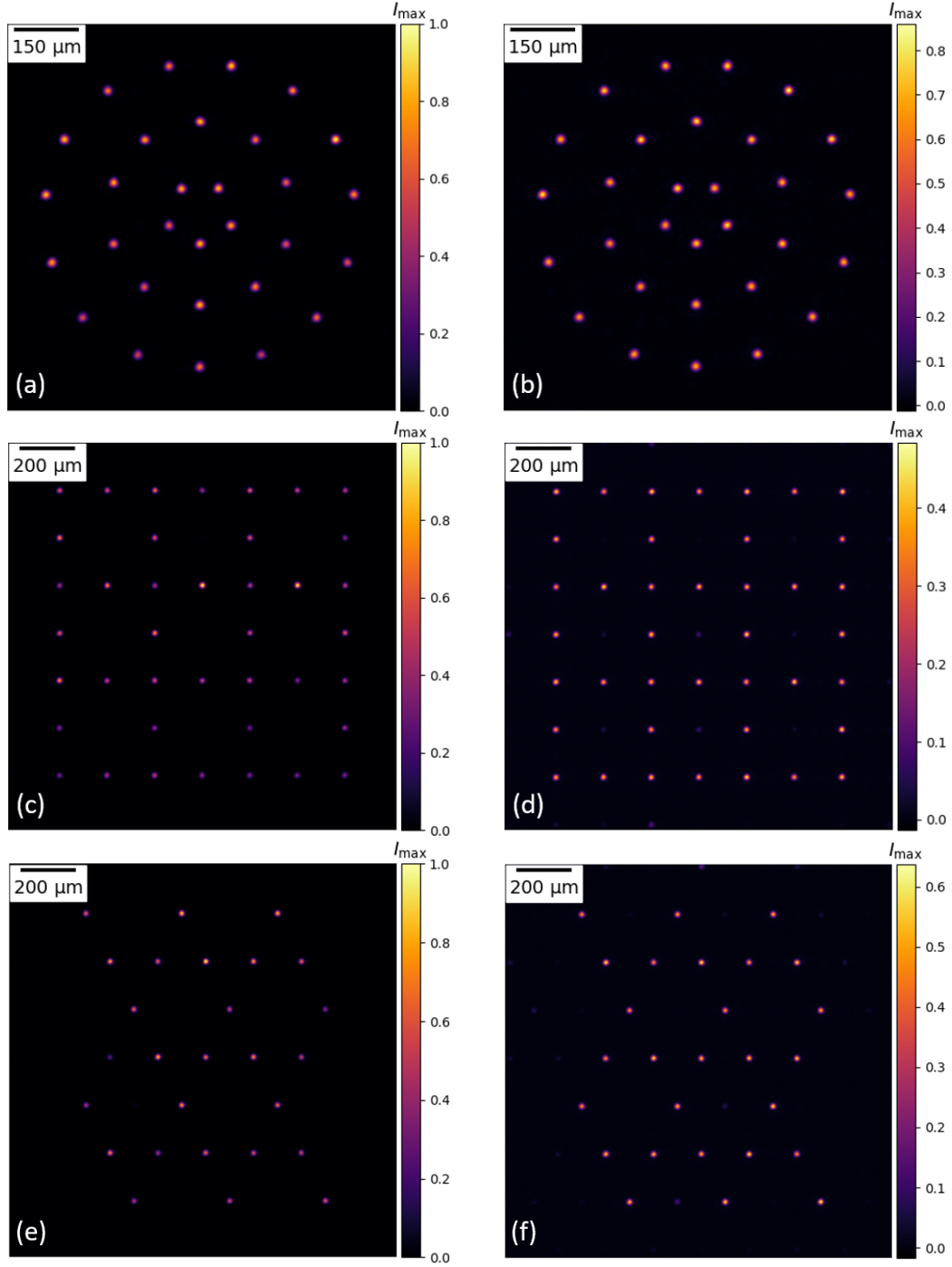


Figure 5.2: Circular (a, b), Lieb (c, d) and Kagome (e, f) lattice geometries using the GS (left column) and the WGS (right column) algorithm.

5.3 Scalability of WGS algorithm

We now focus on the scalability of the WGS algorithm with respect to the number of spots that can be reconstructed with reasonable quality. The largest number of spots we have been able to create successfully so far is 100 in the form of a 10×10 rectangular array. Note that this is not the upper limit of what is feasible with our system, but rather simply the largest array we have investigated so far.

Similar to before, we first apply the GS algorithm and extract the intensity uniformity and then determine its improvement thanks to the WGS algorithm. Figure 5.3 shows the reconstructed image on the camera via the GS algorithm, while Fig. 5.4 depicts the reconstructed image using the WGS algorithm. For 50 iterations of the GS algorithm, we find a uniformity of only around $u = 8.46\%$ and a mean spot size in the x - and y -direction of $\overline{W}_x = 15.3(5) \mu\text{m}$ and $\overline{W}_y = 15.1(4) \mu\text{m}$. Instead, the WGS algorithm yields an improved uniformity of $u = 97.64\%$ after 128 iterations. The mean spot size roughly remains the same with $\overline{W}_x = 15.2(5) \mu\text{m}$ and $\overline{W}_y = 15.2(4) \mu\text{m}$.

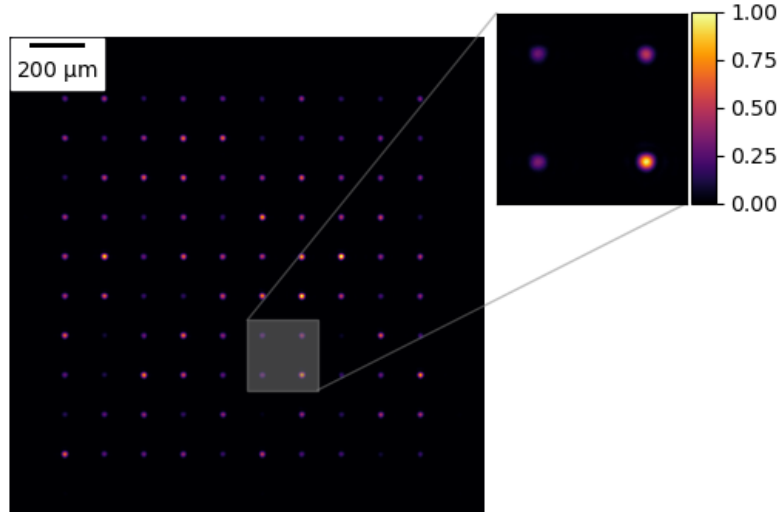


Figure 5.3: 10×10 rectangular optical tweezer array. The image is obtained after 50 iterations of the GS algorithm and suffers from substantial intensity non-uniformity, as clearly shown in the inset figure.

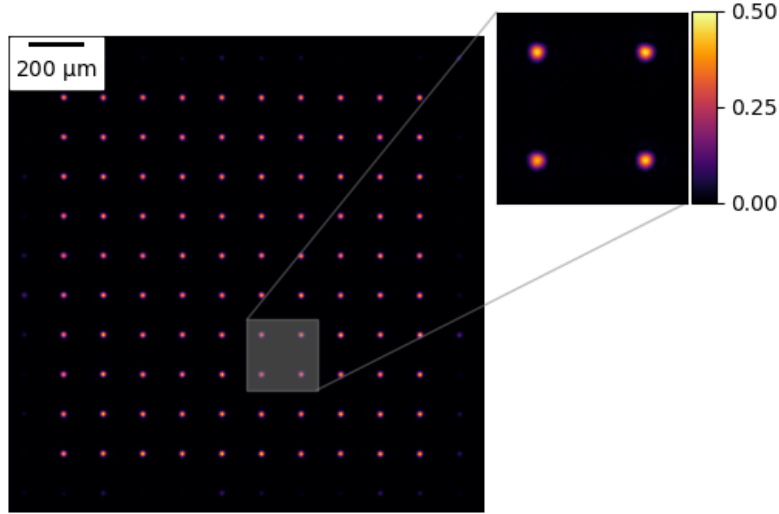


Figure 5.4: 10×10 rectangular optical tweezer array. The WGS algorithm terminates after 128 iterations and results in a great improvement of the intensity uniformity.

Note that the outperformance of the WGS algorithm over the GS algorithm becomes very evident when scaling up the lattice size. For instance, in the case of the 6×6 lattice, we obtain a uniformity of $u = 72.54\%$, while for a moderate scaling up to 10×10 , the uniformity obtained with the GS algorithm drops to $u = 8.46\%$ as mentioned before. However, for the WGS algorithm, reasonable uniformities of around 98% can be achieved for both lattice sizes. The corresponding graphs displaying the convergence of the uniformity, and of the RMSE and the maximum value of the weight can be found in Fig. A.2 in App. A.

5.4 Ghost spots

As mentioned, the intensity patterns we obtain can be polluted by undesired ghost spots. As an example, Fig. 5.5 shows ghosts spots for the specific case of the Lieb lattice. These ghost spots typically emerge as a side effect of the phase-only nature of LC SLMs. Due to the fact that the LC SLM is only able to modulate the phase, but not the intensity, it does not always accurately reconstruct the desired intensity distribution in the focus. As a

result, ghost spots may appear. As briefly discussed in Sec. 2.3, another set of ghost spots appears as a result of the pixelated structure of LC SLMs [87, 88].

In general, ghost spots resemble fainter replicas of the desired image and reflect specific symmetries thereof, as their location of formation is dependent on the symmetry of the target intensity pattern. Moreover, the ghost spots can interfere with the desired spots and consequently cause errors in the intensity distribution and reconstruction. This issue is particularly pronounced for highly symmetric spot configurations. Here, unwanted ghost spots usually exactly coincide with the position of the desired spots, leading to unequal spot intensities. As a result, the presence of ghost spots not only reduces the diffraction efficiency, but also severely degrades the uniformity of the final image. Besides giving rise to non-uniform intensity distributions, ghost spots can pose an additional issue when their intensity becomes comparable to the intensity of the desired spots. In that case, one can unintentionally trap particles in these unwanted spots during the experiment.

Depending on the trap geometry, the intensity of most of our ghost spots

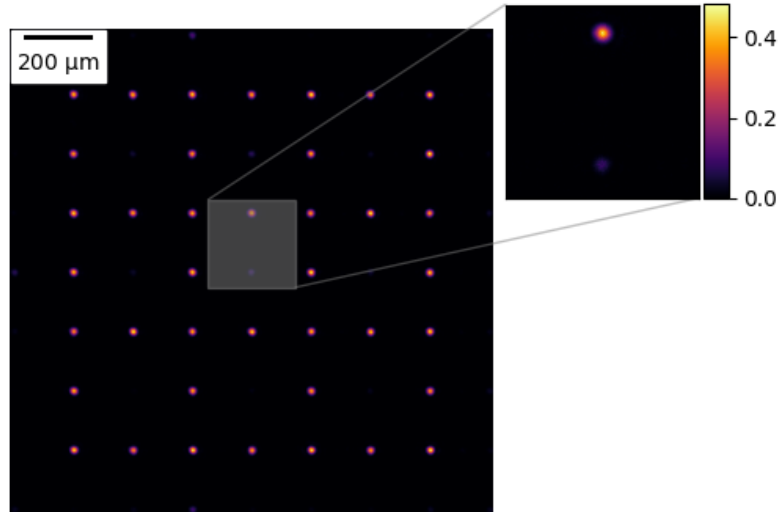


Figure 5.5: Lieb lattice of optical tweezers. The lower spot in the inset figure is one of many ghost spots, emerging due to the pixelated structure of the LC SLM and its phase-only nature.

is found to take values of around 10-15% of the intensity of the desired spots with outliers reaching even 35%. Different approaches aiming their suppression have been shown so far, one of which is presented in Ref. [88].

In Ref. [88], the authors employ a so-called virtual lens on the LC SLM only affecting the modulated light, where the virtual lens is essentially an additional phase pattern. The virtual lens configuration subsequently focuses the modulated light into the Fourier plane of the unmodulated light and vice versa. Accordingly, moving the first order diffraction beam with the desired pattern into the Fourier plane of the zero order beam comes with multiple benefits, one of which is that the zero order beam does not specifically have to be eliminated. Another benefit is the ability to remove undesired ghost spots by displacing them axially into other focal planes. As a result, using a virtual lens configuration yields fewer and lower intensity ghost spots.

5.5 Separation of spots

Besides the emergence of ghost spots, we identify an additional characteristic of the LC SLM that might cause issues in the reconstruction of images. If the separation of the spots as defined in the input target image is chosen too small, the spots are distorted significantly. As shown in Fig. 5.6, we reconstruct multiple images with different spot separations via the WGS algorithm to illustrate this problem.

As can be seen, the spot quality gets worse the smaller the separation is. We again fit each spot with a two-dimensional Gaussian function to determine its size and position. All the results are summarized in Table 5.3. Note that we are not able to conduct the fitting procedure for a separation of 2 pixels and 1 pixel. Additionally, the WGS algorithm can not be conducted properly for these two separations as the spot uniformities do not converge. As for the reason why this might be the case, we assume the following: When the distance between the spots decreases, we can observe a change of both their intensity and their shape. Since the exact intensity between the spots is quite random, the resulting interference is also rather random. As a result, an inhomogeneity of the power of the spots emerges and a distortion of their shape becomes visible. These effects are particularly prominent for smaller separations, which is why the WGS algorithm breaks down when try-

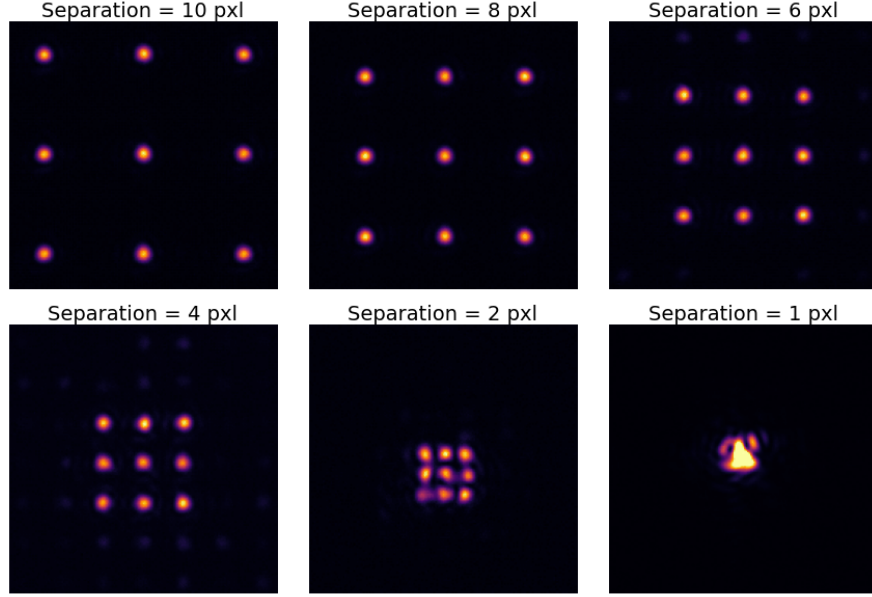


Figure 5.6: Rectangular lattice for different spot separations. We investigate the dependence of the spot quality for different separations of pixels (pxl) in the input target image. A significant decrease in quality can be observed for smaller separations.

ing to obtain uniform spot intensities. When running the WGS algorithm, we always make sure that the area surrounding each spot, which is used for evaluating its intensity, is chosen small enough such that it would not overlap with other areas or include neighbouring spots.

In Table 5.3, the separation in pixels is denoted Δx , while the calculated and measured separation in microns is denoted Δx_c and Δx_m , respectively. The calculation of the separation was conducted with the help of Eq. (3.13). The increase in uncertainty of the mean spot size in the x -direction for smaller separations might indicate a deformation of the spots. As depicted Fig. 5.7, we additionally find that the uniformity slightly decreases, while the corresponding RMSE increases with decreasing separation. Even though the results suggest a reduction in spot quality for decreasing separations, more measurements would have to be conducted for us to be able to support this statement, or might even define a threshold separation beyond which the

spots are deformed considerably. Nevertheless, Table 5.3 shows that the calculated spot separation coincides nicely with the measured one. Therefore, we are able to reliably reconstruct desired spot separations by choosing the target pattern accordingly.

Table 5.3: Calculated separation (Δx_c), mean measured separation ($\overline{\Delta x_m}$), mean spot size (\overline{W}_x , \overline{W}_y), uniformity (u) and RMSE for different trap separations of a 3×3 rectangular array using the WGS algorithm.

Δx (pxl)	10	8	6	4
Δx_c (μm)	142.96875	114.375	85.78125	57.1875
$\overline{\Delta x_m}$ (μm)	143.0(2)	114.4(2)	85.80(17)	57.2(2)
\overline{W}_x (μm)	15.2(2)	15.0(3)	15.3(4)	15.0(8)
\overline{W}_y (μm)	15.1(4)	15.2(4)	15.3(5)	15.2(4)
u (%)	99.06	98.92	98.82	98.80
RMSE (%)	1.73	2.11	2.27	2.33

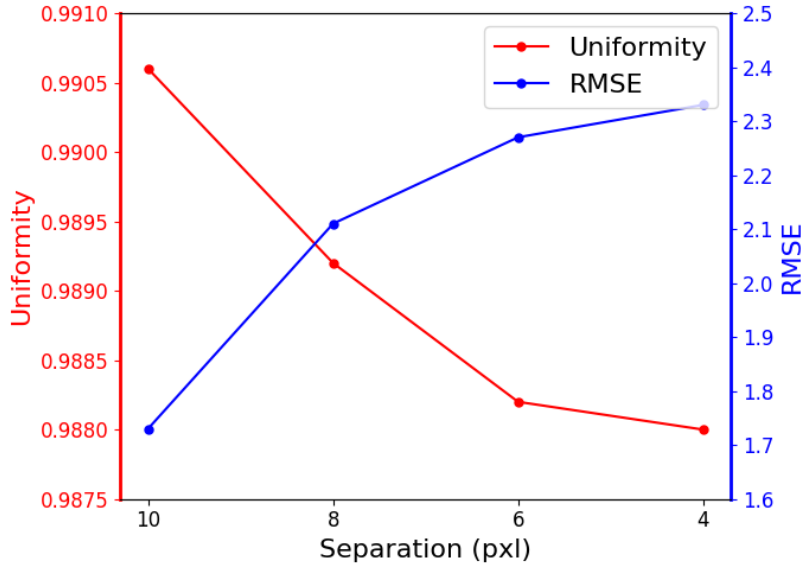


Figure 5.7: Trap uniformity and RMSE as a function of the spot separation.

Chapter 6

Conclusion and Outlook

The aim of this thesis was to generate two-dimensional optical tweezer arrays using an LC SLM for the main experiment in the T-REQS lab. In the main experiment, we generally want to work with dynamic optical tweezer arrays, which we want to harness for quantum simulation using erbium Rydberg atoms. Here, the idea is to use the LC SLM to create only a static pattern, which will then be overlapped with the output of two perpendicular AODs to move the atoms around and consequently make the arrays dynamic. A simplified idea of how overlapping the beam coming from the AODs and the one from the SLM setup could be realized is schematically depicted in Fig. 6.1, where we use polarizing beam splitter (PBS) for overlapping, while we use waveplates to control the intensity and the polarization.

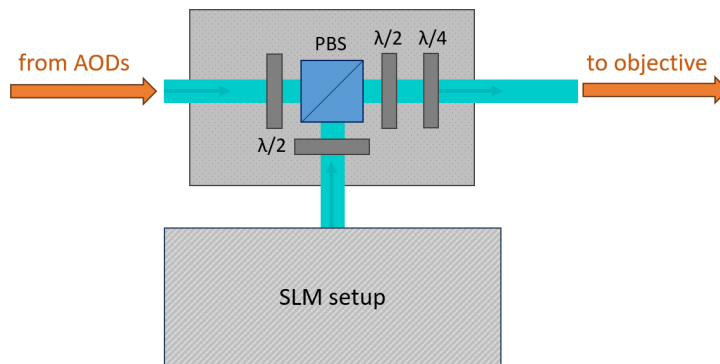


Figure 6.1: Schematic diagram of the overlap between the static pattern of the LC SLM and the moving optical tweezer of the AODs.

At the time of writing this thesis, we are able to generate a one-dimensional optical tweezer array using a single AOD. We are able to successfully trap erbium atoms in these optical tweezers, and at the moment, we are working towards achieving single atom trapping and optimizing our imaging sequence.

Within the scope of this thesis, we first put focus on reviewing Rydberg atoms, as we ultimately want to use these for quantum simulation. The general properties and interactions between Rydberg atoms were covered, where different quantum systems one can simulate were briefly mentioned. In particular, we put emphasis on discussing the Rydberg blockade as a special feature of Rydberg atoms. Here, we talked about the great importance of the Rydberg blockade in terms of quantum simulation. Eventually, we shed light on erbium in Rydberg physics and listed its most relevant properties. Erbium is especially interesting for these types of experiments as its multiple valence electrons give rise to a great variety of new excitation schemes, while its large angular momentum enables the encoding of large Hilbert spaces when doing quantum simulation.

Next, we introduced the basic concepts of atom-light interaction. Within this chapter, we put focus on describing the basic notions needed to understand optical tweezer experiment. Additionally, the majority of this part of the thesis was dedicated towards presenting an overview of different optical devices capable of generating optical tweezer arrays. We discussed the main devices, which include acousto-optic deflectors (AODs), digital micromirror devices (DMDs) and liquid crystal spatial light modulators (LC SLMs), where the working principle of the latter in particular was discussed extensively. Lastly, we compared the advantages and disadvantages of these devices, arguing why we have eventually decided to use an LC SLM.

After that, we presented the optical setup we used for testing the LC SLM. Subsequently, the generation of holographic two-dimensional optical tweezer arrays using an LC SLM was discussed, followed by an overview of the different phase patterns which are typically necessary to drive the LC SLM. In particular, we focused on the Gerchberg-Saxton (GS) algorithm and the weighted Gerchberg-Saxton (WGS) algorithm as means of retrieving phase patterns. At that point, we also presented our first reconstructed images and started comparing the corresponding reconstruction quality in dependence of the algorithm which was used.

The next chapter was entirely devoted to presenting the experimental results and continuing the discussion of the reconstruction quality as started in the previous chapter. Here, we analyzed the performance of the WGS algorithm and evaluated the quality of the resulting spots. We tested the functioning of both the GS algorithm and the WGS algorithm for a variety of different trap geometries. While the GS algorithm gave rise to considerable non-uniformities of the trap intensities for every geometry, the WGS algorithm on the other hand resulted significantly improved uniformities of trap intensities. However, we were able to identify two major problems in our reconstructed images, one of which was that the quality of the spots was found to decrease with a decreasing spot separation. Additionally, we observed the emergence of ghost spots in our reconstructed images. These ghost spots can pose serious issues regarding the implementation of the LC SLM setup in the main experiment, as it might occur that particles are trapped in these undesired spots.

In the future, it would therefore definitely be interesting to further investigate the negative influence of these ghost spots and address their suppression. As reported at the end of the previous chapter, we have not yet been able to explicitly determine a minimum separation beyond which the spots are distorted too much for us to be of any use. Thus, it would be intriguing to work out a reasonable threshold by conducting more/different measurements. Another parameter that is worth testing in the future is the scalability of the WGS algorithm in terms of the number of traps. At this point in time, we have been able to successfully reconstruct 100 traps, but have not yet tested the actual limit, which would be of great interest for the implementation in the main experiment. The way the aberration correction has been conducted until now is another factor that needs to be taken into consideration in the future. While we have put a camera directly in the focus of the traps and measured their intensity thus far, this will unfortunately not be feasible in the main experiment due to limitations in the optical setup. Instead, we are planning on using the light shifts of the optical tweezers for aberration correction.

Appendix A

This chapter includes additional information regarding the choice of wavelength and presents supplementary figures related to the data analysis as conducted in Chap. 5.

A.1 486 nm light

The reason for using a 486 nm laser for our optical tweezer arrays is that, due to the polarizability of erbium, we predict magic conditions for all our main cycling transitions at this wavelength. These cycling transitions are indicated by the arrows in Fig. 1.4 and the most relevant ones are briefly summarized in Table A.1.

In our case, "magic" refers to a specific ellipticity angle that nulls the differential light shift emerging due to the optical trap. Mathematically, this can be expressed as $U_\nu/U_g = 1$, where U_g is the light shift experienced by the ground state and U_ν the light shift of the respective excited state. Here, the excited state is different for every cycling transition, with ν denoting whether it is the 401 nm, 583 nm or 841 nm transition. The differential light shift takes the form

$$\Delta U(\mathbf{r}) = U_\nu - U_g = -\frac{\Delta\alpha(\nu, \chi)}{2\epsilon_0 c} I(\mathbf{r}), \quad (\text{A.1})$$

where $\Delta\alpha$ denotes the difference in polarizability of both states and I the intensity of the trapping potential. As can be seen, the differential light shift can be modified by tuning the trapping light polarisation ellipticity χ accordingly.

Table A.1: Most relevant cycling transitions in the main experiment.

	401 nm	583 nm	841 nm
$\Gamma/2\pi$	28 MHz	190 kHz	8 kHz
	Cooling, fast imaging	MOT, non-destructive imaging	Narrow-line cooling

Figure A.1 displays the ratio between the the light shifts of the ground state and excited state as a function of the ellipticity angle χ . For all three cycling transitions, we can determine an intersection with the horizontal line at a value of one. These three points of intersection correspond to the ellipticity angle at which the magic condition is reached.

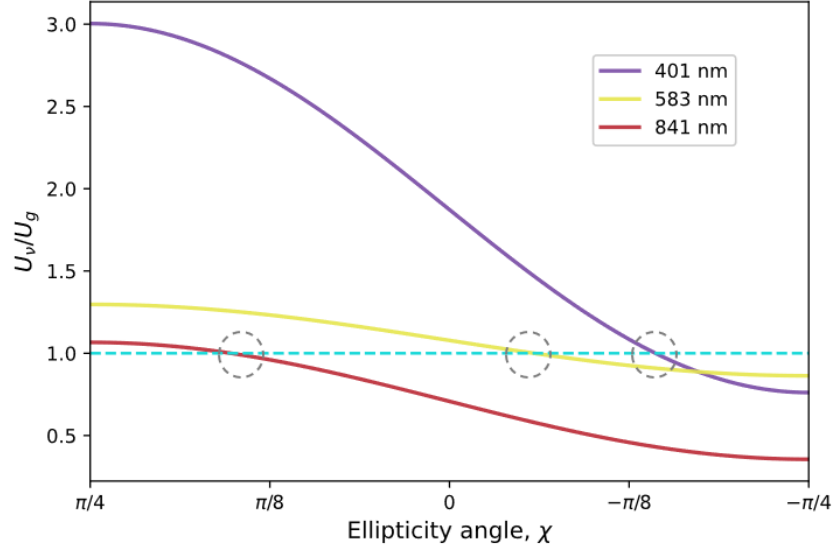


Figure A.1: Dependence of the differential light shift on the ellipticity angle of the trapping light. For all three relevant cycling transitions, we are able to determine magic conditions at different ellipticity angles, as indicated by the dashed circles.

A.2 Performance of WGS algorithm

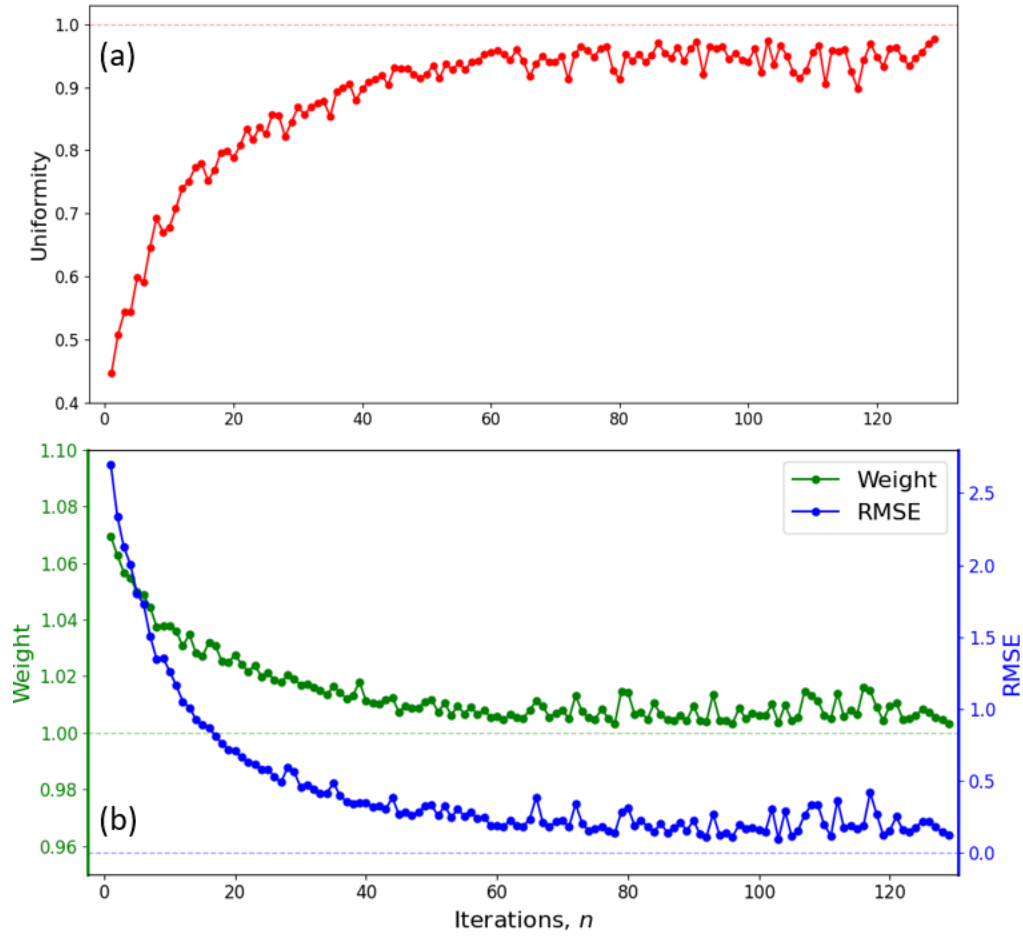


Figure A.2: Results of the WGS algorithm for the 10×10 rectangular array. (a) The uniformity after 128 iterations of the WGS algorithm amounts to about 97.64%. (b) With an increasing number of iterations, the associated RMSE and maximum value of the weight approach the values zero and one, respectively.

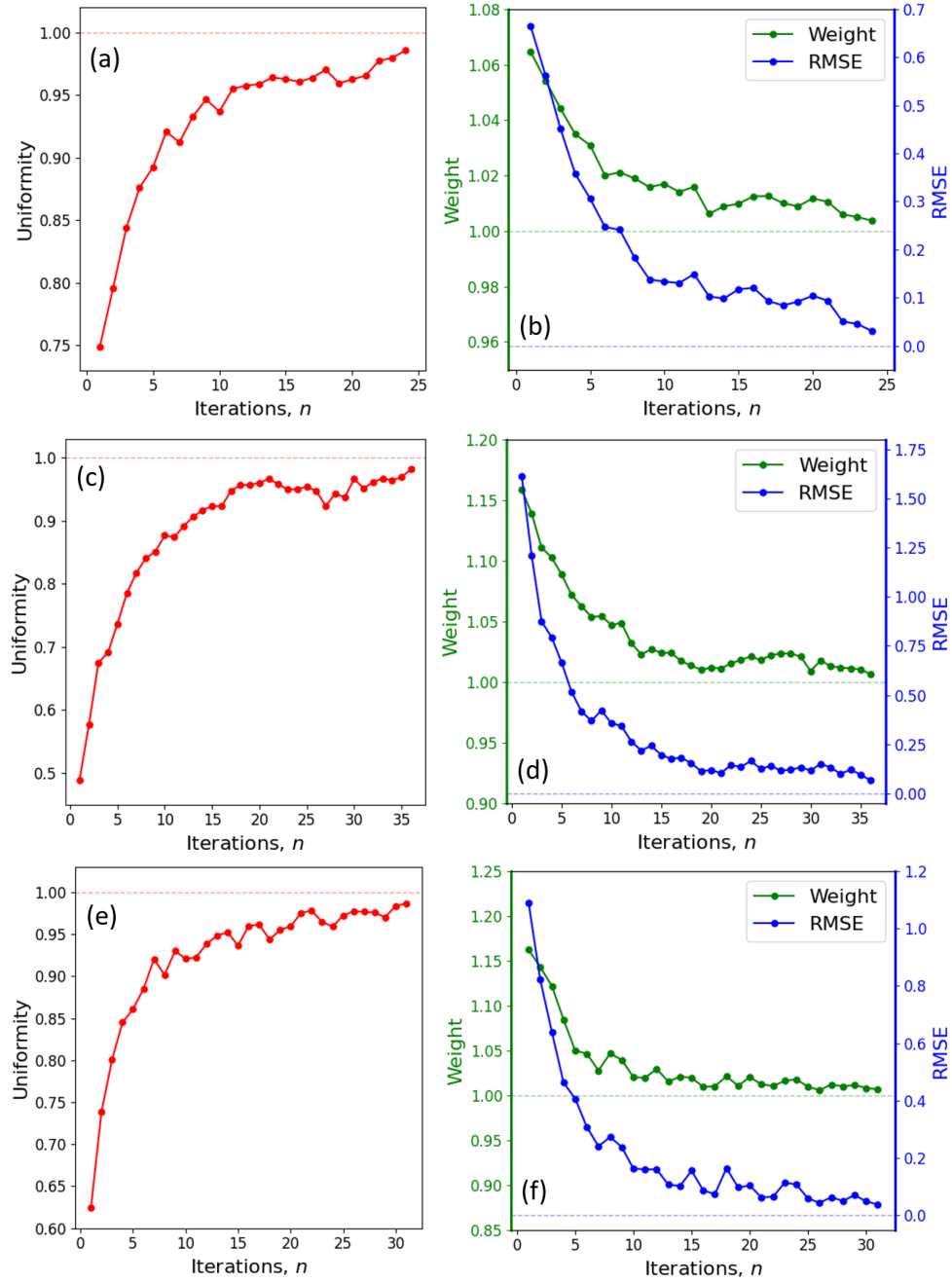


Figure A.3: Uniformity, RMSE, and weight as a function of the number of iterations for different trap geometries. Circular (a, b), Lieb (c, d) and Kagome (e, f).

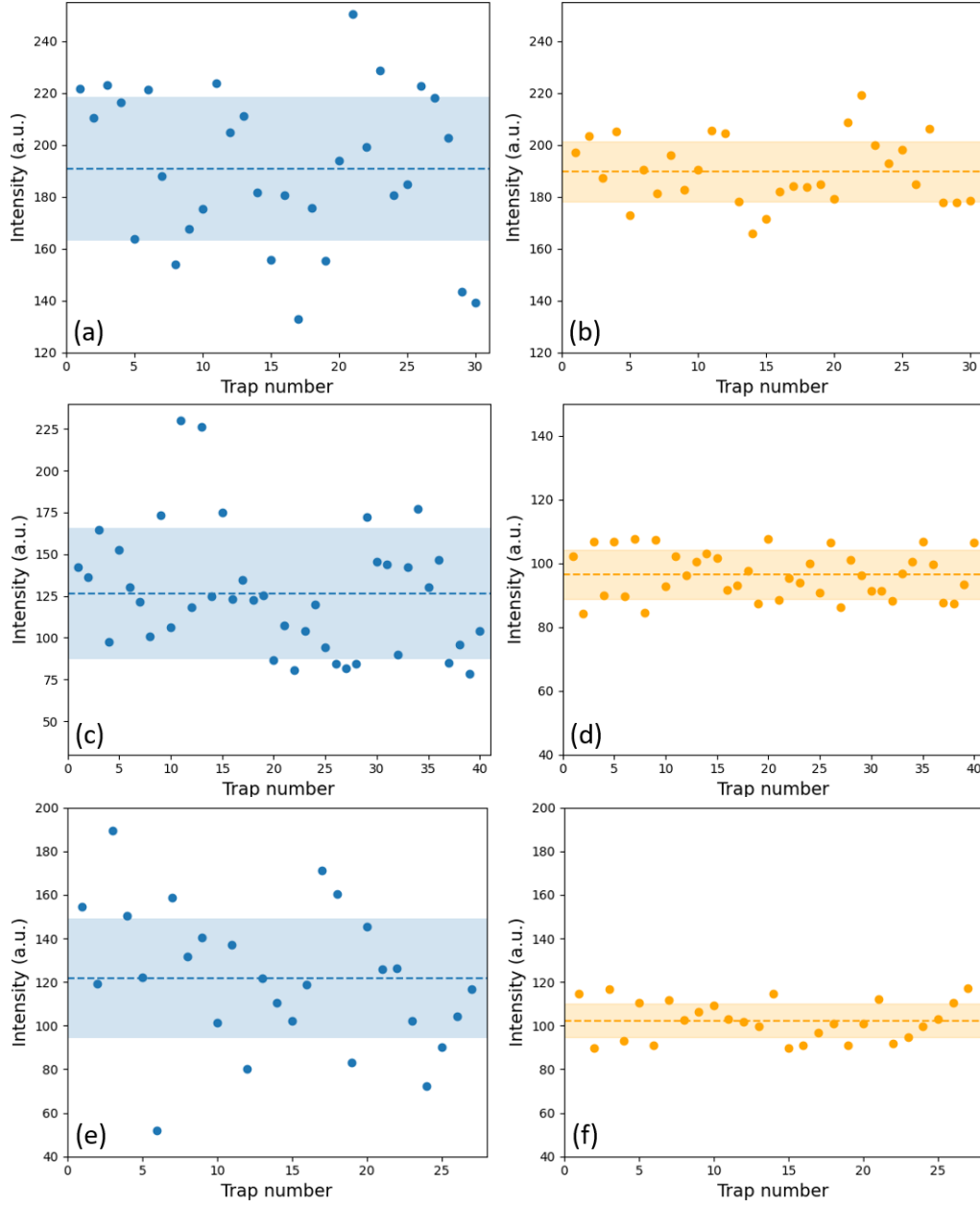


Figure A.4: Individual trap intensities for different trap geometries obtained via the GS (left column) algorithm and the WGS (right column) algorithm. Circular (a, b), Lieb (c, d) and Kagome (e, f).

Bibliography

- [1] Bose. Plancks Gesetz und Lichtquantenhypothese. *Zeitschrift für Physik*, 26:178–181, 1924.
- [2] A. Einstein. *Quantentheorie des einatomigen idealen Gases*. Nummer Buch 2 in Sitzungsberichte der Preussischen Akademie der Wissenschaften. Physikalisch-mathematische Klasse. Verlag d. Akad. d. Wiss., 1925. URL <https://books.google.at/books?id=oRFFHAAACAAJ>.
- [3] Sixty years of lasers. *Nature Reviews Physics*, 2:221, may 2020. doi: 10.1038/s42254-020-0181-9. URL <https://doi.org/10.1038/s42254-020-0181-9>.
- [4] K. B. Davis, M. O. Mewes, M. R. Andrews, N. J. van Druten, D. S. Durfee, D. M. Kurn, and W. Ketterle. Bose-einstein condensation in a gas of sodium atoms. *Phys. Rev. Lett.*, 75:3969–3973, Nov 1995. doi: 10.1103/PhysRevLett.75.3969. URL <https://link.aps.org/doi/10.1103/PhysRevLett.75.3969>.
- [5] M. H. Anderson, J. R. Ensher, M. R. Matthews, C. E. Wieman, and E. A. Cornell. Observation of bose-einstein condensation in a dilute atomic vapor. *Science*, 269(5221):198–201, 1995. doi: 10.1126/science.269.5221.198. URL <https://www.science.org/doi/abs/10.1126/science.269.5221.198>.
- [6] C. C. Bradley, C. A. Sackett, J. J. Tollett, and R. G. Hulet. Evidence of bose-einstein condensation in an atomic gas with attractive interactions. *Phys. Rev. Lett.*, 75:1687–1690, Aug 1995. doi: 10.1103/PhysRevLett.75.1687. URL <https://link.aps.org/doi/10.1103/PhysRevLett.75.1687>.

- [7] Eva Krutmeijer. The Nobel Prize in Physics 2001.
- [8] B. DeMarco and D. S. Jin. Onset of Fermi Degeneracy in a Trapped Atomic Gas. *Science*, 285(5434):1703–1706, 1999. doi: 10.1126/science.285.5434.1703. URL <https://www.science.org/doi/abs/10.1126/science.285.5434.1703>.
- [9] Immanuel Bloch, Jean Dalibard, and Sylvain Nascimbène. Quantum simulations with ultracold quantum gases. *Nature Physics*, 8(4):267–276, 2012. doi: 10.1038/nphys2259. URL <https://hal.science/hal-03740937>.
- [10] Christian Gross and Immanuel Bloch. Quantum simulations with ultracold atoms in optical lattices. *Science*, 357:995–1001, 09 2017. doi: 10.1126/science.aal3837.
- [11] Adam M. Kaufman and Kang-Kuen Ni. Quantum science with optical tweezer arrays of ultracold atoms and molecules. *Nature Physics*, 17(12):1324–1333, December 2021. doi: 10.1038/s41567-021-01357-2. URL <https://ui.adsabs.harvard.edu/abs/2021NatPh..17.1324K>.
- [12] Markus Greiner, Olaf Mandel, Tilman Esslinger, Theodor Haensch, and Immanuel Bloch. Quantum phase transition from a superfluid to a Mott insulator in a gas of ultracold atoms. *Nature*, 415:39–44, 02 2002. doi: 10.1038/415039a.
- [13] Antoine Browaeys and Thierry Lahaye. Many-body physics with individually controlled Rydberg atoms. *Nature Physics*, 16(2):132–142, jan 2020. doi: 10.1038/s41567-019-0733-z. URL <https://doi.org/10.1038%2Fs41567-019-0733-z>.
- [14] Hannes Bernien, Sylvain Schwartz, Alexander Keesling, Harry Levine, Ahmed Omran, Hannes Pichler, Soonwon Choi, Alexander S. Zibrov, Manuel Endres, Markus Greiner, Vladan Vuletić, and Mikhail D. Lukin. Probing many-body dynamics on a 51-atom quantum simulator. *Nature*, 551(7682):579–584, nov 2017. doi: 10.1038/nature24622. URL <https://doi.org/10.1038%2Fnature24622>.
- [15] Pascal Scholl, Michael Schuler, Hannah J. Williams, Alexander A. Eberharter, Daniel Barredo, Kai-Niklas Schymik, Vincent Lienhard, Louis-Paul Henry, Thomas C. Lang, Thierry Lahaye, Andreas M. Läuchli,

- and Antoine Browaeys. Quantum simulation of 2D antiferromagnets with hundreds of Rydberg atoms. *Nature*, 595(7866):233–238, jul 2021. doi: 10.1038/s41586-021-03585-1. URL <https://doi.org/10.1038/s41586-021-03585-1>.
- [16] Sepehr Ebadi, Tout T. Wang, Harry Levine, Alexander Keesling, Giulia Semeghini, Ahmed Omran, Dolev Bluvstein, Rhine Samajdar, Hannes Pichler, Wen Wei Ho, Soonwon Choi, Subir Sachdev, Markus Greiner, Vladan Vuletić, and Mikhail D. Lukin. Quantum phases of matter on a 256-atom programmable quantum simulator. *Nature*, 595(7866):227–232, jul 2021. doi: 10.1038/s41586-021-03582-4. URL <https://doi.org/10.1038/s41586-021-03582-4>.
- [17] C S Adams, J D Pritchard, and J P Shaffer. Rydberg atom quantum technologies. *Journal of Physics B: Atomic, Molecular and Optical Physics*, 53(1):012002, dec 2019. doi: 10.1088/1361-6455/ab52ef. URL <https://doi.org/10.1088/1361-6455/ab52ef>.
- [18] A. Ashkin. Acceleration and Trapping of Particles by Radiation Pressure. *Phys. Rev. Lett.*, 24:156–159, Jan 1970. doi: 10.1103/PhysRevLett.24.156. URL <https://link.aps.org/doi/10.1103/PhysRevLett.24.156>.
- [19] A. Ashkin, J. M. Dziedzic, J. E. Bjorkholm, and Steven Chu. Observation of a single-beam gradient force optical trap for dielectric particles. *Opt. Lett.*, 11(5):288–290, May 1986. doi: 10.1364/OL.11.000288. URL <https://opg.optica.org/ol/abstract.cfm?URI=ol-11-5-288>.
- [20] A. Trautmann, M. J. Mark, P. Ilzhöfer, H. Edri, A. El Arrach, J. G. Maloberti, C. H. Greene, F. Robicheaux, and F. Ferlaino. Spectroscopy of Rydberg states in erbium using electromagnetically induced transparency. *Physical Review Research*, 3(3), aug 2021. doi: 10.1103/physrevresearch.3.033165. URL <https://doi.org/10.1103/physrevresearch.3.033165>.
- [21] Antoine Browaeys, Daniel Barredo, and Thierry Lahaye. Experimental investigations of dipole–dipole interactions between a few Rydberg atoms. *Journal of Physics B: Atomic, Molecular and Optical Physics*, 49(15):152001, jun 2016. doi: 10.1088/0953-4075/49/15/152001. URL <https://dx.doi.org/10.1088/0953-4075/49/15/152001>.

- [22] L. Béguin, A. Vernier, R. Chicireanu, T. Lahaye, and A. Browaeys. Direct Measurement of the van der Waals Interaction between Two Rydberg Atoms. *Physical Review Letters*, 110(26), jun 2013. doi: 10.1103/physrevlett.110.263201. URL <https://doi.org/10.1103/physrevlett.110.263201>.
- [23] Thad G Walker and Mark Saffman. Zeros of Rydberg–Rydberg Förster interactions. *Journal of Physics B: Atomic, Molecular and Optical Physics*, 38(2):S309–S319, jan 2005. doi: 10.1088/0953-4075/38/2/022. URL <https://doi.org/10.1088/0953-4075/38/2/022>.
- [24] I. I. Beterov and M. Saffman. Rydberg blockade, Förster resonances, and quantum state measurements with different atomic species. *Phys. Rev. A*, 92:042710, Oct 2015. doi: 10.1103/PhysRevA.92.042710. URL <https://link.aps.org/doi/10.1103/PhysRevA.92.042710>.
- [25] Bo Yan, Steven A. Moses, Bryce Gadway, Jacob P. Covey, Kaden R.A. Hazzard, Ana Maria Rey, Deborah S. Jin, and Jun Ye. Observation of dipolar spin-exchange interactions with lattice-confined polar molecules. *Nature*, 501(7468):521–525, 2013. ISSN 0028-0836. doi: 10.1038/nature12483. URL <http://www.nature.com/doi/10.1038/nature12483>.
- [26] A. de Paz, A. Sharma, A. Chotia, E. Maréchal, J. H. Huckans, P. Pedri, L. Santos, O. Gorceix, L. Vernac, and B. Laburthe-Tolra. Nonequilibrium Quantum Magnetism in a Dipolar Lattice Gas. *Physical Review Letters*, 111(18), oct 2013. doi: 10.1103/physrevlett.111.185305. URL <https://doi.org/10.1103/physrevlett.111.185305>.
- [27] D. Jaksch, J. I. Cirac, P. Zoller, S. L. Rolston, R. Côté, and M. D. Lukin. Fast Quantum Gates for Neutral Atoms. *Phys. Rev. Lett.*, 85: 2208–2211, Sep 2000. doi: 10.1103/PhysRevLett.85.2208. URL <https://link.aps.org/doi/10.1103/PhysRevLett.85.2208>.
- [28] Xiaoling Wu, Xinhui Liang, Yaoqi Tian, Fan Yang, Cheng Chen, Yong-Chun Liu, Meng Khoon Tey, and Li You. A concise review of Rydberg atom based quantum computation and quantum simulation. *Chinese Physics B*, 30(2):020305, feb 2021. doi: 10.1088/1674-1056/abd76f. URL <https://doi.org/10.1088/1674-1056/abd76f>.

-
- [29] Daniel Barredo, Sylvain de Léséleuc, Vincent Lienhard, Thierry Lahaye, and Antoine Browaeys. An atom-by-atom assembler of defect-free arbitrary two-dimensional atomic arrays. *Science*, 354(6315):1021–1023, nov 2016. doi: 10.1126/science.aah3778. URL <https://doi.org/10.1126%2Fscience.aah3778>.
- [30] Daniel Barredo, Vincent Lienhard, Sylvain de Léséleuc, Thierry Lahaye, and Antoine Browaeys. Synthetic three-dimensional atomic structures assembled atom by atom. *Nature*, 561(7721):79–82, sep 2018. doi: 10.1038/s41586-018-0450-2. URL <https://doi.org/10.1038%2Fs41586-018-0450-2>.
- [31] J. Millen, G. Lochead, and M. P. A. Jones. Two-Electron Excitation of an Interacting Cold Rydberg Gas. *Phys. Rev. Lett.*, 105:213004, Nov 2010. doi: 10.1103/PhysRevLett.105.213004. URL <https://link.aps.org/doi/10.1103/PhysRevLett.105.213004>.
- [32] Luc Couturier, Ingo Nosske, Fachao Hu, Canzhu Tan, Chang Qiao, Y. H. Jiang, Peng Chen, and Matthias Weidemüller. Measurement of the strontium triplet Rydberg series by depletion spectroscopy of ultracold atoms. *Physical Review A*, 99(2), feb 2019. doi: 10.1103/physreva.99.022503. URL <https://doi.org/10.1103%2Fphysreva.99.022503>.
- [33] F. Camargo, R. Schmidt, J. D. Whalen, R. Ding, G. Woehl, S. Yoshida, J. Burgdörfer, F.B. Dunning, H.R. Sadeghpour, E. Demler, and T.C. Killian. Creation of Rydberg Polarons in a Bose Gas. *Physical Review Letters*, 120(8), feb 2018. doi: 10.1103/physrevlett.120.083401. URL <https://doi.org/10.1103%2Fphysrevlett.120.083401>.
- [34] H. Lehec, A. Zuliani, W. Maineult, E. Luc-Koenig, P. Pillet, P. Cheinet, F. Niyaz, and T. F. Gallagher. Laser and microwave spectroscopy of even-parity Rydberg states of neutral ytterbium and multichannel-quantum-defect-theory analysis. *Physical Review A*, 98(6), dec 2018. doi: 10.1103/physreva.98.062506. URL <https://doi.org/10.1103%2Fphysreva.98.062506>.
- [35] J. J. Tsai J. S. Coursey, D. J. Schwab and R. A. Dragoset. Atomic Weights and Isotopic Compositions with Relative Atomic Masses (version 4.1), 2015. URL <http://physics.nist.gov/Comp>.

-
- [36] Belloui Bouzid. Erbium Doped Fiber Laser and Amplifier. *Optics and Photonics Journal*, 04:189–193, 01 2014. doi: 10.4236/opj.2014.47019.
- [37] Michael Berglund and Michael E. Wieser. Isotopic compositions of the elements 2009 (IUPAC Technical Report). *Pure and Applied Chemistry*, 83(2):397–410, 2011. doi: doi:10.1351/PAC-REP-10-06-02. URL <https://doi.org/10.1351/PAC-REP-10-06-02>.
- [38] Albert Frisch. *Dipolar Quantum Gases of Erbium*. PhD thesis, University of Innsbruck, 10 2014.
- [39] B.G. Wybourne and L. Smentek. *Optical Spectroscopy of Lanthanides: Magnetic and Hyperfine Interactions (1st ed.)*. CRC Press, 2007.
- [40] Matthew A. Norcia and Francesca Ferlaino. Developments in atomic control using ultracold magnetic lanthanides. *Nature Physics*, 17(12): 1349–1357, nov 2021. doi: 10.1038/s41567-021-01398-7. URL <https://doi.org/10.1038/s41567-021-01398-7>.
- [41] J. T. Wilson, S. Saskin, Y. Meng, S. Ma, R. Dilip, A. P. Burgers, and J. D. Thompson. Trapping Alkaline Earth Rydberg Atoms Optical Tweezer Arrays. *Physical Review Letters*, 128(3), jan 2022. doi: 10.1103/physrevlett.128.033201. URL <https://doi.org/10.1103/PhysRevLett.128.033201>.
- [42] Arno Trautmann. LATEX-Code for level scheme was kindly provided.
- [43] Han Ban, M Jacka, James Hanssen, Joseph Reader, and Jabez McClelland. Laser cooling transitions in atomic erbium. *Optics express*, 13: 3185–95, 05 2005. doi: 10.1364/OPEX.13.003185.
- [44] A. Kramida, Yu. Ralchenko, J. Reader, and NIST ASD Team. *NIST Atomic Spectra Database (version. 5.10)*, [Online]. Gaithersburg, MD, 2016. URL <https://dx.doi.org/10.18434/T4W30F>. Accessed: 10/08/2023.
- [45] Rudolf Grimm, Matthias Weidemüller, and Yurii B. Ovchinnikov. Optical Dipole Traps for Neutral Atoms. volume 42 of *Advances In Atomic, Molecular, and Optical Physics*, pages 95–170. Academic Press, 2000. doi: [https://doi.org/10.1016/S1049-250X\(08\)60186-X](https://doi.org/10.1016/S1049-250X(08)60186-X). URL

- <https://www.sciencedirect.com/science/article/pii/S1049250X0860186X>.
- [46] H.J. Metcalf and Peter van der Straten. Laser Cooling and Trapping. *Journal of the Optical Society of America B*, 20, 05 2003. doi: 10.1364/JOSAB.20.000887.
- [47] R V Brooks, S Spence, A Guttridge, A Alampounti, A Rakonjac, L A McArd, Jeremy M Hutson, and Simon L Cornish. Preparation of one ^{87}Rb and one ^{133}Cd atom in a single optical tweezer. *New Journal of Physics*, 23(6):065002, jun 2021. doi: 10.1088/1367-2630/ac0000. URL <https://doi.org/10.1088%2F1367-2630%2Fac0000>.
- [48] David Dayton, John Gonglewski, Sergio Restaino, Jeffrey Martin, James Phillips, Mary Hartman, Stephen Browne, Paul Kervin, Joshua Snodgrass, Nevin Heimann, Michael Shilko, Richard Pohle, Bill Carrion, Clint Smith, and Daniel Thiel. Demonstration of new technology MEMS and liquid crystal adaptive optics on bright astronomical objects and satellites. *Opt. Express*, 10(25):1508–1519, Dec 2002. doi: 10.1364/OE.10.001508. URL <https://opg.optica.org/oe/abstract.cfm?URI=oe-10-25-1508>.
- [49] Ashton Hemphill and Lihong Wang. Hybridized wavefront shaping for high-speed, high-efficiency focusing through dynamic diffusive media. *Journal of Biomedical Optics*, 21:121502, 09 2016. doi: 10.1117/1.JBO.21.12.121502.
- [50] Zihui Zhang, Lloyd Russell, Adam Packer, Oliver Gauld, and Michael Hausser. Closed-loop all-optical interrogation of neural circuits in vivo. *Nature Methods*, 15, 12 2018. doi: 10.1038/s41592-018-0183-z.
- [51] Rongwen Lu, Wenzhi Sun, Yajie Liang, Aaron Kerlin, Jens Bierfeld, Johannes D. Seelig, Daniel E. Wilson, Benjamin Scholl, Boaz Mohar, Masashi Tanimoto, Minoru Koyama, David Fitzpatrick, Michael B. Orger, and Na Ji. Video-rate volumetric functional imaging of the brain at synaptic resolution. *Nature Neuroscience*, 20(4):620–628, mar 2017. ISSN 1097-6256. doi: 10.1038/nn.4516.
- [52] A. M. Weiner. Femtosecond pulse shaping using spatial light modulators. *Review of Scientific Instruments*, 71(5):1929–1960, 05 2000. ISSN 0034-

6748. doi: 10.1063/1.1150614. URL <https://doi.org/10.1063/1.1150614>.
- [53] Takeshi Fukuhara, Adrian Kantian, Manuel Endres, Marc Cheneau, Peter Schauß, Sebastian Hild, David Bellem, Ulrich Schollwöck, Thierry Giamarchi, Christian Gross, Immanuel Bloch, and Stefan Kuhr. Quantum dynamics of a mobile spin impurity. *Nature Physics*, 9(4):235–241, feb 2013. doi: 10.1038/nphys2561. URL <https://doi.org/10.1038/2Fnpphys2561>.
- [54] Philipp M. Preiss, Ruichao Ma, M. Eric Tai, Alexander Lukin, Matthew Rispoli, Philip Zupancic, Yoav Lahini, Rajibul Islam, and Markus Greiner. Strongly correlated quantum walks in optical lattices. *Science*, 347(6227):1229–1233, mar 2015. doi: 10.1126/science.1260364. URL <https://doi.org/10.1126/science.1260364>.
- [55] Guillaume Gauthier, Thomas A. Bell, Alexander B. Stilgoe, Mark Baker, Halina Rubinsztein-Dunlop, and Tyler W. Neely. Dynamic high-resolution optical trapping of ultracold atoms. In *Advances In Atomic, Molecular, and Optical Physics*, pages 1–101. Elsevier, 2021. doi: 10.1016/bs.aamop.2021.04.001. URL <https://doi.org/10.1016/bs.aamop.2021.04.001>.
- [56] Alexandre Cooper, Jacob P. Covey, Ivaylo S. Madjarov, Sergey G. Porsev, Marianna S. Safronova, and Manuel Endres. Alkaline-Earth Atoms in Optical Tweezers. *Phys. Rev. X*, 8:041055, Dec 2018. doi: 10.1103/PhysRevX.8.041055. URL <https://link.aps.org/doi/10.1103/PhysRevX.8.041055>.
- [57] Manuel Endres, Hannes Bernien, Alexander Keesling, Harry Levine, Eric R. Anschuetz, Alexandre Krajenbrink, Crystal Senko, Vladan Vuletic, Markus Greiner, and Mikhail D. Lukin. Atom-by-atom assembly of defect-free one-dimensional cold atom arrays. *Science*, 354(6315):1024–1027, 2016. doi: 10.1126/science.aah3752. URL <https://www.science.org/doi/abs/10.1126/science.aah3752>.
- [58] M. A. Norcia, A. W. Young, and A. M. Kaufman. Microscopic Control and Detection of Ultracold Strontium in Optical-Tweezer Arrays. *Phys. Rev. X*, 8:041054, Dec 2018. doi: 10.1103/PhysRevX.8.041054. URL <https://link.aps.org/doi/10.1103/PhysRevX.8.041054>.

-
- [59] Texas-Instruments. DMD101: Introduction to Digital Micromirror Device (DMD) Technology, (2008, rev. 2018).
- [60] Daniel Petter. Spatial modulation of light for ultracold gas experiments with erbium atoms, 2015.
- [61] Michel Mitov. Liquid-crystal science from 1888 to 1922: Building a revolution. *ChemPhysChem*, 15(7):1245–1250, January 2014. doi: 10.1002/cphc.201301064. URL <https://hal.science/hal-01764620>.
- [62] P. J. Collings. *Liquid Crystals: Nature's Delicate Phase Of Matter*. Princeton University Press, 2002.
- [63] HAMAMATSU. Phase spatial light modulator LCOS-SLM, 2021.
- [64] Walter Harm, Alexander Jesacher, Gregor Thalhammer, Stefan Bernet, and Monika Ritsch-Marte. How to use a phase-only spatial light modulator as a color display. *Opt. Lett.*, 40(4):581–584, Feb 2015. doi: 10.1364/OL.40.000581. URL <https://opg.optica.org/ol/abstract.cfm?URI=ol-40-4-581>.
- [65] Silvio Bianchi and Roberto Di Leonardo. A multi-mode fiber probe for holographic micromanipulation and microscopy. *Lab Chip*, 12:635–639, 2012. doi: 10.1039/C1LC20719A. URL <http://dx.doi.org/10.1039/C1LC20719A>.
- [66] Cecilia Muldoon, Lukas Brandt, Jian Dong, Dustin Stuart, Edouard Brainis, Matthew Himsworth, and Axel Kuhn. Control and manipulation of cold atoms in optical tweezers. *New Journal of Physics*, 14(7):073051, jul 2012. doi: 10.1088/1367-2630/14/7/073051. URL <https://doi.org/10.1088%2F1367-2630%2F14%2F7%2F073051>.
- [67] Haining Yang and D P Chu. Phase flicker in liquid crystal on silicon devices. *Journal of Physics: Photonics*, 2(3):032001, may 2020. doi: 10.1088/2515-7647/ab8a57. URL <https://dx.doi.org/10.1088/2515-7647/ab8a57>.
- [68] Michał Makowski. Experimental Aspects of Holographic Projection with a Liquid-Crystal-on-Silicon Spatial Light Modulator. In Manoj Kumar, editor, *Holographic Materials and Applications*, chapter 5. IntechOpen,

- Rijeka, 2019. doi: 10.5772/intechopen.85118. URL <https://doi.org/10.5772/intechopen.85118>.
- [69] Dapu Pi, Juan Liu, Xin Li, and Yongtian Wang. Review of computer-generated hologram algorithms for color dynamic holographic three-dimensional display. *Light: Science & Applications*, 11:231, 07 2022. doi: 10.1038/s41377-022-00916-3. URL <https://doi.org/10.1038/s41377-022-00916-3>.
- [70] Mostafa Agour, Ervin Kolenovic, Claas Falldorf, and Christoph von Kopylow. Suppression of higher diffraction orders and intensity improvement of optically reconstructed holograms from a spatial light modulator. *Journal of Optics A: Pure and Applied Optics*, 11(10): 105405, aug 2009. doi: 10.1088/1464-4258/11/10/105405. URL <https://dx.doi.org/10.1088/1464-4258/11/10/105405>.
- [71] Sergey Turtaev, Ivo T. Leite, Kevin J. Mitchell, Miles J. Padgett, David B. Phillips, and Tomáš Čižmár. Comparison of nematic liquid-crystal and DMD based spatial light modulation in complex photonics. *Opt. Express*, 25(24):29874–29884, Nov 2017. doi: 10.1364/OE.25.029874. URL <https://opg.optica.org/oe/abstract.cfm?URI=oe-25-24-29874>.
- [72] HAMAMATSU. LCOS-SLM Applications and Features, 2023. URL https://www.hamamatsu.com/content/dam/hamamatsu-photonics/sites/documents/99_SALES_LIBRARY/lpd/application_note_LCOS_E.pdf.
- [73] Allison E.M. Browar, Maxim Shusteff, Brett E. Kelly, Robert M. Panas, Jonathan D. Ellis, and Christopher M. Spadaccini. Overview and comparison of spatial light modulator calibration methods. In *Proceedings - ASPE 2016 Annual Meeting*, Proceedings - ASPE 2016 Annual Meeting, pages 293–299. American Society for Precision Engineering, ASPE, 2016. 31st Annual Meeting of the American Society for Precision Engineering, ASPE 2016 ; Conference date: 23-10-2016 Through 28-10-2016.
- [74] Hao Zhang, Jinghui Xie, Juan Liu, and Yongtian Wang. Elimination of a zero-order beam induced by a pixelated spatial light modulator for holographic projection. *Applied optics*, 48:5834–41, 10 2009. doi: 10.1364/AO.48.005834.

-
- [75] Darwin Palima and Vincent Daria. Holographic projection of arbitrary light patterns with a suppressed zero-order beam. *Applied optics*, 46: 4197–201, 08 2007. doi: 10.1364/AO.46.004197.
- [76] Jinyang Liang, Sih-Ying Wu, Fredrik Fatemi, and Michael Becker. Suppression of the zero-order diffracted beam from a pixelated spatial light modulator by phase compression. *Applied optics*, 51:3294–304, 06 2012. doi: 10.1364/AO.51.003294.
- [77] Vasudevan Lakshminarayanan and Andre Fleck. Zernike polynomials: A guide. *Journal of Modern Optics - J MOD OPTIC*, 58:1678–1678, 04 2011. doi: 10.1080/09500340.2011.633763.
- [78] Lizhi Chen, Hao Zhang, Zehao He, Xiaoyu Wang, Liangcai Cao, and Guofan Jin. Weighted constraint iterative algorithm for phase hologram generation. *Applied Sciences*, 10(10), 2020. ISSN 2076-3417. doi: 10.3390/app10103652. URL <https://www.mdpi.com/2076-3417/10/10/3652>.
- [79] Lizhi Chen, Hao Zhang, Liangcai Cao, and Guofan Jin. Non-iterative phase hologram generation with optimized phase modulation. *Opt. Express*, 28(8):11380–11392, Apr 2020. doi: 10.1364/OE.391518. URL <https://opg.optica.org/oe/abstract.cfm?URI=oe-28-8-11380>.
- [80] Yang Wu, Jun Wang, Chun Chen, Chan-Juan Liu, Feng-Ming Jin, and Ni Chen. Adaptive weighted gerchberg-saxton algorithm for generation of phase-only hologram with artifacts suppression. *Opt. Express*, 29(2):1412–1427, Jan 2021. doi: 10.1364/OE.413723. URL <https://opg.optica.org/oe/abstract.cfm?URI=oe-29-2-1412>.
- [81] G. J. Dijk. Intensity patterns generated with a Spatial Light Modulator, 2012.
- [82] Zixin Zhao. High Precision Optical Wavefront Generation Using Liquid Crystal Spatial Light Modulator (LC-SLM), 2021. URL <https://doi.org/10.5772/intechopen.100379>.
- [83] Rujia Li and Liangcai Cao. Progress in Phase Calibration for Liquid Crystal Spatial Light Modulators. *Applied Sciences*, 9(10):2012, May 2019. ISSN 2076-3417. doi: 10.3390/app9102012. URL <http://dx.doi.org/10.3390/app9102012>.

-
- [84] José Luis Martínez Fuentes, Enrique J. Fernández, Pedro M. Prieto, and Pablo Artal. Interferometric method for phase calibration in liquid crystal spatial light modulators using a self-generated diffraction-grating. *Opt. Express*, 24(13):14159–14171, Jun 2016. doi: 10.1364/OE.24.014159. URL <https://opg.optica.org/oe/abstract.cfm?URI=oe-24-13-14159>.
- [85] Rhine Samajdar, Wen Wei Ho, Hannes Pichler, Mikhail D. Lukin, and Subir Sachdev. Quantum phases of Rydberg atoms on a kagome lattice. *Proceedings of the National Academy of Sciences*, 118(4), jan 2021. doi: 10.1073/pnas.2015785118. URL <https://doi.org/10.1073%2Fpnas.2015785118>.
- [86] A. Dauphin, M. Müller, and M. A. Martin-Delgado. Quantum simulation of a topological Mott insulator with Rydberg atoms in a Lieb lattice. *Physical Review A*, 93(4), apr 2016. doi: 10.1103/physreva.93.043611. URL <https://doi.org/10.1103%2Fphysreva.93.043611>.
- [87] Francesca Anselmi, Arkarup Banerjee, and Dinu Florin Albeanu. *Patterned Photostimulation in the Brain*, pages pp 235–270. 04 2015. ISBN 978-3-319-12913-6. doi: 10.1007/978-3-319-12913-6_9.
- [88] Samira Aghayee, Mitchell Weikert, Phillip Alvarez, Gabriel A. Frank, and Wolfgang Losert. High Fidelity Spatial Light Modulator Configuration for Photo-Stimulation. *Frontiers in Physics*, 9, 2021. ISSN 2296-424X. doi: 10.3389/fphy.2021.587112. URL <https://www.frontiersin.org/articles/10.3389/fphy.2021.587112>.

Acknowledgements

First, I would like to thank my supervisor Francesca Ferlino for giving me the opportunity to work in the T-REQS lab. I am grateful for the support and helpful advice when writing this thesis.

I would also like to thank Manfred, who was always available for valuable discussions and had an open ear for my questions, despite constantly being in a hurry.

A big thank you goes out to all the members of the T-REQS, who always supported me and tried to answer all my questions, as silly as they often were. In particular, I would like to thank Daniel and Sam for helping me to write the code. A special thanks also goes to Andrea and Antonio, who gave great advice and suggestions for corrections to my thesis.

Zu guter Letzt möchte ich von ganzem Herzen meinen Eltern danken. Sie sind mir immer unterstützend zur Seite gestanden, sei es finanziell oder durch wertvolle Ratschläge und ein paar aufmunternde Worte. Ohne Euch wäre das alles nicht möglich gewesen - danke!

Eidesstattliche Erklärung

Ich erkläre hiermit an Eides statt durch meine eigenhändige Unterschrift, dass ich die vorliegende Arbeit selbständig verfasst und keine anderen als die angegebenen Quellen und Hilfsmittel verwendet habe. Alle Stellen, die wörtlich oder inhaltlich den angegebenen Quellen entnommen wurden, sind als solche kenntlich gemacht.

Die vorliegende Arbeit wurde bisher in gleicher oder ähnlicher Form noch nicht als Magister-/Master-/Diplomarbeit/Dissertation eingereicht.

Datum

Unterschrift